THE EFFECT OF REACTION AND INFILTRATION ON THE DEGRADATION OF REFRACTORY CERAMICS BY MOLTEN METALS

by

Richard Wesley Jackson III

BS, University of Pittsburgh, 2004

MS, University of Pittsburgh, 2007

Submitted to the Graduate Faculty of

Swanson School of Engineering in partial fulfillment

of the requirements for the degree of

Doctor of Philosophy

University of Pittsburgh

2010

UNIVERSITY OF PITTSBURGH

SWANSON SCHOOL OF ENGINEERING

This dissertation was presented

by

Richard Wesley Jackson III

It was defended on

January 19, 2010

and approved by

J.A. Barnard, Professor, Mechanical Engineering & Materials Science

C.E. Eckert, President, Apogee Technology

J.P. Leonard, Assistant Professor, Mechanical Engineering & Materials Science

W.S. Slaughter, Professor, Mechanical Engineering & Materials Science

Dissertation Co-Director: G.H. Meier, Professor, Mechanical Engineering & Materials Science

Dissertation Co-Director: F.S. Pettit, Professor Emeritus, Mechanical Engineering & Materials Science

THE EFFECT OF REACTION AND INFILTRATION ON THE DEGRADATION OF REFRACTORY CERAMICS BY MOLTEN METALS

Richard Wesley Jackson III, PhD

University of Pittsburgh, 2010

The degradation of refractory ceramics, used to contain and thermally insulate molten aluminum, in many aluminum processing operations, decreases the efficiency of aluminum production. The decreased efficiency results from the erosion of the refractory ceramic by molten aluminum, which increases thermal losses, and, eventually leads to the stoppage of production when the refractory is replaced.

There are two primary modes of refractory degradation; chemical reaction and infiltration. Chemical reaction leads to a steady decrease in the amount of refractory material. To study this phenomenon, tests were performed in which ceramic substrates were immersed in molten metals and the subsequent microstructural evolution was analyzed. Using thermodynamic, kinetic, and mechanical considerations, the critical factors which govern the rate of reaction were identified. From these investigations, a model was developed to determine the equilibrium interfacial composition, and the rate of oxide dissolution. Also, the importance of the Pilling-Bedworth ratio, the ratio of reaction product to reactant molar volume, in the development of refractory ceramics which are resistant to chemical attack was demonstrated.

Molten metal infiltration into the cracks and pores in refractory ceramic materials is the second mode of degradation. The infiltration of cracks with metal can lead to further cracking upon thermal cycling, and, if widespread infiltration occurs, the rate of degradation can be rapid. Two experimental methodologies were used to investigate the tendency for molten metals to infiltrate cracks. First, the classic sessile drop method was used to investigate several model metal-oxide systems, to determine the factors which affect the wetting and infiltration behavior of molten metals. Using these results, several parameters which can affect infiltration behavior

were identified. Secondly, a new experimental method was developed, the dynamic capillary displacement method, to directly study the infiltration behavior of molten aluminum in refractory ceramics. The contact angles, calculated from the infiltration behavior of Al into Al_2O_3 capillaries, are in good agreement with the contact angles reported in the literature, determined by other methodologies.

Combining the investigation of the chemical reactions with the infiltration investigation, a framework was developed for the mechanisms by which molten metals degrade ceramics.

TABLE OF CONTENTS

LIST OF TABLES

LIST OF FIGURES

PREFACE

This work would not have been possible without the assistance of a number of individuals. First, and foremost, I thank my advisors; Prof. G.H. Meier and Prof. F.S. Pettit, for their guidance throughout my time at the University of Pittsburgh. I am grateful for the support that they have given me and the opportunities that they have afforded me. I have been privileged to work with them.

This work would not have been possible without funding from Apogee Technology, Inc. I want to thank Dr. C.E. Eckert, President, Apogee Technology, for his support, encouragement and insight, throughout this project. I also want thank many others at Apogee, particularly Bill Alexander, whose assistance in many of my experiments was essential, and, also, Mike Gray, Scott Moline, George Ducsay, Jack Ducsay, Dave Piccolino, Mike Kinoz and Tom Meyers.

I also want to thank the faculty of the Department of Mechanical Engineering and Materials Science, particularly, my committee members, Prof. Barnard, Prof. Leonard, and Prof. Slaughter. I also want to thank Al Stewart, Matt Stiger, Meltem Yanar, Keeyoung Jung, Andreas Kulovits, Ed Magee, Chris Pekor, Michael Task, Michael Helminiack, Nan Mu, Wei Zhang, and Prof. B.M Gleeson. Their assistance with experiments, and the many discussions I have had with them, has been invaluable.

Finally, I would like to thank my family for all the love and support that they have given me, particularly, my sister, Nancy, for introducing me to engineering, my mother, Joan, who taught me value of hard work, and my father, Skip, who taught me the joy of finding things out.

1.0 INTRODUCTION

The behavior of metal-ceramic interfaces plays an important role in the performance of many engineering technologies.[1] Notable examples are structural materials, such as metal-matrix composites and corrosion resistant alloys[2-4], functional materials such as heterostructured electronics, and refractory ceramics used in liquid metal processing.[5]

As different as these technologies are, so are their desired interfacial properties. In composite structural materials, good adhesion between the metal and ceramic component is generally the most important interfacial property. In the fabrication of metal matrix composites, good wettability by the liquid metal on the ceramic is essential for fabrication. Conversely, in the processing of liquid metals, it is desired that the reactivity and wettability of liquid metals on refractory ceramic structures be minimized.

However, despite the ubiquity of the metal-ceramic interface, structure-composition-properties relationships are well understood under only the most idealized circumstances.[1, 6] Improvement in the understanding of the metal-ceramic interface has been slow due to the extreme difference in the properties of metals and the properties of ceramics.

One technology in which the operating efficiency could be greatly improved through a better understanding of the behavior of metal-ceramic interfaces occurs in the aluminum processing industry. In many aluminum processing operations, it is necessary for large reservoirs of aluminum to be held in the molten state. Refractory ceramics line the walls of these reservoirs, physically containing the molten metal, and providing thermal insulation. Typically, the refractory ceramics are composed of an alumina-silica matrix, with second phase materials such as barite and fluorite.

During service, the refractory ceramics are eroded through interaction with the molten metal, and, eventually, operation must be halted while the refractory is replaced. The loss of refractory material results in a gradual decrease in efficiency due to increasing thermal losses commensurate with the progressively thinning insulating refractory. Improving the resistance of refractory ceramics to degradation by liquid aluminum will increase the insulating efficiency, and reduce the frequency of shutdowns.

Additionally, a number of advanced technologies, such as direct immersion heaters, (resistance heaters encapsulated in a refractory ceramic envelope, which separates the heating elements from the molten metal) are being developed. In this technology, where maximum heat transfer is desired, the thickness of the refractory material must be minimized. As a result, refractory erosion can lead to failure, and knowledge of the refractory degradation rate is even more important.

The goal of this investigation is to develop a fundamental understanding of the mechanisms by which refractory ceramics are degraded by liquid aluminum.

There are two primary modes of refractory degradation; direct chemical reaction and infiltration. In many molten metal-ceramic systems there is a thermodynamic driving force for chemical reaction to take place at the metal-ceramic interface to produce a new phase. To study this phenomenon, tests were performed in which ceramic substrates were immersed in liquid metals. The microstructural evolution was analyzed, and using thermodynamic, kinetic, and mechanical considerations, the critical factors which govern the rate of reaction were identified

The second mode of degradation is metal infiltration into the cracks and pores which are always present in refractory ceramic materials. When molten metal infiltrates a crack, the tendency for further cracking, upon thermal cycling, is increased. If widespread infiltration occurs, the rate of refractory degradation can be rapid due to spallation.

The tendency for a molten metal to infiltrate a crack is governed by surface thermodynamics. Therefore, to probe the tendency for infiltration, the wetting properties of aluminum-refractory systems were studied, along with the wetting behavior of several model metal-oxide couples.

Investigating the wetting properties of liquid aluminum is difficult experimentally, due to the tendency for aluminum to react with oxygen, which prevents an intrinsic measurement of the wetting properties from being made. To avoid this issue, a twofold approach was taken. First, the sessile drop test was performed using several model metal-oxide systems and a model was

developed to predict the amount of oxide dissolution which occurs at a metal-oxide interface. Using the sessile drop results and the dissolution model, along with results and theories in the literature, general trends which influence wetting have been established.

Secondly, to study the wetting properties of liquid aluminum, a new experimental method was developed, the dynamic capillary displacement test, (DCD), to directly study the infiltration behavior of liquid aluminum into refractory ceramics. This test is based on the classic capillary rise experiment, and determines the wetting properties of a liquid-solid system based on the solid-liquid interactions, and is not directly influenced by the liquid-vapor interactions, as is the case with the sessile drop test.

Combining the investigation of the chemical reactions between molten metals and ceramics with the infiltration investigation gives a framework for understanding the factors by which molten metals degrade ceramics.

2.0 BACKGROUND

2.1 THERMODYNAMICS OF CHEMICAL REACTIONS

When evaluating how a material will behave in an environment, it is important to understand which chemical reactions are possible. This evaluation can be made using the second law of thermodynamics. Under conditions of constant temperature and pressure, it is most convenient to use the Gibbs free energy of the system G',

$$G' = H' - TS' \tag{2.1.1}$$

where H', is the enthalpy of the system, T is the absolute temperature and S' is the entropy of the system. At constant temperature and pressure, changes in the Gibbs free energy can be divided into three categories.

$\Delta G' < 0$ spontaneous reaction expected

$\Delta G' = 0$ equilibrium

$\Delta G' > 0$ thermodynamically impossible process

For a generic chemical reaction,

$$aA + bB = cC + dD \tag{2.1.2}$$

the change in the Gibbs free energy $\Delta G'$ can be expressed

$$\Delta G' = \Delta G^{\circ} + RT \ln\left(\frac{a_C^c a_D^d}{a_A^a a_B^b}\right) + \Delta G_{Surface} \tag{2.1.3}$$

where a is the activity and $\Delta G°$ is the change in Gibbs free energy when all of the components are in their standard states and $\Delta G_{Surface}$ is the change in free energy from the creation and destruction of surfaces and interfaces of the products and the reactants. The nature of the quantity $\Delta G_{Surface}$ will be described in Section 2.2. Further, the activity is defined as

$$a_i \equiv \frac{f_i}{f_i^\circ} \cong \frac{p_i}{p_i^\circ} \tag{2.1.4}$$

where f_i is the fugacity of a substance i and f_i° is the fugacity of a pure component i. Under most circumstances, the fugacity can be assumed to be equal to the partial pressure, p_i, to a good approximation.

In the case of an oxide, A_zO submerged in a liquid metal, M, the displacement reaction can be written,

$$yM + A_zO = M_yO + zA \tag{2.1.5}$$

where y and z are stoichiometric coefficients.

Neglecting surface energy, the change in Gibbs free energy for this reaction can be written

$$\Delta G' = \Delta G° + RT \ln\left(\frac{a_A^z a_{M_yO}}{a_M^y a_{A_zO}}\right) \tag{2.1.6}$$

Using this approach, the thermodynamic stability for the creation of other compounds such as $A_rM_sO_t$ and M_xA can be analyzed.

2.2 SURFACE THERMODYNAMICS

2.2.1 Surface energy and surface stress

Surface energy is the fundamental quantity that describes the increase in energy that a bulk phase experiences, when surface is created. Specifically, the work necessary to reversibly create new surface, at constant temperature and pressure, on a given phase *S*, is the surface energy, σ_S (J/m^2) and can be related to the total free energy of the system *G* and the area of the surface created *A*, by Equation 2.2.1.

$$\sigma = \left(\frac{\partial G}{\partial A} \right)_{T,P,n_i} \tag{2.2.1}$$

The surface energy is a scalar quantity which is determined by the nature of the surface.

Surface energy can also be described atomistically. Consider a solid metal. Metal atoms in the bulk of the solid are coordinated with a fixed number of other atoms, *Z*, the coordination number, while atoms located on the surface of the solid are in contact with fewer atoms. Because the atoms in the solid lower their energy by being bonded to an equilibrium number of other atoms, atoms on the surface have higher energy.

The metal-metal bond energy ε_{SS} can be related to the molar heat of sublimation, ΔH_S^S.

$$\Delta H_S^S = -Z \frac{\varepsilon_{SS}}{2} N_A \tag{2.2.2}$$

where N_A is Avogadro's number. The heat of sublimation is the energy necessary to free a mole of atoms in the solid from the bonds of it neighbors, and release it to the gas phase. Neglecting entropic contributions, the surface energy of the solid can be expressed in terms of this bond energy

$$\sigma_S = -\frac{Zm}{\omega}\frac{\varepsilon_{SS}}{2}N_A = \frac{m}{\omega}\Delta H_S^S \qquad (2.2.3)$$

where m is the fraction of broken bonds at the surface, and ω is the surface area per atom.

Similarly, the surface free energy of a liquid can be defined in terms of the heat of vaporization, ΔH_L^V.

$$\sigma_L = -\frac{Zm}{\omega}\frac{\varepsilon_{LL}}{2}N_A = \frac{m}{\omega}\Delta H_L^V. \qquad (2.2.4)$$

Figure 1, expresses the surface free energy of liquid metals as a function of the heat of vaporization.

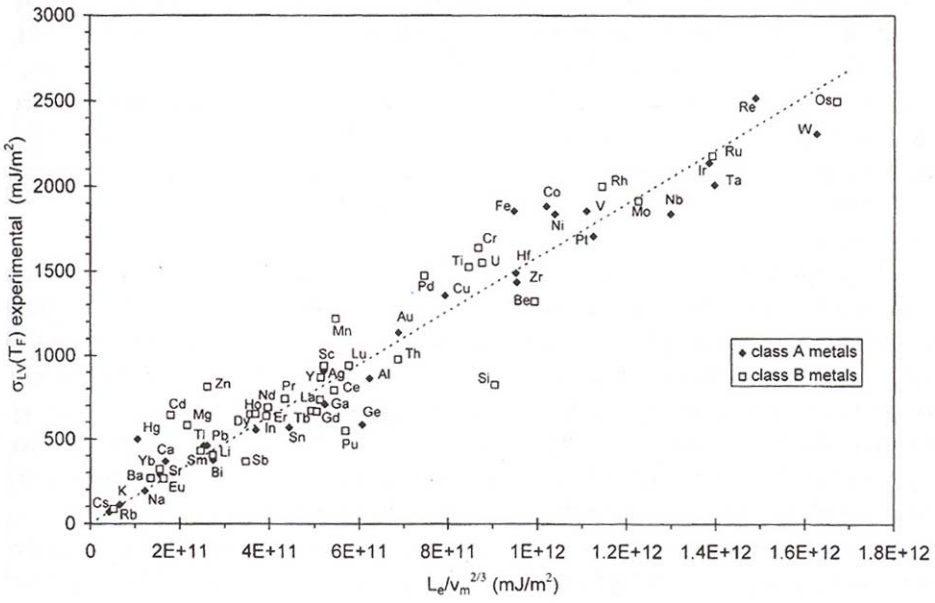

Figure 1. Experimental surface energies of liquid metal at their melting temperature plotted as a function of their heat of vaporization and molar volume.[7]

Alternatively, the surface area of a condensed phase can be increased while keeping the same number of atoms present at the surface, but straining the interatomic bonds. The extension of the surface due to elastic strain was termed the 'surface tension' by Gibbs[8], and has also been called the surface stress. The surface stress, $\underline{\boldsymbol{\gamma}}$, is a second order tensor quantity.

The structure of a liquid prevents the extension of the surface from occurring in any other way than by adding new atoms to the surface. Consequently, the quantities σ_L and $\underline{\boldsymbol{\gamma}}_L$ are identical for pure liquids. In solids, the interatomic spacing of atoms on the surface can be

stretched or compressed. Therefore, the surface energy and the surface stress are different quantities. Shuttleworth[9] has related the two quantities by the expression

$$\underline{\gamma}_S = \sigma_S + \frac{d\sigma_S}{d\underline{\varepsilon}} \tag{2.2.5}$$

where $\underline{\boldsymbol{\varepsilon}}$ is the macroscopic strain tensor. Physically, the second term in equation 2.2.5 can be viewed as the change in the bonding energy of the surface atoms as a result of elastic strain.

The bonding in many solids is anisotropic and as a result, the energy necessary to stretch bonds on the surface will change with direction along the surface. Therefore, the surface stress $\underline{\boldsymbol{\gamma}}$ of a solid will depend on the symmetry of the surface.

Unless otherwise noted, in this work it will be assumed that solid interfaces are isotropic and unstrained. Consequently, the surfaces stress will be assumed to be equal to the surface energy.

2.2.2 Interfacial energy

The fundamental quantity that describes the energy change that accompanies the creation of an interface between two condensed phases, *S* and *L*, is the interfacial energy σ_{SL}. The expansion of the *SL* interface can be viewed as three processes: the creation of *SL* bonds, the destruction of *SS* bonds, and the destruction of *LL* bonds.

Using the method applied previously in the determination of surface energy in terms of bond energies, the solid-liquid interfacial energy can then be defined. In terms of liquid-liquid, solid-solid, and solid-liquid bond energies

$$\sigma_{SL} = -\frac{Zm}{\omega}\left(\varepsilon_{SL} - \frac{\varepsilon_{SS} + \varepsilon_{LL}}{2}\right)N_A = \frac{m}{\omega}\left(\Delta H_S + \Delta H_L - \Delta H_{SL}\right) \tag{2.2.6}$$

where it is assumed that coordination across the *SL* interface is the same as in the *S* and *L* phases.

.

2.2.3 Work of Adhesion

Using the fundamental quantities surface energy and the interfacial energy, a useful quantity, the work of adhesion can be defined. The work of adhesion, W_A, is the energy which bonds two surfaces together, and as defined by Dupre[10],

$$W_A = \sigma_S + \sigma_L - \sigma_{SL} \tag{2.2.7}$$

or in terms of bond energies as

$$W_A = \left(-\frac{Zm}{\omega}\frac{\varepsilon_{SS}}{2} - \frac{Zm}{\omega}\frac{\varepsilon_{LL}}{2} + \frac{Zm}{\omega}\left(\varepsilon_{SL} - \frac{\varepsilon_{SS} + \varepsilon_{LL}}{2}\right)\right)N_A = \frac{Zm}{\omega}\frac{\varepsilon_{SL}}{2} = \Delta H_{SL} \tag{2.2.8}$$

2.2.4 Work of Immersion

Another quantity, useful in the description of the thermodynamics of surfaces, is the work of immersion, W_I, which can be defined in terms of a classic capillary rise experiment.

If a capillary tube, with radius r, is lowered into a liquid, the height of the liquid will remain the same if the surface energy at the liquid-capillary interface, σ_{SL}, is equal to the solid surface energy σ_S, Figure 2a. The height of the liquid in the capillary will rise a distance h above the height of the liquid outside of the capillary if σ_S-$\sigma_{SL}>0$ Figure 2b.

The height, h, defined as the positive direction as down, can be calculated by performing an energy balance. The change in energy due to the displacement of liquid into the capillary tube is due to two factors: first, the change in surface energy that results from the creation of liquid-solid interface and the destruction of solid-vapor interface, and second, there will be the change in energy from displacement of the liquid against gravity.

$$E = (\sigma_S - \sigma_{SL})2\pi rh + \rho g \pi r^2 h\left(\frac{h}{2}\right) \tag{2.2.9}$$

The minimum energy can be found setting $\frac{dE}{dh} = 0$

$$h = \frac{2(\sigma_{SL} - \sigma_S)}{\rho g r} \tag{2.2.10}$$

Similarly, the liquid will be depressed in the capillary tube if σ_S-$\sigma_{SL}<0$, Figure 2c. The quantity (σ_{SL}-σ_L) is the work of immersion, because it quantifies the energy change when a unit area of solid-vapor interface is replaced by solid liquid interface.

$$W_I = \sigma_{SL} - \sigma_S \tag{2.2.11}$$

or in terms of bond energies

$$W_I = \frac{Zm}{\omega}\left(\varepsilon_{SL} - \frac{\varepsilon_{SS}}{2}\right)N_A = \Delta H^{\circ}_{SL} - \Delta H^{\circ}_{SS} \qquad (2.2.12)$$

where ΔH°_{SL} is the heat of formation of *SL*.

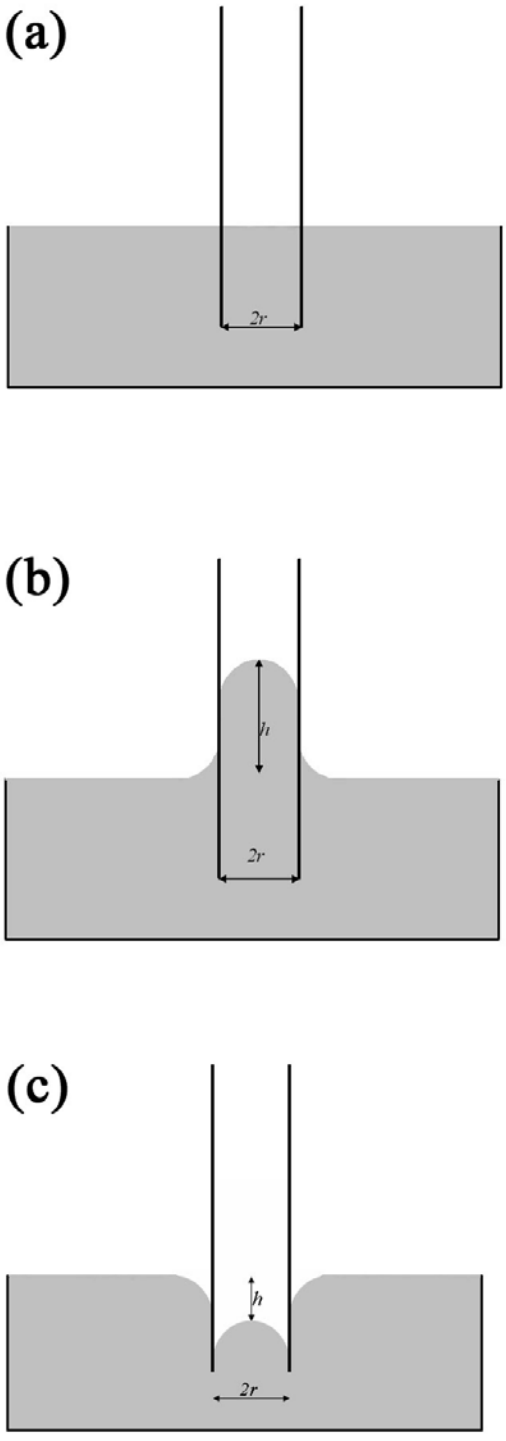

Figure 2. Capillary rise experiment when σ_{SL}-σ_S is (a) zero (b) negative (c) positive

2.2.5 Young's Equation

Historically, a convenient method of determining the surface energies of a liquid-solid system has been through the sessile drop experiment, Figure 3. When a liquid droplet is brought in contact with an undeformable, perfectly flat, chemically homogenous solid, the shape of the droplet will change, minimizing the free energy of the system. If the droplet is sufficiently small, gravity can be neglected, the energy can be minimized by varying the interfacial area.

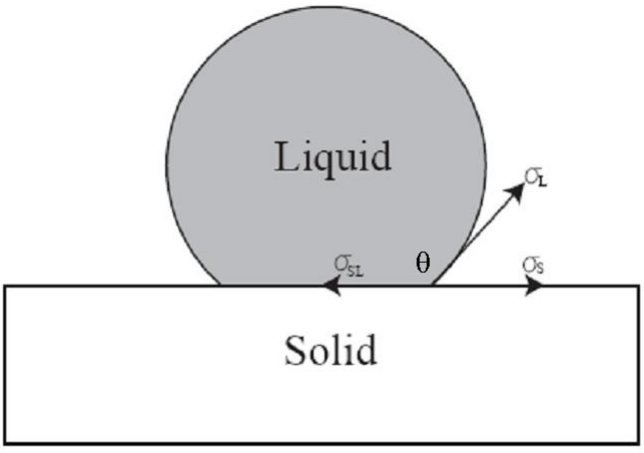

Figure 3. Sessile drop

At the three-phase interface between solid, liquid, and gas, the triple line, a force balance must exist. If it is assumed that the solid and the liquid are isotropic and that the surface stress $\underline{\gamma}$ is equal in magnitude to the surface energy, then the change in surface energy as a result of an increase in the length z of the triple line can be expressed as

$$G(z+\delta z)-G(z)=\Delta G=(\sigma_S-\sigma_{SL})\delta z+\cos\theta\sigma_L\delta z \qquad (2.2.13)$$

The equilibrium condition can be found by setting

$$\frac{d\Delta G}{dz} = 0 \tag{2.2.14}$$

which results in the classical expression of Young's Equation[11].

$$\cos\theta = \frac{\sigma_S - \sigma_{SL}}{\sigma_L} \tag{2.2.15}$$

2.2.6 Young-Dupré Equation

The contact angle between a solid and a liquid can be expressed in terms of the work of adhesion, by substituting Equation 2.2.7, into Equation 2.2.15.

$$\cos\theta = \frac{W_A}{\sigma_L} - 1 \tag{2.2.16}$$

This expression is the Young-Dupré Equation.[10] It is a useful expression because it expresses the contact angle's relationship to the cohesive forces between the solid and the liquid, W_A and the cohesive forces in the liquid σ_L.

2.2.7 Laplace Equation

It is also useful to relate the surface energy of a liquid to pressure. A straight forward example of this relationship is the expansion of a spherical bubble, with surface stress γ_L. The change in energy to expand a bubble with a radius r a distance dr will be.

$$dG = 4\pi r^2 \gamma_L dr + \frac{4}{3}\pi r^3 \Delta P dr \tag{2.2.17}$$

where ΔP is the pressure difference between the inside and the outside of the bubble.

Finding the minimum energy configuration results in

$$\Delta P = \frac{2\gamma_L}{r} \tag{2.2.18}$$

the Laplace Equation. [12]

2.3 GAS-LIQUID INTERACTIONS

The description of solid and liquid surfaces given in Section 2.2.1 assumes that there is no interaction between the condensed phase and the environment around it. This is a reasonable description of pure metals in high vacuum, but in many cases, condensed phases will be adjacent to a gas phase. Gibbs has considered this system and modeled the boundary between the two phases to be a distinct interphase, having properties different from the bulk of the two phases, which can be viewed as an infinitely thin, uniform membrane.[8]

It is necessary that the interface is in a state of stress, different from both adjacent bulk phases, such that mechanical equilibrium can be obtained. This is the previously described surface stress. Additionally, the chemical composition of the interface can be different from the composition of the adjacent bulk phases. Gibbs has described the adsorption of a component *i* on a surface,

$$\Gamma_i = \frac{n_i^S}{A} \tag{2.3.1}$$

where n_i^S are number of moles of *i* on the dividing surface, A is the surface area and Γ_i is the absolute adsorption if *i* having units mol/cm^2.

If the solution of a gas *i* onto a liquid *j* is considered, in which the concentration of the gas phase in the liquid is dilute, the relative adsorption of *i* onto *j* can be expressed

$$\Gamma_{i,j} = \Gamma_i - \Gamma_j \frac{X_i}{X_j} \tag{2.3.2}$$

where X_i and X_j are the respective mole fractions the species *i* and *j* in the bulk liquid.[13] When the quantity $\Gamma_{i,j}$ is positive, it means the interface is enriched in *i*, with respect to the bulk composition, while if $\Gamma_{i,j}$ is negative, it means that the surface is denuded in *i*. Using the relative adsorption coefficient, Defay and Prigogine have developed an expression for the change in surface tension of a liquid as a function of the partial pressure of that species in the gas phase p_j.[13]

$$d\sigma_i = -RT\Gamma_{j,i} d \ln p_j \tag{2.3.4}$$

2.4 LIQUID-SOLID INTERACTIONS

Many different types of forces can influence the wetting properties of liquids on solids. These forces can be grouped into three basic categories. Listed by increasing strength, these forces are: the coulombic forces; the attraction between charged particles, polarization forces; the attraction between distorted charge centers, and quantum mechanical forces; the attraction due to chemical bonding.[14] The force, or forces which predominates the solid-liquid interfacial bonding of a given system, will depend on the chemical nature of the liquid and solid components.

In liquid metal-ceramic systems, all of the above forces can be present. In general, the degree of wetting increases with the strength of bonding at the metal-ceramic interface.[7] In systems which are weakly bonded, the predominant forces are coloumbic and polarization based, and can be characterized as van der Waals forces. These systems typically have a weak thermodynamic driving force for reaction, and no new phases are created at the metal-ceramic interface. As the attraction between a liquid and a ceramic phase increases, the amount of dissolution of the ceramic into the metal will increase and the interfacial bond strength is influenced by physical van der Waals forces along with chemical bonding. It has been shown that as the extent to which a ceramic will dissolve into a metal increases, so does the wettability of that system. As the strength of the interactions increases further, the thermodynamic driving force for interaction between the metal and the ceramic will be sufficient to form new phases. In this situation, the adhesion and wettability between the metal and the ceramic is general good,

and properties of the system depend upon the nature of the interactions between the liquid and the new phase which has been created.

2.4.1 Non-Reactive Metal-Oxide Systems

A chemical reaction between M and A_zO will proceed if the free energy of reaction is negative, as described in Equation 2.1.6. However, even without the formation of a new phase, chemical bonding may still be a primary contributor to the adhesion between M and A_zO. Over the years, a number of models have been developed to relate the physical properties of metals and oxides to the contact angle, and the work of adhesion.[15-19] Eustathopoulos and Drevet[16] have collected the contact angles of many metal-oxide systems, and calculated the equilibrium mole fraction of dissolved oxygen, X_O, at the metal-oxide interface. These authors found that when there was only a small amount of oxide dissolution, $X_O<10^{-5}$, the contact angle was in the range of 110-140°, and was not a function of X_O. As the amount of dissolved oxygen increased above $X_O>10^{-5}$, the contact angles were found to decrease monotonically with increasing X_O.

The contact angle, of metals on oxide systems in which there is little oxide dissolution, is high, due to the weak adhesive forces at the metal-oxide interface. In these systems, there is little chemical interaction between the metal and the oxide and adhesion is primarily due to physical interactions. *Lipkin et al.*[20] have determined the magnitude of the van der Waals forces at these interfaces and the calculated work of adhesion, agrees well with experimentally measured W_A values.

As the amount of oxide dissolution increases, chemical interactions play an increasingly important role in adhesion. Naidich[21], has proposed that oxygen dissolved in the metal will tend to form metal-oxygen complexes which have partially ionic and partial covalent (metallic) bonding behavior. The localization of the electrons in the cluster decreases the bond strength between the cluster and the atoms in the liquid metal, which leads the clusters to segregate to two-dimensional defects, like the liquid-vapor and solid-liquid interfaces.

At the solid-liquid interface, the charged metal species in the cluster is coulombically attracted to oxygen anions in the oxide. The bond between the cluster and the oxide surface is stronger than the bond between the neutral metal atoms and oxide surface, which decreases the metal-oxide interfacial energy, and as a result, the contact angle decreases as the amount of oxide dissolution increases.

2.4.1.1 Oxide Dissolution

Consider the pure liquid metal *M* in contact with the oxide A_zO. The dissolution of A_zO into *M* can be described by the reaction

$$A_zO = z\underline{A} + \underline{O} \tag{2.4.1}$$

where $\underline{A}$ and $\underline{O}$ denotes species dissolved in *M*.[16] This reaction can be viewed as the summation of three processes:

$$A_zO = zA + \tfrac{1}{2}O_{2(g)} \tag{2.4.2}$$

$$zA = z\underline{A} \tag{2.4.3}$$

$$\tfrac{1}{2}O_{2(g)} = \underline{O} \tag{2.4.4}$$

If activity of $\underline{A}$ is defined in reference to the standard state of pure liquid A, and the activity of $\underline{O}$ is defined in reference to the standard state of oxygen gas at 1 atm, then the standard free energy change for the Equations 2.4.3 and 2.4.4 is zero[1].

$$\Delta G_2^\circ = -\Delta G_{A_zO}^\circ \tag{2.4.5}$$

Further, at equilibrium, the free energy change for Equation 2.4.1 is zero. The ratio of activities of the oxide and the dissolved species can be expressed in terms of the equilibrium constant K

$$K = \exp\left(\frac{\Delta G_{A_zO}^\circ}{RT}\right) = \frac{a_{\underline{A}}^z a_{\underline{O}}}{a_{A_zO}} \tag{2.4.6}$$

When the activity of the oxide is unity, and activities of the dissolved species in the metal are sufficiently dilute so that they obey Henry's law, Equation 2.4.6 can be simplified.

$$K = \left(\gamma_A^\circ X_A\right)^z \left(\gamma_O^\circ X_O\right) \tag{2.4.7}$$

Further, the activity coefficients of A and O can be related to the partial excess free energies.

$$\gamma_A^\circ = \exp\left(\frac{\overline{G}_A^{xs}}{RT}\right) \qquad \gamma_O^\circ = \exp\left(\frac{\overline{G}_O^{xs}}{RT}\right) \tag{2.4.8}$$

The equilibrium oxygen concentration can now be expressed in terms of the partial free energies of mixing, and the free energy of formation of A_zO.

$$\left(X_A\right)^z X_O = \exp\left(\frac{\Delta G_{A_zO}^\circ - zG_A^{xs} - G_O^{xs}}{RT}\right) = K' \tag{2.4.9}$$

---

[1] The choice of standard states in reactions 2.4.3 and 2.4.4, were selected to follow the derivation of Eustathopoulos and Drevet. Equation 2.4.9 can also be obtained if the standard states of A and O are changed to the mole fraction of each component in solution in M, as is commonly done in the literature, which changes the value of K in Equation 2.4.6, and changes the activity coefficients in Equation 2.4.8 to unity.

A convenient way to view the range of equilibrium compositions which can exist between *M* and A_zO, assigned by Equation 2.4.9, is an isothermal section of the *M-A-O* ternary phase diagram, Figure 4. Applying the Gibbs' Phase Rule, $F=C-P+2$, to the $M-A_zO$ couple; a two phase, three component system, there is one degree of freedom, at constant temperature and pressure. Therefore, in order to determine the particular equilibrium concentration X_O and X_A, the kinetics of the system need to be considered.[22]

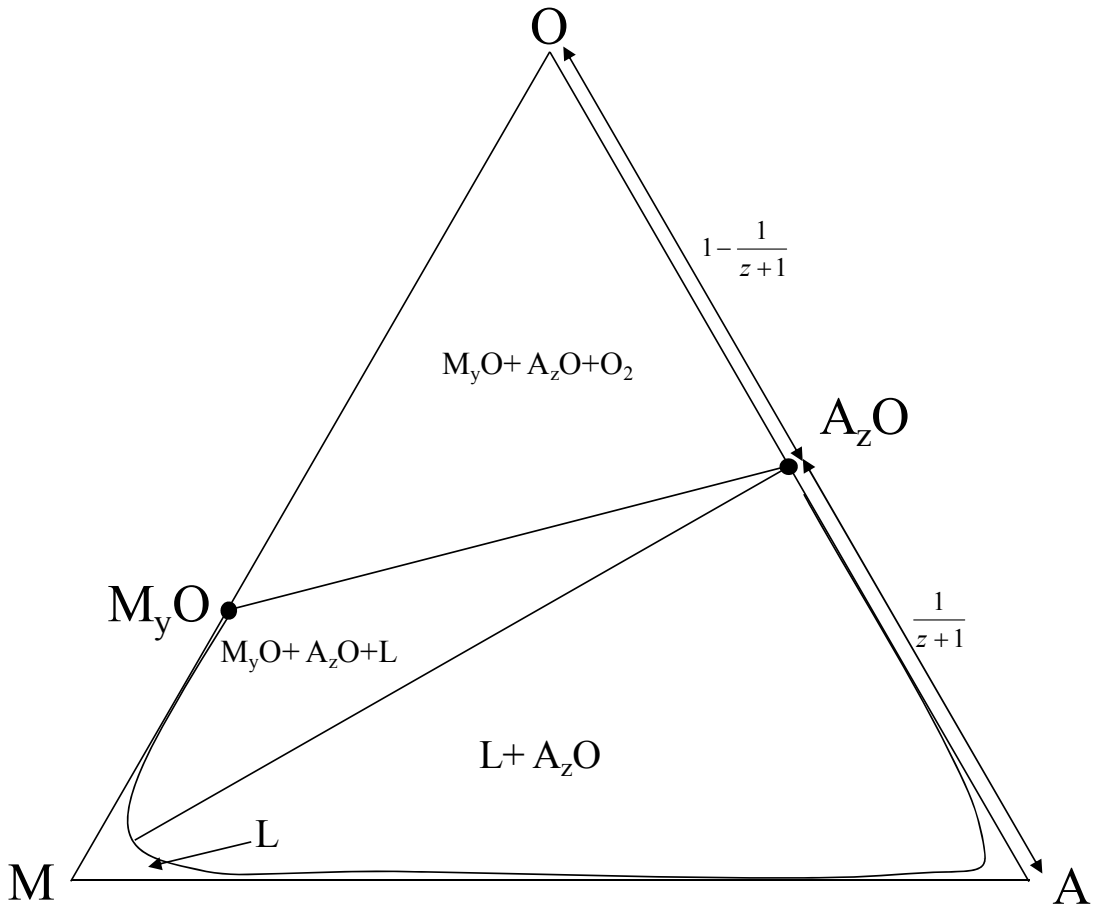

Figure 4. Schematic isothermal section of a ternary phase diagram

In previous work, it was assumed that the diffusion path between *M* and A_zO was a straight line. This is the best first approximation, but a straight line diffusion path cannot be assumed *a priori*. [17]The theoretical calculation of the diffusion path of a diffusion couple requires knowledge of the thermodynamic and kinetic data for the systems, and in most cases, such an analysis is complicated at best. However, in this work, a relatively simple system is being analyzed and a general method for determining the equilibrium *M-O-A* compositions can be determined.

First, if the dissolution process is diffusion controlled, and convection can be ignored, the flux of each component in to the metal will be governed by Fick's 1st Law

$$J_i = -D_i \frac{\partial X_i}{\partial x} \tag{2.4.10}$$

The actual flux of the each component will depend on the geometric configuration of the liquid metal into which the components are diffusing, but if the metal thickness is much greater than the diffusion distance of *A* and *O*, then the diffusive profiles are in the form of an error function solution to Fick's 2nd Law, where *A* and *B* are constants,

$$X_i = A + Berf\left(\frac{x}{\sqrt{4D_i t}}\right) \tag{2.4.11}$$

which is subject to the boundary conditions

1. $x = \infty$ $X_O = 0$ $X_A = 0$ $t = t$
2. $x = -\xi$ $X_O = X_O^*$ $X_A = X_A^*$ $t = t$ [2]

[2] The second boundary condition, the concentration of *A* and *O* are constant at all times, is generally not true for non-infinite metal-oxide couples. The ratio of the concentrations of *A* and *O* are only bound to remain in

The distance that the interface has moved, ξ, will increase parabolically with time, if the dissolution process is controlled by diffusion, which can be expressed as $\xi = \sqrt{k_p t}$, where k_p is the parabolic dissolution constant. The dissolution process can also be expressed in terms of the oxygen diffusivity, $\xi = 2\gamma\sqrt{D_O t}$, where, γ, is a dimensionless constant. The concentration profiles of *A* and *O* can now be expressed as

$$X_A = \frac{X_A^*}{1 + erf\left(\frac{\xi}{\sqrt{4D_A t}}\right)} erfc\left(\frac{x}{\sqrt{4D_A t}}\right) \tag{2.4.12}$$

$$X_O = \frac{X_O^*}{1 + erf\left(\frac{\xi}{\sqrt{4D_O t}}\right)} erfc\left(\frac{x}{\sqrt{4D_O t}}\right) \tag{2.4.13}$$

The ratio of the diffusivities is now defined as $\Theta = \frac{D_O}{D_A}$ and substituting Equations 2.4.12 and 2.4.13 into 2.4.11 produces

$$J_A^M = -D_A \frac{2}{\sqrt{\pi}} \frac{X_A^*}{\left[1 + erf\left(\gamma\Theta^{1/2}\right)\right]\sqrt{4D_A t}} \exp\left(\frac{-x^2}{4D_A t}\right) \tag{2.4.14}$$

$$J_O^M = -D_O \frac{2}{\sqrt{\pi}} \frac{X_O^*}{\left[1 + erf\left(\gamma\right)\right]\sqrt{4D_O t}} \exp\left(\frac{-x^2}{4D_O t}\right) \tag{2.4.15}$$

Due to the volume change associated with the dissolution of A_zO, there is a drift velocity of the interface.[23]

---

thermodynamic equilibrium, Equation 7, at the metal-oxide interface. However, it will be shown, that the values of X^*_A, and X^*_O are time independent.

$$J_O^{A_zO} = \frac{d\xi}{dt}\left(1 - \frac{\overline{V}_{A_zO}}{\overline{V}_M}\right) \tag{2.4.16}$$

$$J_A^{A_zO} = \frac{d\xi}{dt}\left(1 - \frac{\overline{V}_{A_zO}}{\overline{V}_M}\right) \tag{2.4.17}$$

Applying a mass balance, the flux of each component is related to the interfacial compositions.[23]

$$\left(X_O^{A_zO} - X_O^*\right)\frac{d\xi}{dt} = J_O^{A_zO} - J_O^M \tag{2.4.18}$$

$$\left(X_A^{A_zO} - X_A^*\right)\frac{d\xi}{dt} = J_A^{A_zO} - J_A^M \tag{2.4.19}$$

Substituting Equations 2.4.14, and 2.4.16 into Equation 2.4.18, and Equations 2.4.15, and 2.4.17, into Equation 2.4.19, yield Equations 2.4.20, and 2.4.21, respectively.

$$\left(X_A^{A_zO} - X_A^*\right)\frac{d\xi}{dt} = \frac{d\xi}{dt}\left(1 - \frac{\overline{V}_{A_zO}}{\overline{V}_M}\right) + D_A \frac{2}{\sqrt{\pi}} \frac{X_A^*}{\left[1 + erf\left(\gamma\Theta^{1/2}\right)\right]\sqrt{4D_A t}} \exp\left(\frac{-x^2}{4D_A t}\right) \tag{2.4.20}$$

$$\left(X_O^{A_zO} - X_O^*\right)\frac{d\xi}{dt} = \frac{d\xi}{dt}\left(1 - \frac{\overline{V}_{A_zO}}{\overline{V}_M}\right) + D_O \frac{2}{\sqrt{\pi}} \frac{X_O^*}{\left[1 + erf\left(\gamma\right)\right]\sqrt{4D_O t}} \exp\left(\frac{-x^2}{4D_O t}\right) \tag{2.4.21}$$

Rearranging Equations 2.4.20 and 2.4.21 and substituting Equation 2.4.9 yields

$$K' = \left(\frac{\left(X_O^{A_zO} + \dfrac{\overline{V}_{A_zO}}{\overline{V}_M}\right)}{1 + \dfrac{1}{\sqrt{\pi}} \dfrac{\exp\left(-\gamma^2\right)}{\gamma\left[1 + erf\left(\gamma^{1/2}\right)\right]}}\right)\left(\frac{\left(X_A^{A_zO} + \dfrac{\overline{V}_{A_zO}}{\overline{V}_M}\right)}{1 + \dfrac{1}{\sqrt{\pi\Theta}} \dfrac{\exp\left(-\Theta\gamma^2\right)}{\gamma\left[1 + erf\left(\gamma\Theta^{1/2}\right)\right]}}\right)^z \tag{2.4.22}$$

which can be solved numerically for X_O^*, X_A^*, and γ

2.4.1.2 Chemical equilibrium in the sessile drop system

In the sessile drop experiment, chemical equilibrium between the gas and liquid phase must be achieved, in addition to the equilibrium between the solid and liquid phases, which was described in the previous section. In the case of the *M-O₂* system, the chemical potential of oxygen in the gas phase must be equal to the chemical potential of oxygen dissolved in the metal, at the metal gas interface. This equilibrium is described by the expression

$$p_{O_2}^{1/2} = a_{\underline{O}} = \gamma_O^{\circ} X_O \qquad (2.4.23)$$

where the activity of dissolved oxygen is with respect to pure oxygen gas, at a pressure of one atmosphere as a standard state and it is assumed that the concentration of oxygen in the metal is small and obeys Henry's Law.

If the *pO₂* in the gas phase is greater than $p_{O_2}^{*\,1/2}$ where

$$p_{O_2}^{*\,1/2} = \gamma_O^{\circ} X_O^{*} \qquad (2.4.24)$$

and, X_O^{*}, is the mole fraction of oxygen calculated by Equation 2.4.22 then there will be a gradient in the oxygen activity across the sessile drop. The activity gradient will drive the diffusion of oxygen from the gas-metal interface toward the metal-oxide interface. The rate at which oxygen is added to the droplet will depend on the oxygen activity difference between the atmosphere and the dissociation pressure of A_zO, the diffusivity of oxygen in the metal, and the size of the droplet. However, after a sufficiently long time, a uniform concentration will be reached across the droplet. In most metals, the diffusivity of oxygen is high, and the radius of the liquid metal is small, and as a result, equilibrium can be reached in a matter of minutes. The

concentration of oxygen in the liquid metal is schematically represented in Figure 5, where the sessile drop configuration is idealized as a finite diffusion couple of length L.

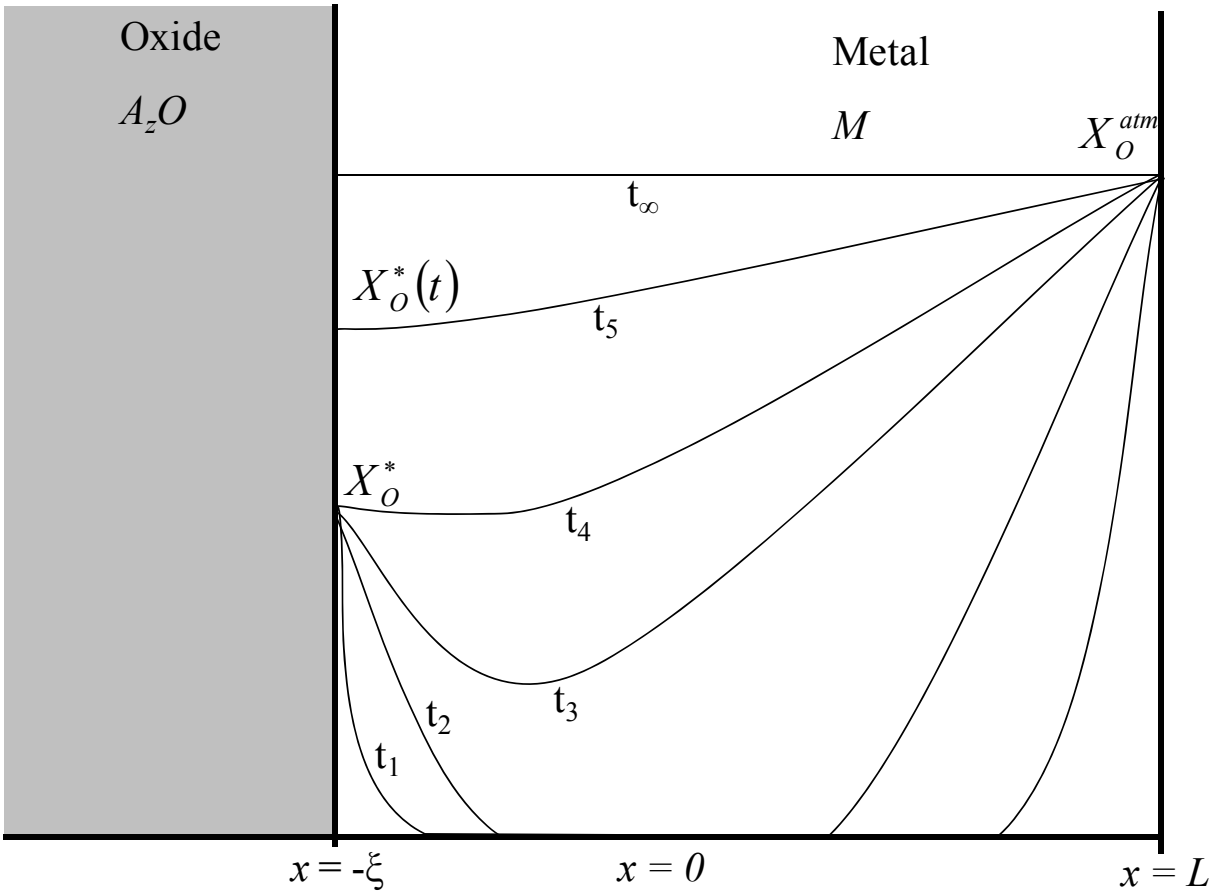

Figure 5. Oxygen concentration profiles in a A_zO-M diffusion couple of finite thickness

.

2.4.1.3 Bonding in non-reactive systems

Among the forces that may act between two surfaces, van der Waals interactions are always present.[14] Van der Waals interactions are electrodynamic in origin and arise from the interaction between oscillating or rotating, molecular or atomic diploes. There are three types of interactions that contribute to the van der Waals force:

(i) the Keeson force, which results from interaction between two permanent dipoles,
(ii) the Debye force, which results from interactions between on permanent dipole and one induced dipole and
(iii) the London or dispersion force, which results from two induced dipoles.

The spatial dependence of the van der Waals force can be illustrated by considering two harmonic oscillators 1 and 2 separated by a distance R, as derived by Kittel.[24] The change in energy associated with the interaction of these oscillators is

$$\Delta U = -\frac{-\hbar\omega_{\circ}e^4}{4C^2R^6} \qquad (2.4.25)$$

where C is the force constant of the oscillator, e is the charge on each of the oscillators components, h is Planck's constant, and ω_0 is the highest optical absorption frequency.

Similarly, the van der Waals force between two molecules can be described by the equation, [14]

$$E_{vdW} = \frac{I_1 I_2}{I_1 + I_2}\frac{\alpha_1\alpha_2}{R^6} \qquad (2.4.26)$$

where I_i is the first ionization potential and α_i is the polarizability of the species i.

Hamaker[25] has developed a model to calculate the free energy between two bodies by performing a pair-wise summation over all the atoms in the bodies. The van der Waals energy as a function of distance between the two bodies is now

$$E_{vdW} = \frac{A}{12R^2} \tag{2.4.27}$$

where A is the Hamaker constant, which is a material property of the system.

However, the Hamaker analysis uses the physical properties of the molecular species in each of the bodies, and ignores the many-body effects, which can significantly affect the electronic structure of condensed phases. In order to incorporate many-body effects, Lifschitz has developed an alternative model which treats the bodies as a continuum with certain dielectric properties. [20, 25-26]

The Lifshitz continuum model describes the interaction of solids 1 and 2, acting through a medium 3. The Hamaker constant A can be expressed as

$$A = \tfrac{3}{4} k_B T \left(\frac{\varepsilon_1 - \varepsilon_3}{\varepsilon_1 + \varepsilon_3} \right) \left(\frac{\varepsilon_2 - \varepsilon_3}{\varepsilon_2 + \varepsilon_3} \right) + \frac{3h}{4\pi} \int_{\nu_1}^{\infty} \left(\frac{\varepsilon_1(i\nu) - \varepsilon_3(i\nu)}{\varepsilon_1(i\nu) + \varepsilon_3(i\nu)} \right) \left(\frac{\varepsilon_2(i\nu) - \varepsilon_3(i\nu)}{\varepsilon_2(i\nu) + \varepsilon_3(i\nu)} \right) d\nu \tag{2.4.28}$$

where ε is the static dielectric constant, and ε($i\nu$) is the frequency dependent dielectric constant, and $\nu = 2\pi k_B T/h$. The first term gives the zero-frequency contribution to the van der Waals energy and consists of the Keesom and Debye interactions. The second term accounts for the London interactions.

When considering a metal bonding to a ceramic in a vacuum, equation 2.4.28 can be simplified because $\varepsilon = \varepsilon(i\nu) = 1$ for a vacuum, and $\varepsilon_m = \infty$ for a metal.

$$A = \tfrac{3}{4} k_B T \left(\frac{\varepsilon_C - 1}{\varepsilon_C + 1} \right) + \frac{3h}{4\pi} \int_{\nu_1}^{\infty} \left(\frac{\varepsilon_M(i\nu) - 1}{\varepsilon_M(i\nu) + 1} \right) \left(\frac{\varepsilon_C(i\nu) - 1}{\varepsilon_C(i\nu) + 1} \right) d\nu \tag{2.4.29}$$

The frequency dependence of the permittivity of a ceramic can be written

$$\varepsilon_C(i\nu) = 1 + \frac{\varepsilon_C - n_C^2}{1 + \dfrac{\nu}{\nu_{rot,C}}} + \frac{n_C^2 - 1}{1 + \left(\dfrac{\nu}{\nu_{e,C}} \right)^2} \tag{2.4.30}$$

where $\nu_{rot,C}$ is the molecular rotational relaxation frequency in the infrared spectrum, and $\nu_{e,C}$ is the main electronic absorption frequency in the visible or ultraviolet spectrum and n_C is the refractive index of the medium. Typically, the molecular rotation relaxation frequency is small, with $\nu_{rot,C} << \nu_1 << \nu_{e,C}$. Therefore, the contribution of $\nu_{rot,C}$ to the dispersion energy can be neglected. As a result, equation 2.4.30 can be reduced to

$$\varepsilon_C(i\nu) = 1 + \frac{n_C^2 - 1}{1 + \left(\dfrac{\nu}{\nu_{e,C}} \right)^2} \tag{2.4.31}$$

The static dielectric constant of metals is infinite, and the frequency dependent permittivity, derived from the jellium approximation[20], is

$$\varepsilon_M(i\nu) = 1 + \frac{\nu_M^2}{\nu^2 + \dfrac{\nu}{\tau}} \approx 1 + \left(\frac{\nu_M}{\nu} \right)^2 \tag{2.4.32}$$

Combining equations, (2.4.20), (2.4.22) and (2.4.23), and integrating, yields

$$A = \tfrac{3}{4}k_B T\left(\frac{\varepsilon_C - 1}{\varepsilon_C + 1}\right) + \frac{3h}{4\pi}\frac{\left(n_C^2 - 1\right)^{\nu_{e,M}/\nu_{e,C}}}{\sqrt{2\left(n_C^2+1\right)}\left[\left(n_C^2+1\right) - \left(\nu_{e,M}/\nu_{e,C}\right)^2\right]} \left\{\nu_{e,M}\left[\tan^{-1}\left(\frac{\sqrt{2}\nu_1}{\nu_{e,C}\sqrt{n_C^2+1}}\right) - \frac{\pi}{2}\right] - \nu_{e,C}\sqrt{n_C^2+1}\left[\tan^{-1}\left(\frac{\sqrt{2}\nu_1}{\nu_{e,M}}\right) - \frac{\pi}{2}\right]\right\} \quad (2.4.33)$$

The Hamaker function can be simplified by noting that the static dielectric term is small. Furthermore, because $\nu_{rot,C} << \nu_1 << \nu_{e,C}$ the arctangent terms are smaller than $\pi/2$.

$$A \approx \frac{3h}{8}\frac{\left(n_c^2 - 1\right)\nu_{e,m}\nu_{c,m}}{\sqrt{2\left(n_c^2+1\right)}\left(\nu_{e,c}\sqrt{n_c^2+1} + \nu_{e,m}\right)} \quad (2.4.34)$$

Lipkin et al. have used this form of the Hamaker constant to calculate the van der Waals energy between the (111) surface of fcc metals, and the oxygen terminated surface of the basal plane of sapphire. In this model, the fcc lattice is elastically strained so that the metal atoms are sitting in two thirds of the interstitial sites on the sapphire surface. The van der Waals energy can then be expressed as

$$E_{vdW} \approx \frac{\sqrt{3}A}{4\pi^2 r_O} \quad (2.4.35)$$

where r_O is the ionic radius of oxygen in sapphire.

2.4.2 Reactive Systems

In many liquid metal-oxide systems, there is a tendency for chemical reaction to take place. To understand how these multi-phase systems evolve with time, both thermodynamic and kinetic analyses need to be performed. In general, there are a number of phases which can evolve from an M-A_zO couple and it is necessary to consider the free energy change for each reaction, and to consult available phase diagrams. Additionally, because of the thermodynamic degree of freedom in the two phase, three component system, a kinetic analysis must be performed determine the reaction path which describes the layer sequence between the diffusion couple. To determine the overall rate of reaction, the rate limiting reaction process must be determined. If the reaction products remain adherent, diffusional processes generally govern the reaction rate, and the relative fluxes in the layers determine the morphology of the reaction process. If the reaction products do not remain adherent, which is generally caused by the cracking in the product oxide layers as a result from tensile growth stress due to volume contract, the overall rate of reaction is determined by the rate of surface reaction.

2.4.2.1 Thermodynamics

In some liquid metal-oxide systems, chemical reactions occur where new phases are formed. These reactions can be grouped into three general categories:

(a) $$yM + A_zO = M_yO + zA$$

(b) $$yM + A_zO = A_zM_y + \frac{1}{2}O_2 \qquad (2.4.36)$$

(c) $$yM + \frac{x-1}{2}O_2 + A_zO = A_zM_yO_x$$

where types (a) and (b) are displacement reactions, like the reduction of Cu_2O by Ni, or the formation of PtAl when Al_2O_3 is reduced by Pt[27]. The third type of reaction is the formation of a ternary oxide, for example, the reaction of Fe with Cr_2O_3 to form $FeCr_2O_4$. If the free energy change for any of these reactions is negative, it is possible for the reaction to proceed.

2.4.2.2 Kinetics

A wide range of reaction rates are observed in the reaction of liquid metals with solid oxides. In the analysis of the reaction rate, it is important to determine the rate controlling step of the reaction. If an adherent reaction product forms, the rate of reaction is generally controlled by the diffusion through the reaction layer, and the reaction rate decreases with time, as the diffusion distance necessary to continue the reaction increases. On the other hand, if the reaction product does not remain adherent, the rate limiting step will be the surface reaction and the reaction rate tends to be constant with time.

Consider the M-A_zO couple in which the displacement reaction

$$yM + A_zO = M_yO + zA \qquad (2.4.37)$$

is thermodynamically favorable. This type of reaction can proceed in a number of ways. First, it will be assumed that reaction products remain adherent, then there are two possible layer sequences for this reaction (a) $A_zO/A/M_yO/M$ and (b) $A_zO/M_yO/A$-M/M. A schematic of each layer sequence, Figure 6.[22] The nature of the layer sequence has been analyzed by van Loo et

al. who concluded that a component will only diffuse down its own activity gradient, and therefore, layer sequence (a) will exclusively form in systems which do not have a change in slope in the tie lines of their phase diagram, Figure 7.[22] Conversely, systems which do have a sign change in the slope of the tie lines, Figure 8, can form either layer sequence. However, only sequence (b) has been observed.[22]

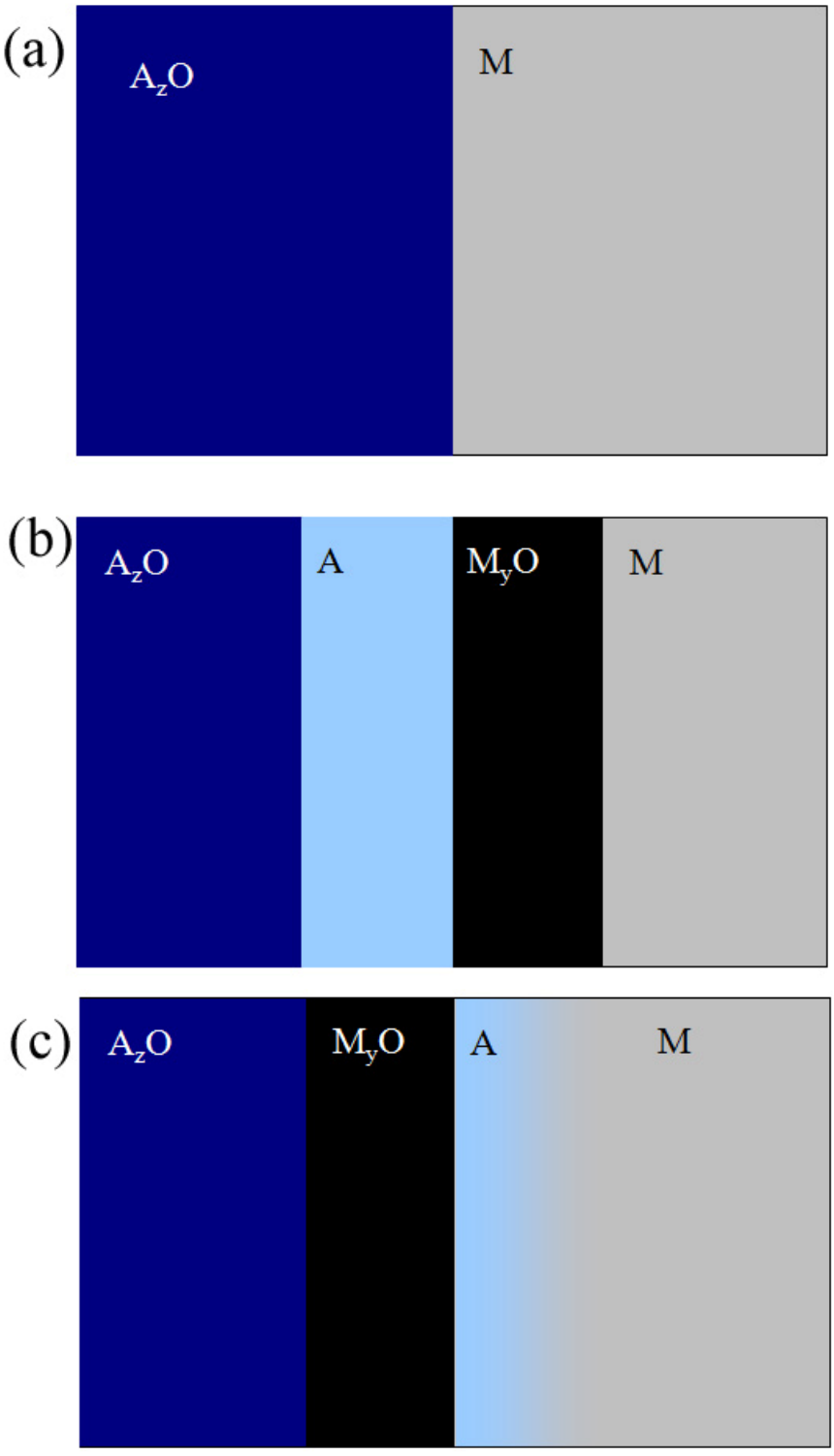

Figure 6. Schemtatic of (a) the initial A_zO-M diffusion couple and after a diffusion anneal (b) and (c)

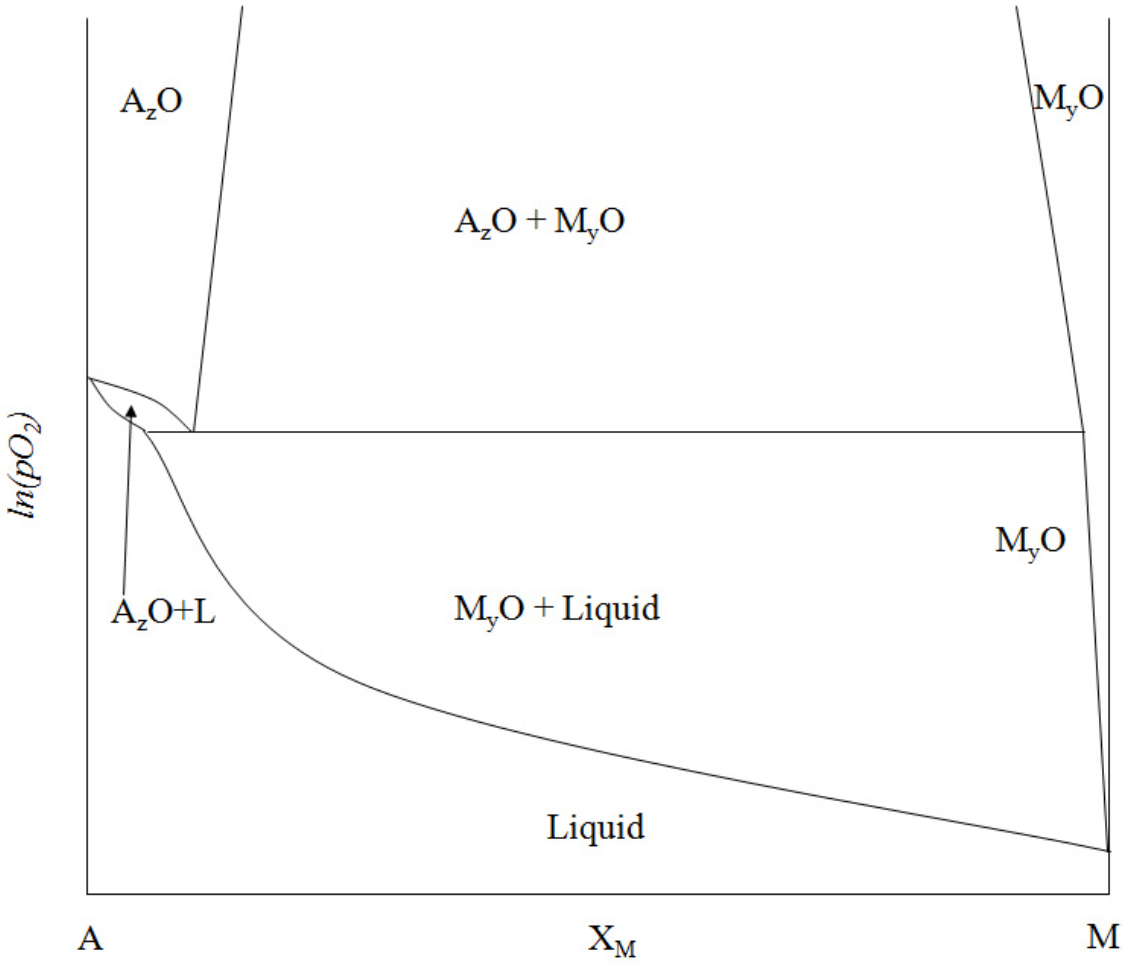

Figure 7. A-M-O composition-oxygen potential ternary phase diagram

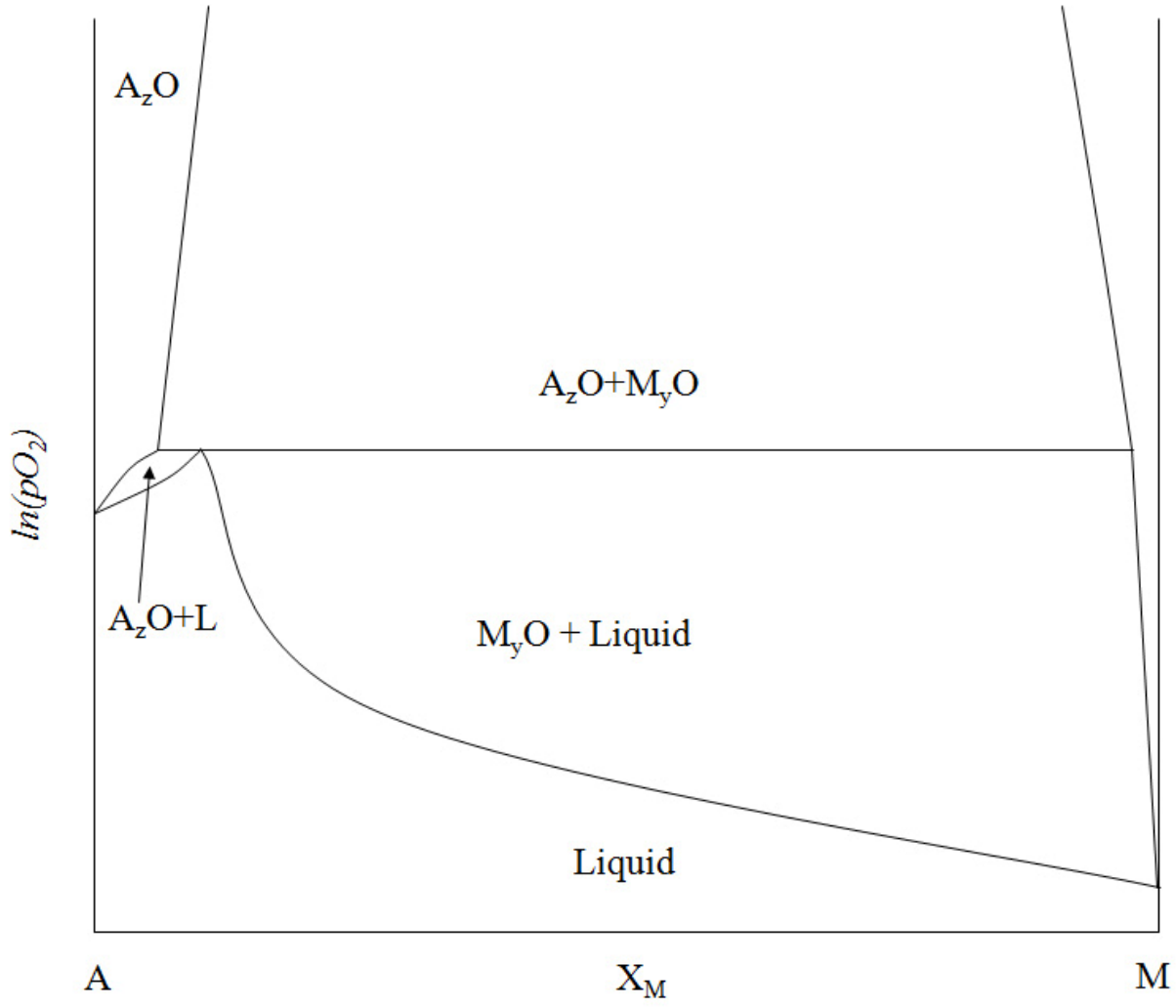

Figure 8. A-M-O composition-oxygen potential ternary phase diagram

Generally, the evolution of both layer sequences will be controlled by diffusion, in analogous manner to the formation of oxides on metals, as described by Wagner[28]. Indeed, Rapp et al,[29] have shown that the growth of oxide layers by displacement reactions in the solid state grow by diffusion controlled processes. In this analysis, Rapp demonstrated that the morphology of the system will depend on the relative fluxes of each component, in each layer. If the layer sequence (a) is considered, where the flux of the metal cations through each oxide is much greater than the flux of oxygen in the oxide, the relevant fluxes, which can control layer growth, are the diffusion of *M* from the *M*-M_yO interface, and the diffusion of *O* through *A*. If the cationic flux of *M* through M_yO is less than the flux of *O* through *A*, the growth of M_yO will be controlled by the flux of *M*.

2.4.2.3 Interfacial Instability

During reaction, it is probable that small perturbations will form at the A-M_yO interface, Figure Figure 9. This perturbation will decrease the diffusion distances of O through A to the interface and increase the diffusion distance of M through M_yO. As a result, if the rate controlling process is the diffusion of M, oxide growth at the perturbation will be less than the rest of the scale, and the perturbation will shrink and disappear. Conversely, if the flux of O is controlling the growth rate, the diffusion distance to the top of the perturbation will be decreased, which will allow the oxide to grow faster at the top of the perturbation than the rest of the scale. When this is the case, the interface will become undulated, and eventually lead to the aggregate structure.

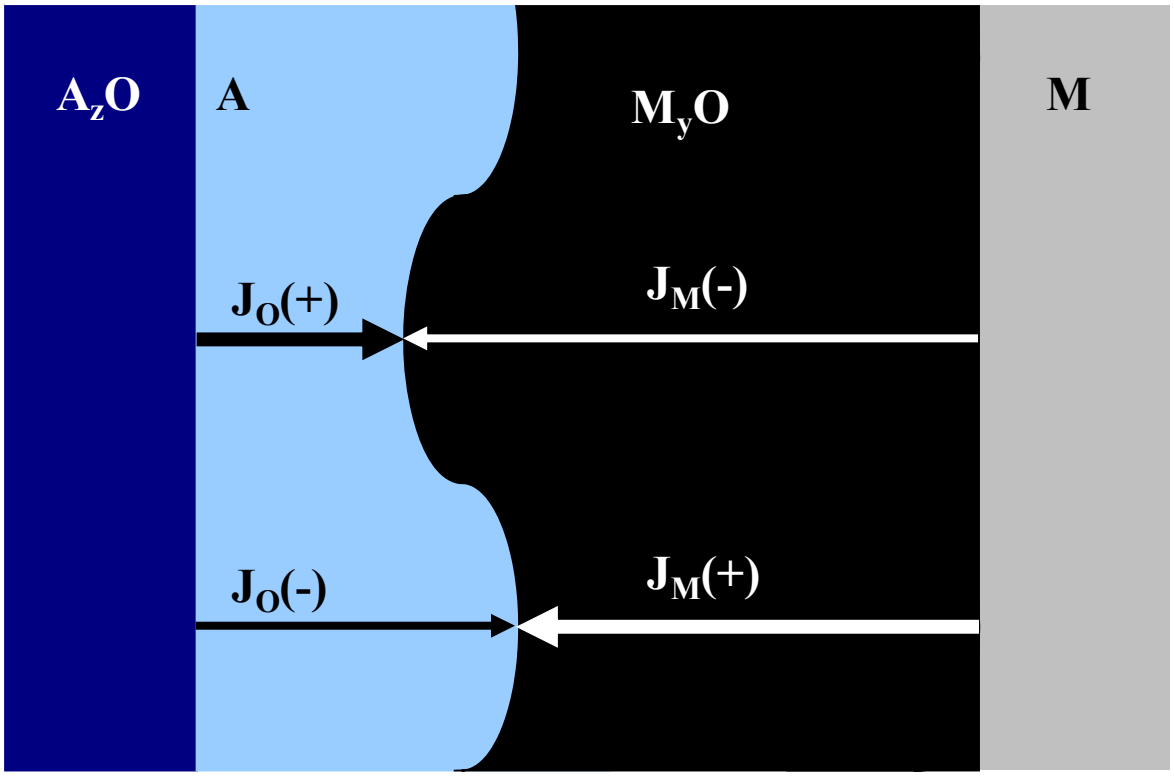

Figure 9. The variation in flux magnitude as a function of diffusion distance due to the formation of a perturbation.

In Rapp et al.'s work, the Ni-Cu_2O diffusion couple was studied. It was found that after annealing at 1000°C, a planar Ni/NiO/Cu/Cu_2O had developed, and the growth rate of NiO, was determined by the diffusion of Ni through NiO. In the same work, a Fe-Cu_2O diffusion couple was annealed at 1000°C. A similar layer sequence was developed, Fe/FeO/Cu/Cu_2O. However, because the rate of reaction was controlled by the flux of oxygen through copper, which was less than the flux of Fe through FeO, an aggregate structure developed in which FeO particles sit in a Cu matrix.

The above analysis is relatively simple when simple displacement reaction occurs. However, in many systems, ternary oxides exist, and it is possible for many reactions to take place. Notably, Li et al.[30] have studied the Ti-Al_2O_3 system in which multiple binary and ternary oxides along with intermetiallic compounds exist. After annealing a Ti-Al_2O_3 diffusion couple at 1100°C, the layer sequence Al_2O_3/TiAl/Ti_3Al/α-Ti/β-Ti forms. As demonstrated in Section 2.4.1.1, it is necessary to consider the fluxes of each species in a diffusion couple in a addition to the thermodynamics. Li et al[30] found that when a thin sheet of Ti was bonded with Al_2O_3 a different layer sequence developed. The thinner Ti layer allowed O and Al to accumulate to higher concentrations, which decreased the flux of each component into the layer, which changed the overall layer sequence to Al_2O_3/TiAl/α-Ti/ β-Ti.

2.4.2.4 Reaction Product Adherence

In the above analysis, it was assumed that reaction products remained adherent, and solid state diffusion controlled the overall reaction. However, this is not always the case. In the analysis of the reaction between two condensed phases, an important consideration is the volume change associated with the reactions. Consider a planar, solid substrate, A_zO in contact with the liquid metal M, which undergoes the displacement reaction in Equation 2.4.37. If the reaction product M_yO grows into A_zO, and the volume of the reaction products is greater than the volume of the reactants, the product will be put into a compressive stress. If the volume of the products is less than the reactants, the layer will be under a tensile stress.[3] The stress state is particularly important when ceramic phases are concerned. Most ceramics can withstand large compressive stress before buckling and spalling, but crack under relatively small tensile stresses.

A well established example of this issue occurs in the high temperature oxidation of metals, where a metal interacts with oxygen to form a metal oxide scale. Metals which react with oxygen to form an oxide with a smaller molar volume, e.g. Mg oxidizing to MgO, are found to oxidize very rapidly. As the oxidation reaction occurs, a thin layer of MgO grows, and the scale is put into tension due to the volume decrease. As the scale thickness increases, so does the strain energy in the scale, and the oxide cracks once the scale grows to a critical thickness. Conversely, when a Ni-Al alloy is selectively oxidized to form Al_2O_3, which has a larger molar volume, then the alloy, the oxide scale is put into compression. In many cases, an oxide scale is able to withstand several GPa of compressive stress without buckling and spalling.

Pilling and Bedworth[31] analyzed the effect that the ratio of the molar volume, subsequently known as the Pilling-Bedworth Ratio, *PBR*, of the oxide to the molar volume of the metal has on the oxidation behavior of several metals.

$$PBR = \frac{V_{Ox}}{V_M} \tag{2.4.38}$$

is defined as the ratio of the molar volume of the oxide to the metal. If the ratio is greater than unity, then the oxide is in compression and may be adherent, while if the ratio is less than unity, then the oxide is in tension, and cracking is observed. The *PBR* of several metal-oxide systems is presented in Table 1.

Table 1. The ratio of oxide to metal molar volume, the Pilling-Bedworth Ratio, PBR, for several metal oxides[3]

Oxide	PBR
K_2O	0.45
MgO	0.81
Na_2O	0.97
Al_2O_3	1.28
ZrO_2	1.56
Cu_2O	1.64
NiO	1.65
TiO_2	1.70

In liquid metal-oxide reaction, analyzing the change in volume due to reaction, and the resulting stress state is more complex because multiple layer sequences can develop and growth into a liquid phase does not generate stress. First, the initial layer sequence must be determined. First, consider a diffusion couple which forms the layer sequence $A_zO/A/M_yO/M$ and A is solid. The change in volume is then

$$V_{A_zO} \Rightarrow V_{M_yO} + V_M \tag{2.4.39}$$

Calculating the *PBR*

$$PRB = \frac{V_{M_yO} + V_M}{V_{A_zO}} \tag{2.4.40}$$

On the other hand, if the layer of *A* is a liquid, the volume expansion or contraction of M_yO should not create a stress in either, A_zO or M_yO.

If the $A_zO/M_yO/A/M$ layer sequence forms and *A* is solid, then the volume change of the reaction will again be the same as Equation 2.4.40, with the same *PBR* .

If the *A* phase remains liquid, then the change in volume of the reaction will only concern the oxide phases

$$V_{A_zO} \Rightarrow V_{M_yO} \tag{2.4.41}$$

and the change in volume will be

$$PRB = \frac{V_{M_yO}}{V_{A_zO}}$$

Zhou and DeHosson [32] have studied the wetting behavior of aluminum on silica, where it is found that the aluminum reduces silica to form alumina.

$$4Al + 3SiO_2 = 2Al_2O_3 + 3Si \tag{2.4.42}$$

which has the layer sequence SiO_2/Al_2O_3/Si-Al/Al. The volume change for the reaction is

$$PBR = \frac{2V_{Al_2O_3}}{3V_{SiO_2}} = 0.71 \tag{2.4.43}$$

The volume decrease suggests that the alumina layer will be in tension. Indeed, the reaction is observed to proceed rapidly, which is much faster than can occur as a result of solid-state diffusion through alumina. Although mechanistic study of the reaction rate has not been performed, it is speculated that the liquid metal flows through cracks in the alumina scale, and allows reaction to continue. The reaction rate can be either controlled by the kinetics of the surface reaction, or by liquid diffusion through cracks.

Alternatively, Nicholas et al. [33] have studied a number of binary and ternary liquid metals' wetting behavior on Al_2O_3. In many of the alloys, which have a high Ti activity, a TiO layer was observed to grow between the melt and the alumina substrate. After a 1 hour exposure at 1100°C a continuous 3-5μm layer of TiO was observed. The possible reaction is

$$Al_2O_3 + 3Ti = +3TiO + 2Al \tag{2.4.44}$$

which has a

$$PBR = \frac{3V_{TiO}}{V_{Al_2O_3}} = 1.02 \tag{2.4.45}$$

One area where the reaction rate of liquid metals with ceramics has been performed, is in the aluminum processing industry, where immersion tests in which refractory bricks are exposed to liquid aluminum.[34] However, these tests have involved multiphase ceramics, and a mechanistic understanding of the reaction processes has not been developed.

2.4.2.5 Wetting Behavior of reactive systems

The wetting behavior of metal-oxide systems which undergo a reaction depends on the nature of the reaction product. If the reaction product has partial metallic bonding character, as in the case of TiO, then adhesion between the metal and the TiO layer is strong, and low contact angles were observed. Conversely, when an alumina layer is formed, as in the Al-SiO_2 sessile drop, the wetting behavior is poor, as determined by the Al-Al_2O_3 bonding energies. In many other cases, it is hard characterize the meaning of a contact angle when thick multiphase reaction products are formed because the interfacial area cannot easily be determined and the metal-oxide interface is no longer in the plane of the oxide-vapor interface. However, it is frequently observed that good wetting is associated with reaction. In addition to the formation of metal-like compounds, there is generally a large amount of oxygen dissolution into the metal phase associated with the displacement reaction, and these clusters can promote adhesion, as described in Section 2.4.1.

2.5 NON-IDEAL SURFACES

In reality, solid surfaces are never truly, flat and homogenous, as assumed in Young's Equation. Deviation from ideality due to surface roughness, and chemical inhomogenity will now be considered

2.5.1 Rough Surfaces

Surface roughness can change the wetting phenomena in two ways. First, roughness will increase the area of contact between solid and liquid. If the true surface area is denoted A_R, and the surface area for a perfectly flat surface is A_I, then the change in free energy as a result of the increase of triple line length can be expressed as

$$G(z+\delta z)-G(z)=\Delta G=(\sigma_{SL}-\sigma_S)\frac{A_R}{A_I}\delta z+\cos\theta\sigma_L\delta z \tag{2.5.1}$$

The minimum energy configuration is

$$\cos\theta=\frac{A_R}{A_L}\left(\frac{\sigma_{SL}-\sigma_S}{\sigma_L}\right) \tag{2.5.2}$$

the Wenzel equation. [35]

A rough surface will increase the contact angle of a non-wetting liquid, and decrease the contact angle of a wetting liquid. Defining the quantity θ', as the contact angle of a liquid on a perfectly smooth surface, Figure 10 plots the change in θ, the measured contact angle, as a function of roughness for different values of θ'. In the Figure 10, each line represents a given

energetic relationship between a solid and a liquid. The graph shows how the contact angle will change as the surface roughness increases.

Rough surfaces can also pin the movement of the triple line which prevents the droplet from moving to its equilibrium configuration. Such a surface will keep a liquid that is advancing across a surface at an artificially high contact angle, and a liquid that is receding to an artificially low contact angle.

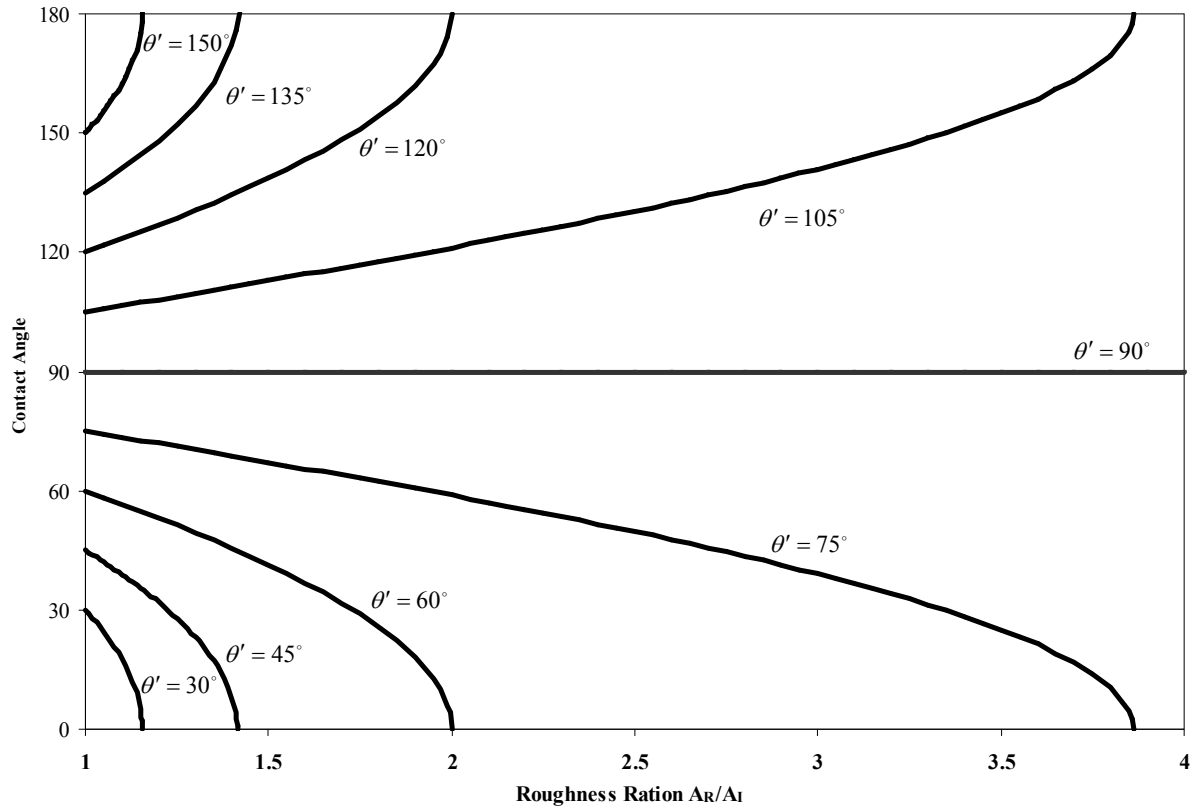

Figure 10. Equilibrium contact angle as a function of surface roughness

2.5.2 Heterogeneous Surfaces

The manner in which a liquid wets a flat, heterogeneous surface is a function of the phase distribution on the multi-phase surface, along with the global geometry of the solid-liquid ensemble. The problem of a liquid wetting a two-phase heterogeneous solid was first addressed by Cassie, in 1948.[36] Subsequently, many authors have analyzed under which circumstances Cassie's law is valid and have developed modified expressions. Additionally, it is possible for metastable configurations to develop depending on the solid microstructure. Often, the metastable configuration of a given system is dependent on whether the liquid is advancing or receding toward equilibrium.

A simple example, which can be used to illustrate the wetting behavior of liquids on heterogeneous solids, is the capillary rise of a liquid up a hollow cylinder composed of two phases α, and β. It is further assumed that the distribution of β in an α matrix is uniform and that the average radius of each phase is small with respect to the capillary length l_C . The capillary length is the distance a perfectly wetting liquid can climb a wall against gravity.[7]

$$l_C = \sqrt{\frac{2\sigma_L}{\rho g}} \tag{2.5.3}$$

The total energy of the liquid, raised a height *h* up a capillary tube of radius *r* is

$$E = f^{\alpha}\left(\sigma_{SL}^{\alpha} - \sigma_{S}^{\alpha}\right)2\pi rh + f^{\beta}\left(\sigma_{SL}^{\beta} - \sigma_{S}^{\beta}\right)2\pi rh - \rho g\pi r^2 h\left(\frac{h}{2}\right) \tag{2.5.4}$$

where f^{α}, and f^{β} are the surface area fractions of the α and β phases. Setting $\frac{dE}{dz} = 0$, the capillary rise will be

$$h = \frac{2\pi\left(f^{\alpha}\left(\sigma_{SL}^{\alpha} - \sigma_{S}^{\alpha}\right) + f^{\beta}\left(\sigma_{SL}^{\beta} - \sigma_{S}^{\beta}\right)\right)}{\rho g r} \tag{2.5.5}$$

Substituting Equation 2.5.5 and Equation 2.2.14, into Equation 2.2.9, an expression can be produced that describes the measured contact angle of a liquid on an α-β surface.

$$\cos\theta^{M} = f^{\alpha}\cos\theta^{\alpha} + \left(1 - f^{\alpha}\right)\cos\theta^{\beta} \tag{2.5.6}$$

This relationship is known as Cassie's law. [36]

Cassie's law was derived by applying the minimum energy change criterion $\frac{dE}{dz} = 0$ to determine the equilibrium configuration. In the above derivation, it was assumed the spatial distribution of α and β phases were uniform in the direction parallel to *h*. However, if the distribution of phases is not homogenous, the change in energy that results from the movement of the triple line toward a given location will not necessarily be identical to the energy change that results from the movement of the tripleline in the opposite direction. Under these circumstances, a receding liquid can form a different contact angle than an advancing liquid. This phenomenon is know as contact angle hysteresis, and in certain systems, the advancing and receding contact angles can be quite different.

The concept of contact angle hysteresis and metastable configurations can be illustrated, following the example of Eustatholopous et al,[7] by considering the vertical wall of a crucible consisting of two macroscopic phases α and β in which $\theta^{\alpha}>90°$ and $\theta^{\beta}<90°$ and the α-β interface is perpendicular to the wall, Figure 11.

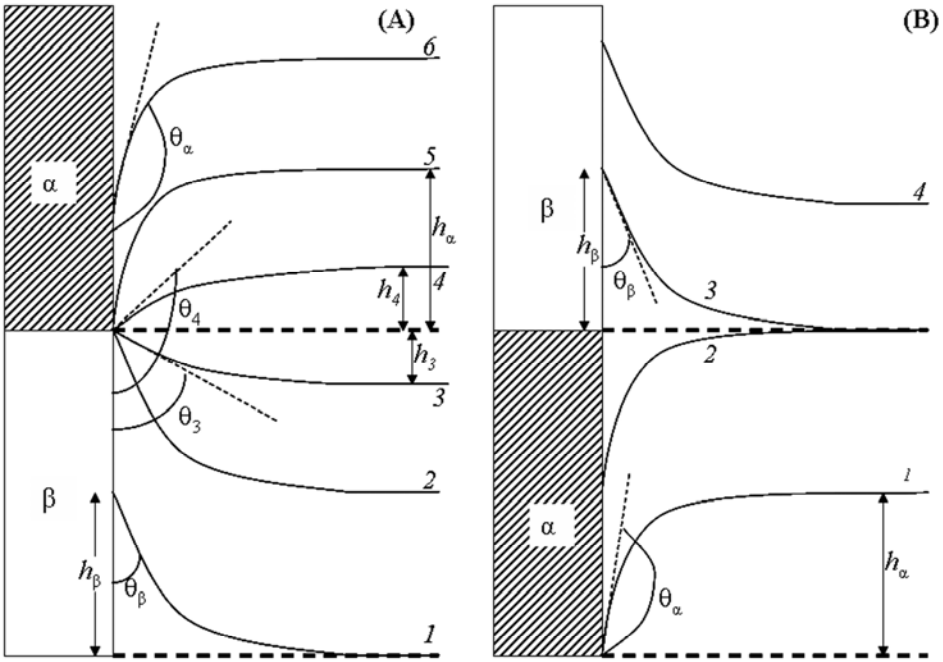

Figure 11. A schematic representation of the profile of a liquid surface against a two-phase crucible wall. (A). The height of a liquid is increased from a starting amount in configuration 1, to a final amount in configuration 6 in 5 steps. (B) The liquid is initially in configuration 1 and liquid is raised to configuration 4.

First, consider the liquid to be at height $h°$ and separated from the wall. If the liquid is then allowed to contact the wall, it will climb the wall a distance h_β forming the contact angle θ_β such that Young's equation is satisfied at the liquid-β-vapor triple line. This is shown in configuration 1 in Figure 11(A). If liquid is then added to the crucible, the global level of the liquid will be raised as will the location of the triple line. By further raising the liquid, the triple line, at contact angle θ_β, will continue to advance up the wall until it reaches the α-β interface, configuration 2 in Figure 11(A). Once the triple line reaches the α-β interface, the liquid will be pinned because the liquid does not wet the α phase. Further increases to the liquid height will cause the contact angle to increase, configuration 3, Figure 11(A). In this configuration, Young's equation is no longer satisfied at the triple line. By further increasing the liquid height, the liquid will become parallel with the α-β interface, having a 90° contact angle.

If more liquid is added so that the liquid level is above the α-β interface, a capillary depression will occur, configuration 4, Figure 11(A). This contact angle will be less than θ^α until enough liquid is added to raise the global height of the liquid a distance h_α above the α-β interface, where h_α is the equilibrium capillary depression distance of the liquid on α. When the height of the liquid is between configurations 2 and 4, in Figure 11(A), the system is at a local energy minimum, but the system is metastable with respect to the minimum surface energy configuration. The variation in contact angle as a function of the location of global height of the liquid is given in Figure 12.

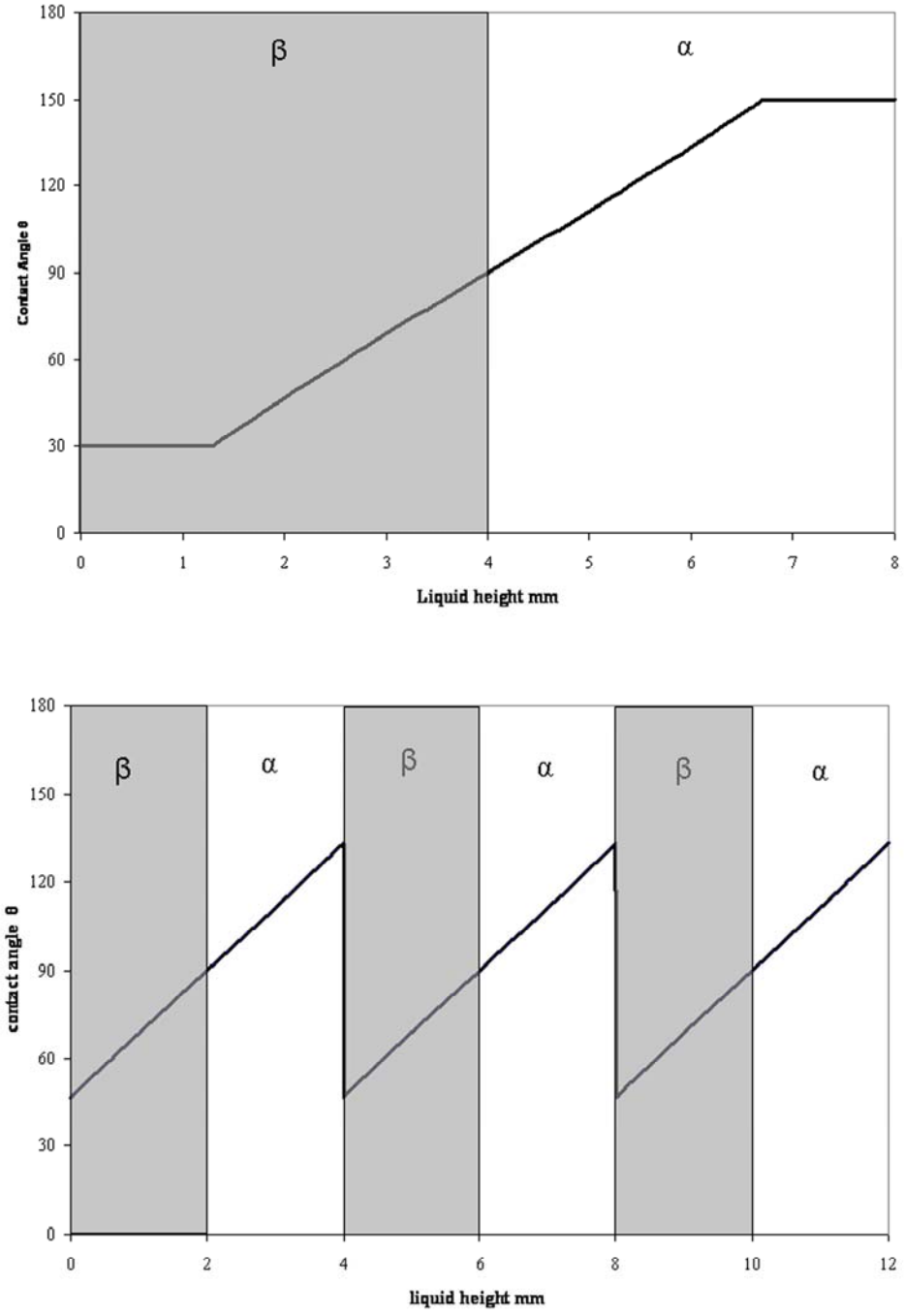

Figure 12. Contact angle as a function of liquid height for a liquid in (A) a bi-strip crucible and (B) a multi-strip crucible.

Alternatively, if the non-wetting α phase is below the β phase, Figure 12(B), a depression of the liquid will occur. As the liquid level is raised, the same contact angle, θ_α and depression distance h_α will occur, until the global liquid level is above the α-β interface. When the liquid level is raised above the α-β interface, the liquid will climb the wall a distance h_β forming the equilibrium contact angle, θ_β, with the β phase.

Now consider a crucible wall composed of multiple alternating strips of α and β, such that the thickness of the strips are greater than h_α and h_β. The contact angle can be determined as a function of the global height of the liquid, Figure 12. In this configuration, the liquid height-contact angle relationship is not a function of the direction the liquid is moving. If the thickness of the strips gets thinner, the form of the variation of contact angle will remain the same as in Figure 12, but the equilibrium contact angle will not be reached, and the range of cycle of contact angles will be smaller and as the strips get infinitely small, a constant 90° contact angle will be achieved.

Johnson and Dettre[37] have studied the wetting of a heterogeneous solid in the standard sessile drop configuration in which they considered the wetting of a droplet on a solid composed of rings of alternating wetting and non-wetting phases. In the sessile drop configuration, the liquid is still subject to being pinned in metastable configurations. These authors expanded their analysis to consider the vibrational energy of a liquid, and examined the energy barrier a liquid must overcome to move from a pinned configuration into a lower energy configuration. Using this method, they were able to predict the contact angle hysteresis of advancing and receding liquids which is observed in many systems.[38]

In many circumstances, the heterogeneous surfaces are not composed of a homogeneous distribution of two phases. As shown above, liquids in these systems can be pinned in metastable configurations. An advancing liquid, by definition, is initially at a contact angle higher than equilibrium and moving toward a lower energy configuration. If the liquid moving along a heterogeneous surface is subject to pinning, it is possible that the liquid will not be able to reach its lowest energy configuration. Therefore advancing liquids tend to have higher than equilibrium contact angles. Likewise, receding liquid will tend to have lower than equilibrium contact angles, as they start at contact angles lower than equilibrium and may be subject to pinning, resulting in a contact angle lower than equilibrium.

Horsthemke and Schroder[39] have shown that the contact angle of an advancing or receding liquid can be determined without considering the influence of vibrational energy. They calculated the maximum area fraction that a line passing through a two-phase mixture by considering an array of hexagons which are randomly assigned to be either α or β. From this arrangement, values of the local minimum, f_{min} and maximum f_{max} area fractions a line could pass through was determined using a statistical method. With knowledge of the maximum and minimum area fractions, the expressions

$$\cos\theta^{A} = f^{\alpha}_{\max}\cos\theta^{\alpha} + \left(1 - f^{\alpha}_{\max}\right)\cos\theta^{\beta}$$
$$\cos\theta^{R} = f^{\alpha}_{\min}\cos\theta^{\alpha} + \left(1 - f^{\alpha}_{\min}\right)\cos\theta^{\beta}$$

were developed. Figure 13 shows the variation in contact angle for an advancing and receding liquid as a function of the overall area fraction α and β when θ^{α}=90° and θ^{β}=0°.

Naidich et al have studied the wetting of Sn, Sn-Ti, and Cu-Sn alloys on macroscopically patterned Mo-SiO_2/MgO/Al_2O_3 glass systems.[40] The contact angle hysteresis measured in that study agreed with the work of Horsthemke and Schroder. However, the liquid droplet shape on certain macroscopically patterned surfaces was non-circular, demonstrating the ability of a heterogeneous surface to pin a liquid.

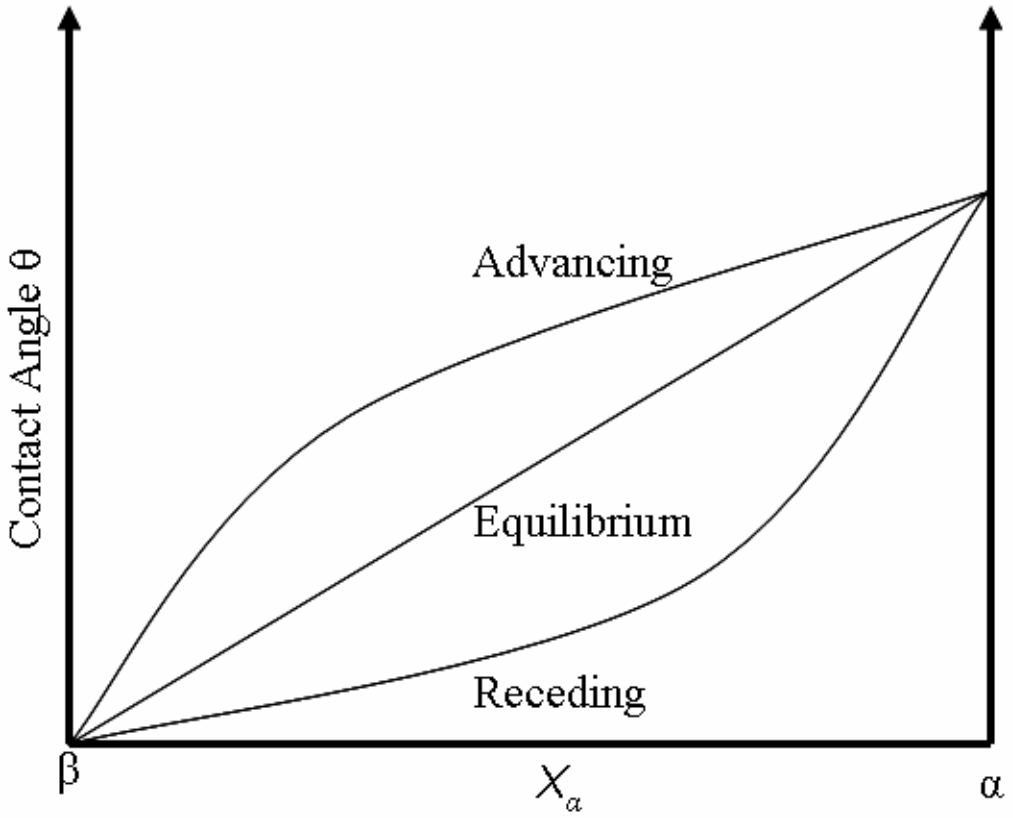

Figure 13. The contact angle of an advancing, equilibrium and receding liquid on a two phase solid consisting of α and β where θ_α=90° and θ_β=0°.

2.6 WETTING BEHAVIOR OF LIQUID COPPER ON METAL OXIDES

Gallois and Lupis[41] have determined the surface free energy of liquid copper at very low values of pO_2 and then determined the effect that the pO_2 has on the surface energy. The surface free energy of copper remained relatively constant over a range of low values of pO_2, and then decreased with increasing pO_2. At a given pO_2, the relative adsorption isotherm becomes constant and this saturation is believed to occur as a result of the formation of the 2D compound Cu_3O. Table 2 lists several physical properties of copper.

Table 2 Physical properties of Cu and Cu-O [7, 41]

Property		unit
T_M	1083.4	°C
Density	7.92	g/cm^3
Surface Free Energy at T_M in vacuum	1.32	J/m^2
Oxygen Saturation Adsorption	5.72×10^{-6}	mol/m^2
Area of Adsorbed Oxygen	2.9	nm
Dissocation of Cu_2O at T_M	3.9×10^{-6}	atm

The sessile drop technique has been used to determine the contact angle of Cu on ZrO_2 yielding θ=122° at 1200°C.[42] Similarly, Ghetta et al.[43] have determined the contact angle of Cu on Al_2O_3 using the sessile drop technique and found θ=130°. These authors have also studied the dependence of contact angle on pO_2 finding that the contact angle remains constant at low oxygen partial pressures and then abruptly drops approximately 10° when the oxygen partial pressure is greater than $pO_2=10^{-11}$ atm, and then remains constant if the pO_2 is further increased. Young's equation indicates that the contact angle of a non-wetting liquid will increase as the liquid surface energy decreases. Therefore, if it is assumed that the alumina surface energy remains constant, then the solid-liquid interfacial energy must decrease faster than the liquid surface energy. Yi et al.[44] has found that $CuAlO_2$ can form at Cu-Al_2O_3 interfaces if the effective pO_2 at the interface is sufficiently high. It is believed that the formation of $CuAlO_2$ decreases the solid-liquid interfacial energy which causes the contact angle to drop. The only study of the wetting properties of Cu on NiO was performed by Naidich[45] who found the contact angle to be 68°.

2.7 LIQUID ALUMINUM-ENVIRONMENT INTERACTIONS

2.7.1 The Oxidation of Liquid Aluminum

2.7.1.1 Thermodynamics

Corundum, α-Al_2O_3, is the thermodynamically stable oxide of aluminum, and has rhombohedral crystal structure. However, at temperatures below 1000°C, aluminum has been found to oxidize to several metastable oxides. At low temperatures an amphorous oxide phase is found and at higher temperatures, γ-Al_2O_3, a cubic spinel, and θ-Al_2O_3, which is monoclinic are observed.[3]

Several Al_xO_y vapor species are known to exist, which can be formed by the decomposition of Al_2O_3.

$$Al_2O_3 = Al_2O_{(g)} + O_{2(g)} \quad (2.7.1)$$

$$Al_2O_3 = 2AlO_{(g)} + \tfrac{1}{2}O_{2(g)} \quad (2.7.2)$$

$$Al_2O_3 = 2Al_{(g)} + \tfrac{3}{2}O_{2(g)} \quad (2.7.3)$$

$$Al_2O_3 = Al_2O_{2(g)} + \tfrac{1}{2}O_{2(g)} \quad (2.7.4)$$

A vapor species diagram is presented in Figure 14. Al-O vapor species diagram at 700°C in which the partial pressure of each vapor species is plotted as a function of oxygen partial pressure. At oxygen partial pressures in the range of the Al_2O_3 dissociation pressure, the partial pressures of Al_2O and Al, becomes the greatest.

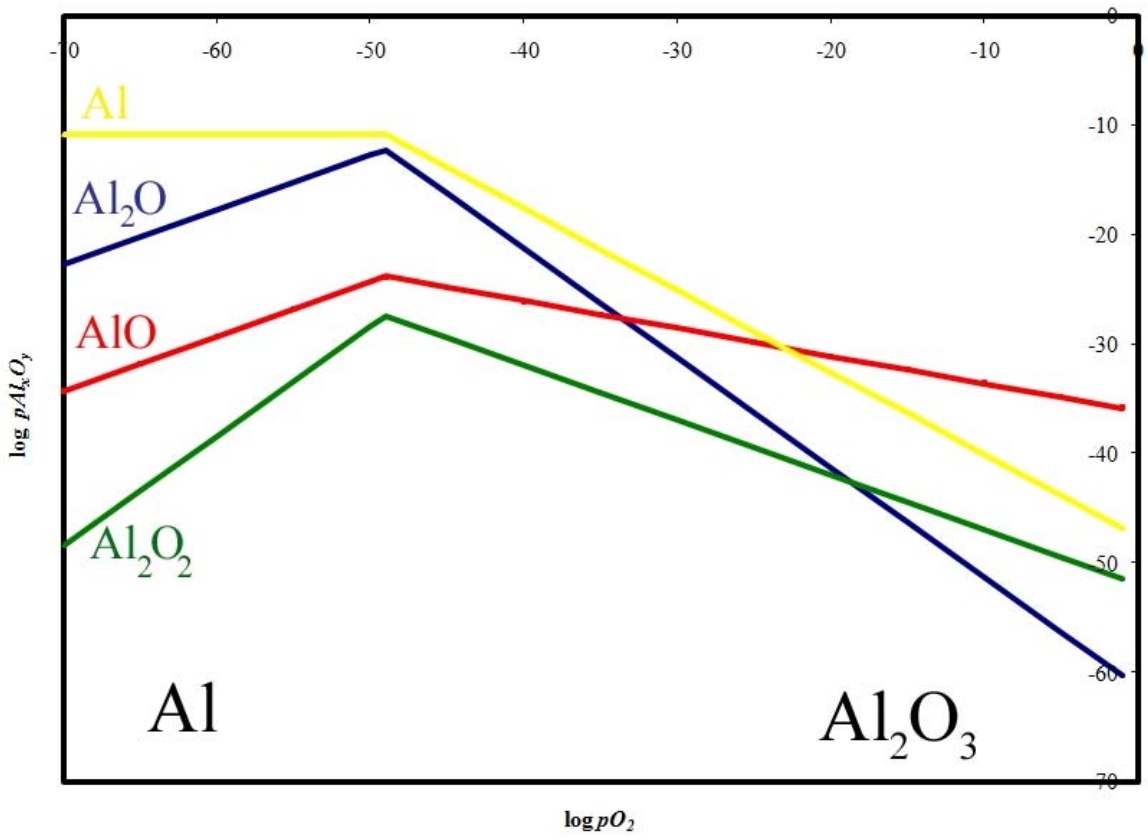

Figure 14. Al-O vapor species diagram at 700°C

Numerous investigators have studied the wetting behavior of aluminum on alumina. In order for a liquid metal sessile drop measurement to move to an equilibrium contact angle, it is necessary that an oxide scale is not formed on the surface of the liquid metal. Therefore, for a system of the type, A-A_zO, if the oxygen partial pressure in the atmosphere is not at the A/A_zO dissociation pressure, there will be a tendency for either A to be oxidized, or A_zO to be reduced.

It has been suggested that under high vacuum conditions, a dynamic equilibrium can be established in the Al-Al_2O_3 system, in which the aluminum surface can remain metallic when the bulk composition of the gas has a pO_2 greater than Al_2O_3 dissociation pressure. The deoxidation mechanism of Al_2O_3 will now be considered.

Consider a droplet of liquid aluminum, which is initially covered by an oxide film of γ-Al_2O_3 100 nm thick, and exposed to a pO_2=10^{-10} atm. Under these conditions, the thickness of the oxide will increase and the growth will be controlled by the outward diffusion of Al through the oxide.[3] In addition to oxide growth, the oxide will produce vapor species as shown in Figure 14. Al-O vapor species diagram at 700°C. The oxide scale will continue to grow as long as the flux of aluminum through the scale is greater than the flux of Al, in Al_xO_y vapor species, away from the oxide surface.

If the bulk pO_2 in the atmosphere is decreased to the point where the rate of oxygen consumption is greater than the rate at which oxygen can flow to the oxide-gas interface, an oxygen concentration gradient will develop in the gas phase. Once the oxygen concentration

gradient is developed, the process will have a tendency to avalanche. As shown in Figure 14. Al-O vapor species diagram at 700°C, the pAl_2O and pAl increase with decreasing pO_2. The increased concentration of $Al_2O_{(g)}$ consumes more oxygen and causes the pO_2 to be further depressed at the gas-oxide interface.

As the thickness of the oxide film approaches 5 nm,[46] the oxide will be thin enough for electron tunneling to proceed through the oxide, which will allow the oxidation process to continue without solid state diffusion. Under these conditions, the activity of Al in the oxide will increase, and become constant through the thickness of the oxide.[46] The metal consumption rate will then become much more rapid than when diffusion is rate controlling. Eventually, the local pO_2 can drop below the Al_2O_3 dissociation pressure and a metallic Al surface can be developed.

2.7.1.2 Kinetics

Even in air, the oxidation rate of aluminum to α-Al_2O_3 is extremely slow. The slow growth of α-Al_2O_3 is due to the low defect density in the oxide, which makes solid state diffusion sluggish. The growth kinetics of γ-Al_2O_3 and θ-Al_2O_3 are significantly more rapid than α-Al_2O_3, but still relatively slow.

Freti et al.[47] have determined the oxidation rate of liquid aluminum at temperatures between 700 and 800°C. It was found that γ-Al_2O_3 was grown, and after a 2 hour exposure at 700°C, a 100 nm thick scale had formed. After 5 hours of growth, γ-Al_2O_3 transformed to α-Al_2O_3. The γ-α phase transition results in a decrease in molar volume, and cracking occurs upon transformation.

2.7.2 Aluminum-Ceramic Chemical Interactions

2.7.2.1 The Al-Si-O system

When equilibrium is reached, the Al-Si-O ternary system is relatively simple, with no intermetallic phases, two binary metal oxides, corundrum, Al_2O_3 and cristobolite SiO_2, (the tridymite polymorph is not stable at the temperature considered in this investigation) and a single ternary oxide, mullite, $Al_6Si_2O_{13}$. However, both Al_2O_3 and SiO_2 exhibit multiple metastable polymorphs.

The Al-Si binary phase diagram is presented in Figure 15, and isothermal section of the Al-Si-O ternary phase diagram are presented in Figure 16.

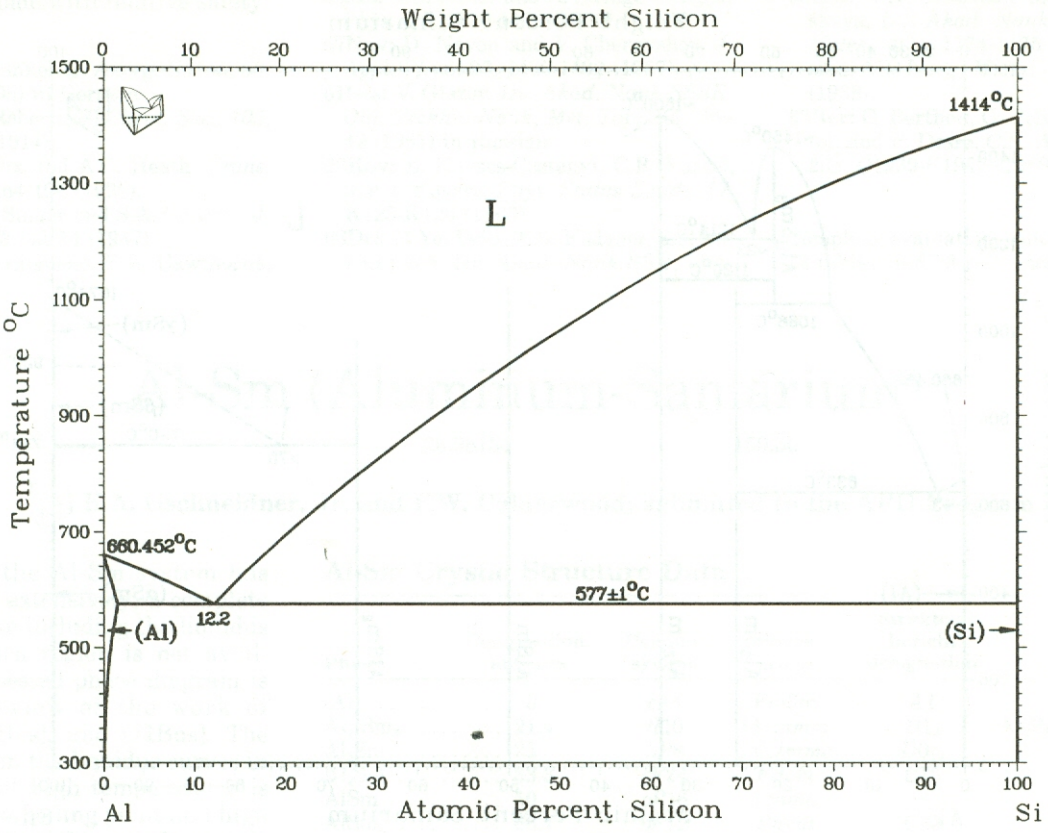

Figure 15 Al-Si binary phase diagram [48]

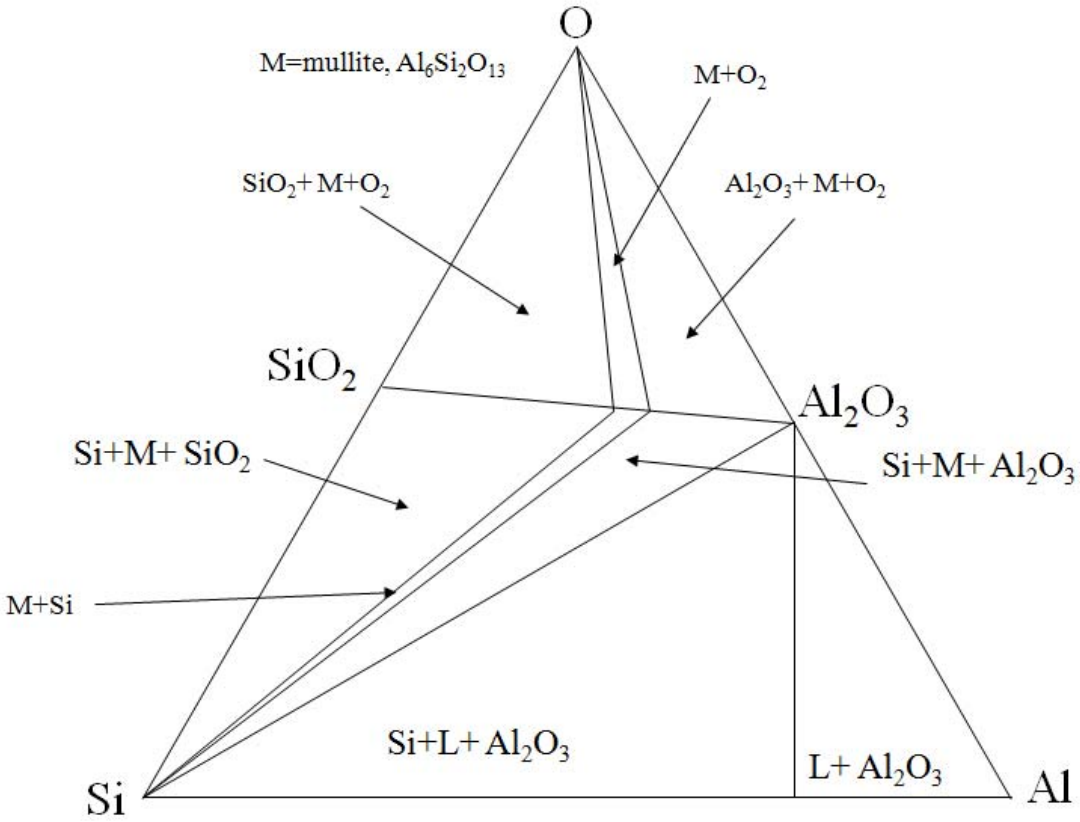

Figure 16. Isothermal section of Al-Si-O ternary phase diagram at 700°C

Schematic models of the metal mole fraction versus oxygen potential are presented in Figure 17. The exact details of these diagrams are unknown.

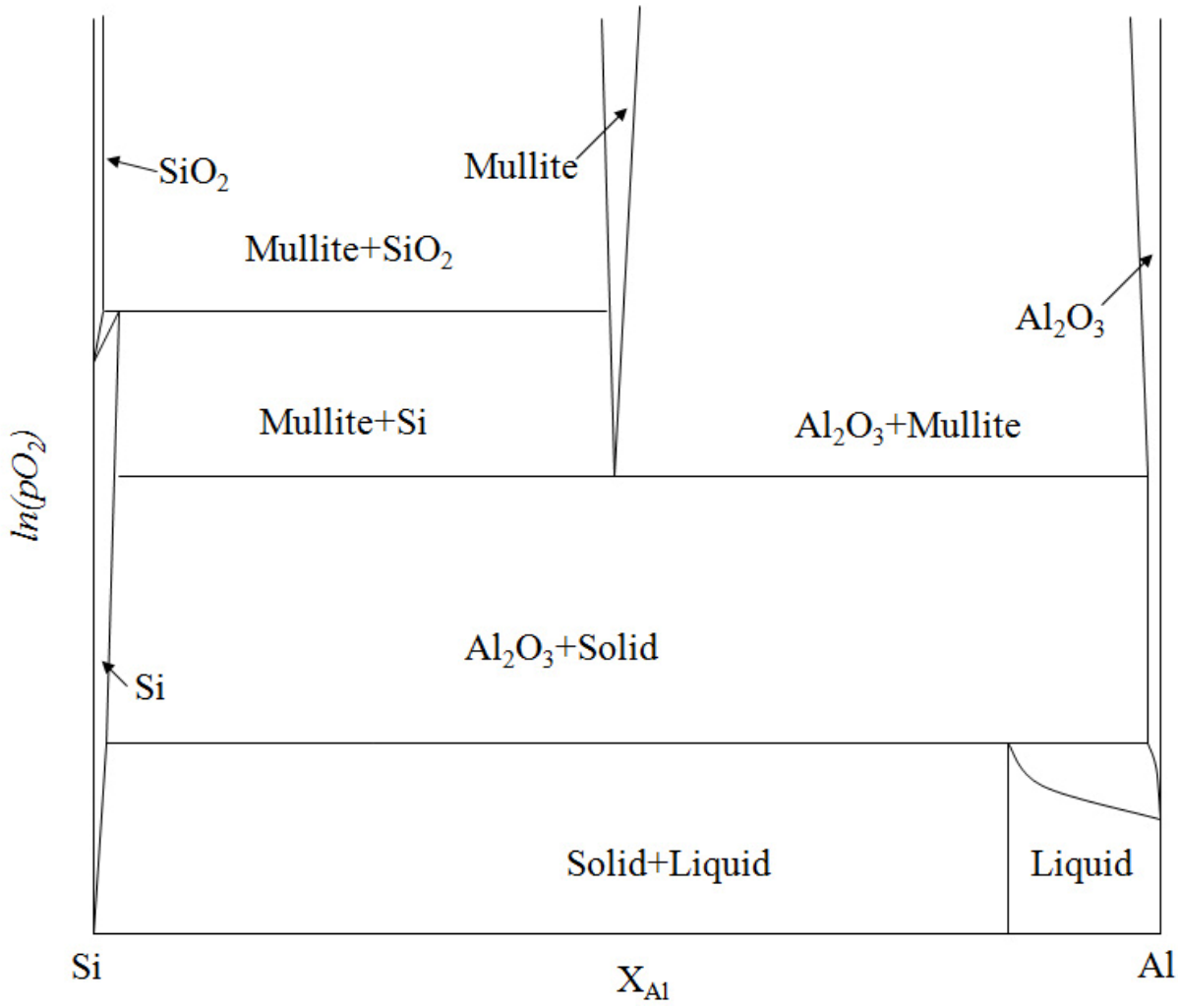

Figure 17. Schematic of oxygen partial pressure-composition Al-Si-O phase diagram

2.7.2.2 Al-Zirconia

Several Al-Zr intermetallic compounds exist, as shown in the binary phase diagram, in Figure 18, but no ternary oxides exist in the Zr-Al-O system. The standard free energy change for the reaction

$$3ZrO_2 + 4Al = 2Al_2O_3 + 3Zr \qquad (2.7.5)$$

becomes positive around the melting point of Al, and in the temperature range 700-1000°C, $\Delta G°$=5-35kJ/mol. If the reduced zirconia can react with Al to form the intermetallic compound Zr_3Al, the standard free energy change for the reaction, should be negative.

$$3ZrO_2 + 5Al = 2Al_2O_3 + Zr_3Al \qquad (2.7.6)$$

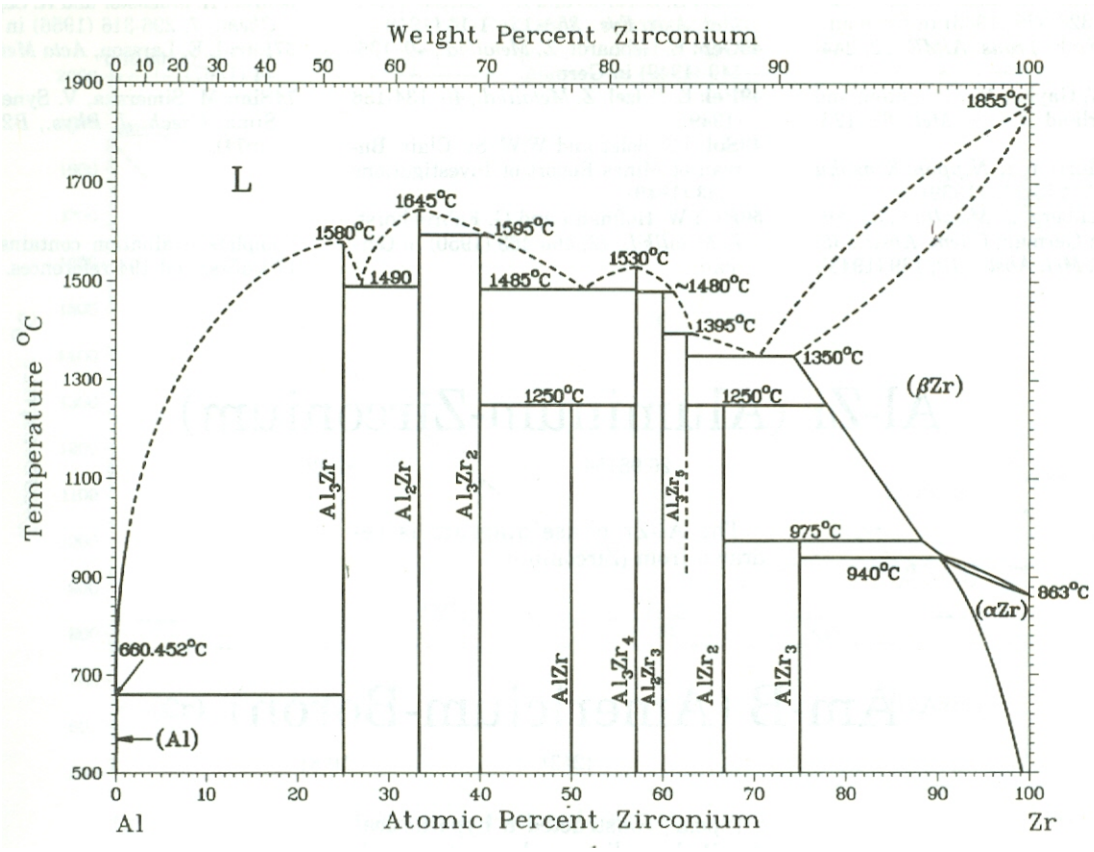

Figure 18. Al-Zr binary phase diagram [48]

2.7.2.3 Al-Metallophobic Ceramic Interactions

Barite, $BaSO_4$, has the tendency to be reduced by Al, according to the reaction

$$BaSO_4 + \tfrac{8}{3} Al = \tfrac{1}{3} Al_2S_3 + BaO + Al_2O_3 \qquad (2.7.7)$$

Fluorite, CaF_2, is not susceptible to reduction by Al, as the reaction, Equation 2.7.8, has a large postive standard free energy change. The corresponding $pAlF_3$ is less than 10^{-20} atm in the temperature range 700-1000°C.

$$3CaF_2 + 2Al = 2AlF_{3(g)} + 3Ca \qquad (2.7.8)$$

2.7.3 Wetting Behavior of Liquid Aluminum on Ceramics

Experimentally, the wetting behavior of liquid aluminum on ceramic substrates has been difficult to measure due to the extremely low dissociation pressure of Al_2O_3.[7] Unless performed in a very low pO_2 atmosphere, an oxide film will form on the surface of the liquid aluminum, preventing a true aluminum surface energy from determining the equilibrium contact angle. Under these circumstances, the contact angle of aluminum on most ceramics is large, and can be as high as 160°.

When investigated in a sufficiently low pO_2 environment, the contact angle of Al on Al_2O_3 has been found to be a function of temperature. Laurent et al.[49] have calculated the Al/Al_2O_3 contact angle's temperature dependence in the range 663-1000°C, in high vacuum, finding

$$\theta^\circ = 103 - 0.05\left(T - T_m\right)$$

The temperature coefficient of aluminum, $d\theta/dT$, is similar to that of other metals on alumina, denoting the lack of influence of an oxide scale on the contact angle. However, the Al/Al_2O_3 contact angles had a greater variation, ±8°, than less reactive metals on alumina, ±3°. These authors[49] have attributed the variation to the presence of discontinuous oxides on the liquid metal surface. If the pO_2 in the environment in which the sessile drop measurement is performed is sufficiently low, the Al_2O_3 scale was found to evaporate from the liquid metal, as described in Section 2.7.1 Under these conditions, the contact angle will initially be greater than the equilibrium angle, and then decrease with time as the amount of oxide on the aluminum surface is decreased due to Al_2O evaporation.

The contact angle of *Al* on ZrO_2 is 60° at 1100°C [50]. This contact angle is surprisingly low considering the small amount of ZrO_2 that dissolves into *Al*. The strong adhesion, and low contact angle, may be associated with the high electrical conductivity that ZrO_2 exhibits in low pO_2 environments. Liquid metals generally form low contact angles on highly conductive ceramics due to electronic bonding at the interface which decreases the solid-liquid interfacial energy.[7]

2.8 REFRACTORY MATERIALS

The degradation of refractory ceramics decreases the efficiency with which aluminum can be processed in re-heating and holding operations, used in production of cast aluminum products. Refractory degradation decreases the production efficiency in three ways. First, because the refractories which hold liquid aluminum serve as insulators, reduction in refractory thickness allows the heat flux out of the liquid metal to increase, which increases the power necessary to hold the metal in the liquid state. Secondly, the faster the refractory is degraded, the more frequently the operation must be shut down to allow the refractory to be replaced. The shut down of operation drastically decreases the overall efficiency because slow cooling and heating procedures must be used which causes the shut down time to be lengthy. Thirdly, the manner in which liquid metal is heated is determined by the stability of the refractory. In most commercial plants, heat is supplied by burning methane above the liquid metal bath. This process is an inefficient method of heat transfer, relying primary on radiation and convection, and causes significant metal loss. If the rate of degradation is understood, and sufficiently slow, functional refractory walls, which hold heating elements, and direct immersion heaters can be used which heat the molten aluminum by conduction which is significantly more efficient.

Refractory ceramics used in the aluminum processing industry are typically made of three components: the matrix, cement, and metallophobic additions.[5] The primary matrix component in most refractories is alumina, due to its chemical stability, and low cost. Many refractories, known as 'high-alumina refractories' are over 90% Al_2O_3. The second most

common component is silicon, which is usually present as mullite, $Al_6Si_2O_{13}$, magnesite $MgSiO_4$ or as silica, SiO_2. The silica phases generally have inferior chemical resistance, with respect to alumina, but are more thermal shock resistant, better insulators, and less expensive. Stabilized zirconias are also used but are more expensive, and susceptible to liquid metal infiltration.

Most refractories use a cement phase, typically, composed of calcium-aluminate, to bind the matrix particles together. The use of cement is necessary in castable refractories.[5]

In addition to the matrix phases above, small additions of metallophobic agents are also present in most refractories. The most common additives are CaF_2, BN, and $BaSO_4$. Typically refractories are composed of 1-10% of these compounds.

The reduction of silica by aluminum is one of the primary degradation mechanisms by which refractory ceramics are degraded. However, a mechanistic understanding of the rate of degradation, and the mechanism which controls this rate is far from complete. The general analysis of refractory degradation is complicated by the complex nature of the refractory due to the heterogeneous structures, but it is useful to investigate the degradation mechanism of each component, in order to build a fundamental background necessary to understand the degradation of the composite material.

A second degradation mechanism is through liquid metal infiltration into cracks and pores. The addition of metallophobic agents, $BaSO_4$, BN, and CaF_2 decreases the tendency for metal infiltration. The mechanisms by which the metallophobic agents improve the resistance of

refractory ceramics to liquid infiltration are not well understood. Aluminum will react with barite and boron nitride to form Al_2O_3 and AlN, respectively. It is possible that these or other reaction products form at a slower rate than the dissolution of alumina or silica, or that they can adhere better to the matrix, but more work is warranted in this area. Aluminum does not react with fluorite, and fluorite is one of the few compounds that liquid aluminum does not wet.[51] This compound may increase the contact angle of Al on Al-Si-O/CaF_2 ceramics as described in Section 2.7.2.3. The addition of CaF_2 may increase the contact angle of Al on the refractory ceramic in a manner predicted by Cassie's Law. However, it is unclear if the small concentration of CaF_2 which is present could increase the contact angle enough to prevent infiltration.

3.0 PROBLEM STATEMENT

The degradation of refractory ceramics by molten metals decreases the operational efficiency of many aluminum processing operations. The goal of this investigation is to develop a fundamental understanding of the mechanisms by which refractory ceramics are degraded by liquid aluminum.

4.0 EXPERIMENTAL PROCEDURE

4.1 SESSILE DROP

The sessile drop technique was used to measure the contact angle of liquid metals on ceramic substrates. The experimental apparatus consists of a resistance heated tube furnace with a mullite reaction chamber, Figure 19. On one end of the reaction chamber, a flat, Pyrex window is sealed to the mullite tube, enabling viewing into the chamber. On the other end is a standard taper glass joint, with a removable end cap, with two O-ring joints. One of the joints is connected to a mechanical vacuum pump which allows the system to be evacuated to a pressure of 10^{-4} atm. The other joint is used as a gas inlet.

Different techniques were used to control the gas atmosphere. When the lowest oxygen partial pressure was desired, an Ar-4%H_2 gas mixture was flowed directly into the chamber. When higher oxygen partials pressures were desired, Ar-H_2 mixtures were bubbled through a water bath, and the oxygen partial pressure was fixed by controlling the initial gas composition and the water bath temperature. Table 3 shows the oxygen partial pressures in equilibrium with different gas compositions and water bath temperatures. In order to obtain specific oxygen partial pressures without the presence of hydrogen, argon gas was passed through a furnace

containing metal turnings. The choice of metal along with the furnace temperature was used to fix the oxygen partial pressure in the gas.

Table 3. Equilibrium gas compositions for O_2-H_2-H_2O at 1100°C

Gas Mixture	Gas Pressure atm		
	pO_2	pH_2	pH_2O
Ar-4%H_2	2.14×10^{-24}	0.04	2.00×10^{-7}
Ar-0.06%H_2O	2.03×10^{-11}	4.05×10^{-7}	6.24×10^{-4}
Ar-0.06%H_2O Cu/Cu_2O-1000ºC	5.65×10^{-7}	6.71×10^{-11}	0.06

The ceramic substrates used in the sessile drop experiments were roughly ground, and then finely polished using 9 and 3 μm diamond pastes and then with 0.04 μm colloidal silica. The metal specimens were cut to the desired size, and polished with a 600 grit diamond polishing wheel to create fresh surface. The ceramic and metal specimens were then ultrasonically cleaned in acetone and isopropanol.

Following cleaning, the specimen was placed on the ceramic substrate and loaded into the reaction chamber. The chamber was then evacuated and backfilled with the desired gas mixture. This process was repeated three times. The temperature was then elevated to the desired test temperature, and a Canon Rebel XT camera with a Quantaray 70-300mm lens, was used to photograph the liquid metal droplet shape on the ceramic substrate.

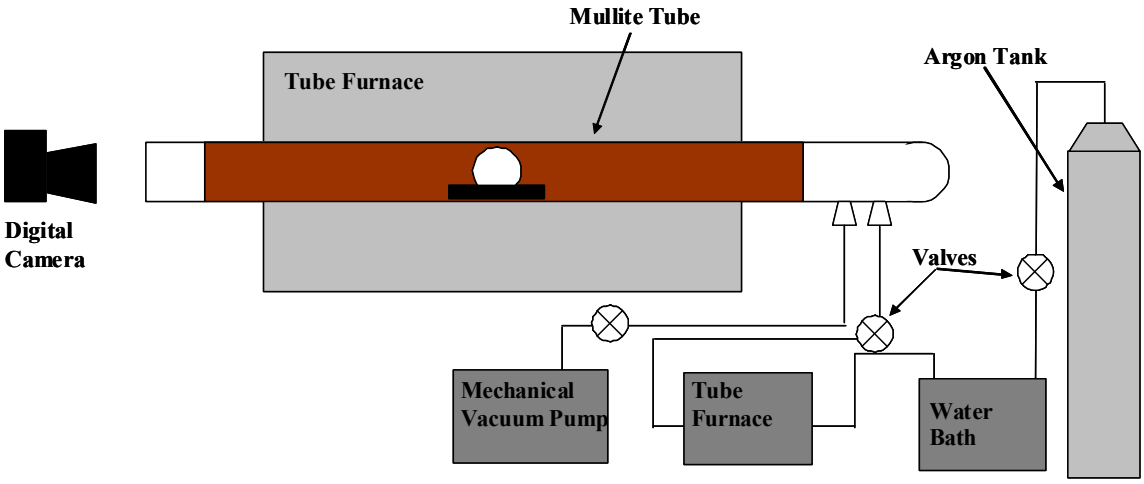

Figure 19. Schematic of sessile drop apparatus

4.2 DYNAMIC CAPILLARY DISPLACEMENT (DCD)

An alternative method has been developed to determine the contact angle which is based on the classic capillary rise experiment. The contact angle is determined by measuring the distance a liquid is raised or depressed above the external liquid surface, Figure 2. The energetics of the liquid displacement were described in Section 2.2.

The apparatus consists of a 50 kg bath of aluminum which is heated in a resistance crucible furnace. A screw driven vertical traverse is attached to a uni-strut truss which extends over the liquid metal, Figure 20. A digital caliper is attached to the truss and to the traverse which allows measurement of the vertical travel of the traverse. A ceramic tube, with an inner diameter between 1-4 mm is attached to the traverse and is incrementally lowered into the metal bath. A graphite electrode sits in the liquid metal bath, and a wire is lowered into the tube during testing. When the wire contacts the metal inside the tube, a circuit is completed. From the length of the wire, the length of the tube and depth of the tube below the metal surface, the distance the metal is displaced in the tube can be determined.

During testing, the surface of the aluminum metal reacts with the air to form an oxide film, whose thickness grows to angstroms in the first seconds of exposure and to hundreds of nanometers after several hours of exposure. The oxide film inhibits the flow of the liquid metal into the tube. To break the oxide film vibratory energy is applied to the tube.

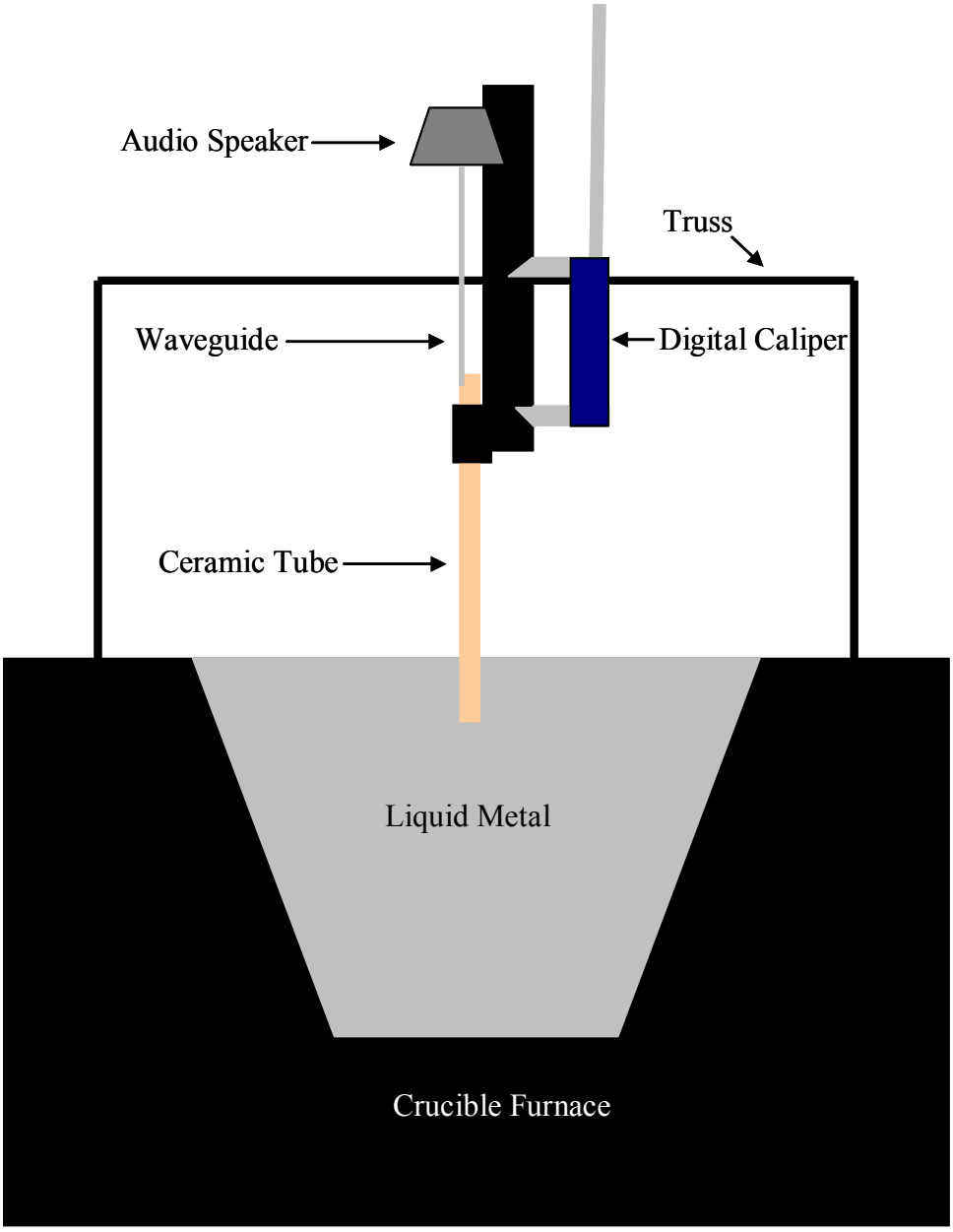

Figure 20. A schematic representation of the dynamic capillary apparatus.

The source of the vibratory energy is an audio speaker. The speaker is connected to a computer, which using the program Audacity™, plays a tone at a fixed frequency. The volume of the tone was adjusted to change the amplitude of the tone, and the voltage and current input into the speaker were measured under the range of tones and amplitudes used to determine the speaker input power. These results are presented in Figure 21. To transmit the audio energy into the tube, a cylindrical plate was epoxied to the voice coil of the speaker. A 24" long, 0.125" diameter rod was welded to the disc to serve as a wave guide and was attached to the tube using a clamp. A cross-sectional schematic of the tube, with the electrical conduction distance sensor is presented in Figure 22

Additional experiments were performed using quartz tubes in distilled water. The height the water climbed in the quartz tube, was visually determined.

The aluminum used in this test was 99.9% pure Al. To further reduce the concentration of tensioactive alkaline, and alkaline earth metals, e.g. Na, Mg, and Ca, an Ar-1%Cl_2 gas mixture was bubbled through the molten metal. This process, known as 'fluxing' is commonly used to adjust the concentration of Mg in molten Al.[52] The following reactions between chlorine and the metal take place, Table 4. The standard free energy of formation of each of the chloride listed above are large negative numbers.

Table 4. ΔG° for the reaction of Al, Mg, Ca, and Na with Cl_2 at 700°C

Reaction	ΔG° (kJ)
$Cl_2 + 2/3Al = 2/3AlCl_3$	-356.9
$Cl_2 + Mg = MgCl_2$	-447.3
$Cl_2+Ca= CaCl_2$	-629.8
$Cl_2+2Na=2NaCl$	-599.1
$Mg+3/2AlCl_3=3/2Al+MgCl_2$	-105.7
$Ca+3/2AlCl_3=3/2Al+CaCl_2$	-272.9
$2Na+3/2AlCl_3=3/2Al+2NaCl$	-242.2

The compounds $MgCl_2$, $CaCl_2$, and NaCl are solid at 700°C and have densities of 2.3, 2.15, an ad 2.16 g/cm^3, respectively. The density of molten aluminum is 2.66 g/cm^3 and as a result, $MgCl_2$, $CaCl_2$, and NaCl, float to the surface of the metal. These compounds were then skimmed off of the surface.

The residual chlorine activity can be calculated using the data in Table 4. If it is assumed that the partial pressure of $AlCl_3$ is 1 atm, then the residual partial pressure of chlorine is $pCl_2 = 7.97x10^{-20}$. However, the partial pressure of $AlCl_3$ rapidly decreases from 1 atm once the fluxing process has ceased, $AlCl_3$ disperses from the molten Al surface, and, as a result, the residual dissolved Cl concentration in the molten Al will be very low.

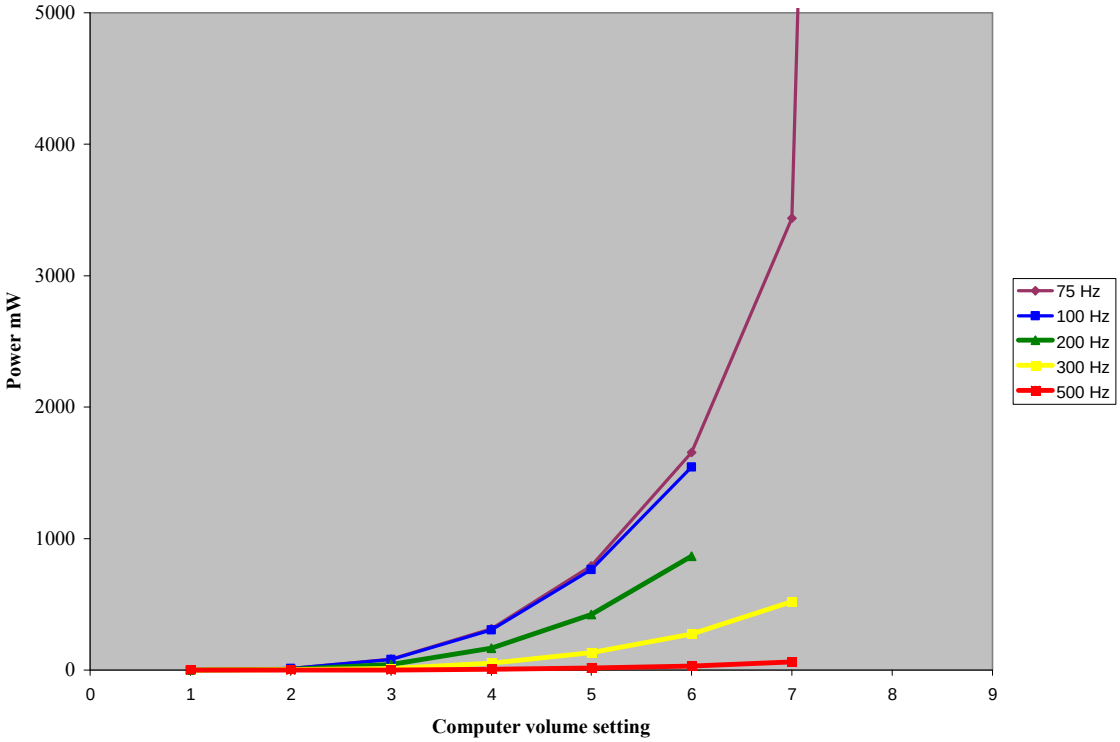

Figure 21. Power input into the speaker as a function of volume

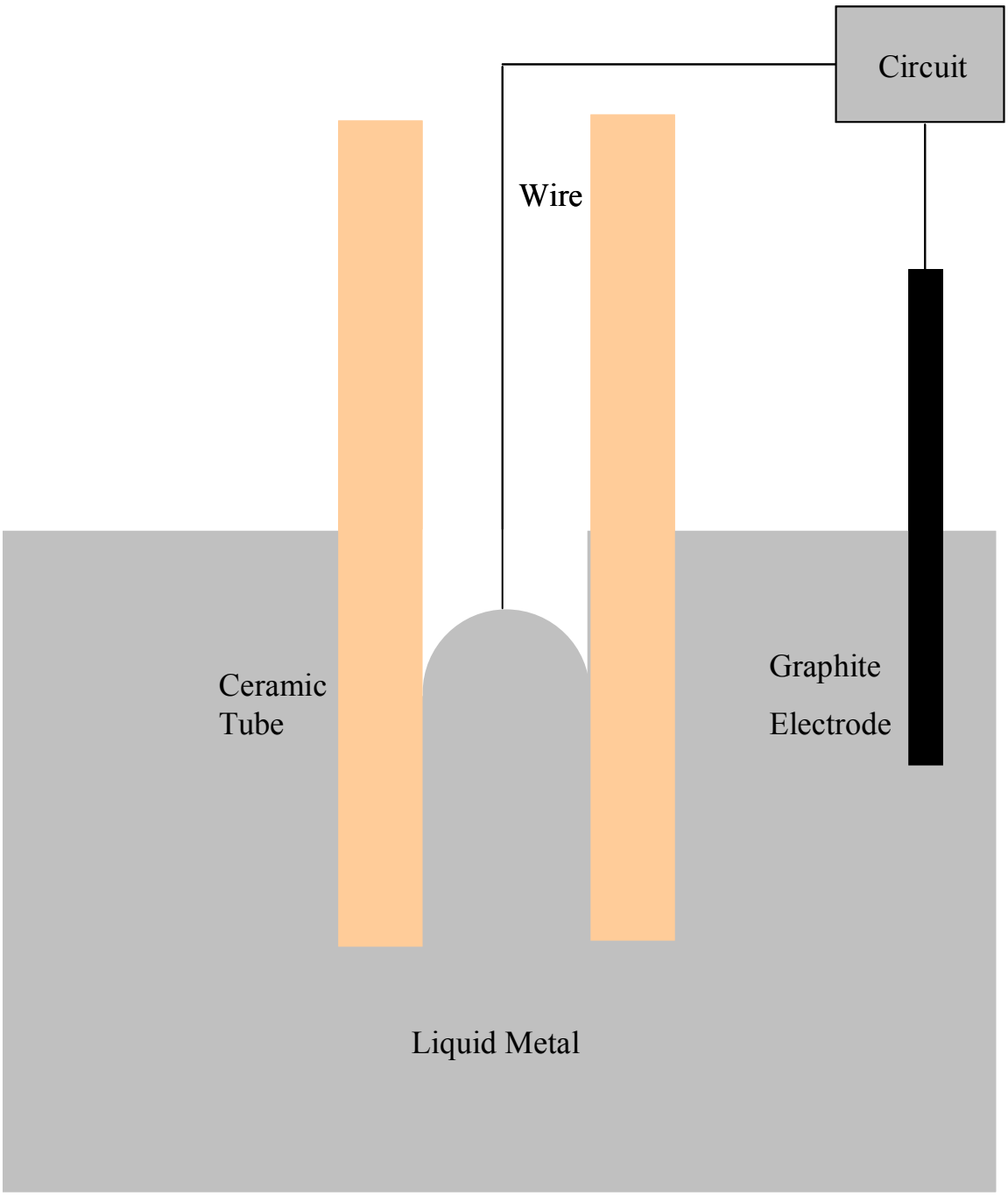

Figure 22. Cross-sectional schematic of the tube with the circuit probe

4.3 IMMERSION TESTS

Immersion tests were performed to evaluate the phase and morphological evolution of ceramic substrates in contact will liquid metals and to determine the reaction rates. These tests were performed in two devices; the tube furnace used in the sessile drop tests, and the liquid aluminum bath used in the capillary displacement test.

In the tube furnace, a ceramic substrate and solid metal were placed in a crucible, and heated in a controlled atmosphere to melt the metal and held for a prescribed time. The crucible immersion test was used to study NiO and Al_2O_3 substrates with Cu, Ag, and Sn metal. These materials were placed in alumina crucibles which were filled in a gettered Ar gas environment, and heated to 1100°C, and held for 30 minutes. Following cooling, the samples were cross sectioned and the rate of dissolution was analyzed using the scanning electron microscope.

The bath immersion tests were performed in a 50 kg bath of the liquid aluminum held at 700°C. The substrates tested were alumina, mullite, quartz and barite.

5.0 RESULTS

5.1 OXIDE DISSOLUTION

5.1.1 Immersion Tests

The dissolution behavior of oxides in liquid metals was experimentally investigated by exposing an oxide substrate in a liquid metal, and measuring the surface recession. Cross-sectional images of NiO in Cu, NiO in Ag, and Al_2O_3 in Sn are presented in Figure 23. A small amount of dissolution was observed for the Ag-NiO couple, and no dissolution could be measured in the Sn-Al_2O_3 couple, but a significant amount of NiO dissolution occurred into Cu. The experimentally measured values, of ξ, the dissolution distance, are presented in Table 5.

Table 5. Thermodynamic and kinetic data for several metal-oxide couples at 1100°C, with the interfacial compositions and calculated dissolution distance, ξ, for a 30 min. exposure

Metal	Oxide	$\Delta G°$ J/mol	D_O m^2s^{-1}	D_A m^2s^{-1}	γ	X_O	X_A	ξ μm
Cu	NiO	-106832	6.071E-09	3.624E-09	2.560E-03	7.190E-03	1.204E-02	1.69E+01
Cu	SiO_2	-269523	6.071E-09	7.572E-10	6.860E-08	2.953E-07	1.887E-04	4.54E-04
Cu	Al_2O_3	-355176	6.071E-09	3.376E-09	1.400E-09	6.915E-09	4.355E-06	9.26E-06
Ag	NiO	-8582	1.332E-08	3.376E-09	2.400E-04	2.334E-04	4.638E-04	2.35E+00
Ag	SiO_2	-259273	1.332E-08	4.88E-09	1.400E-09	3.781E-09	7.505E-05	1.37E-05
Ag	Al_2O_3	-331926	1.332E-08	3.376E-09	1.325E-10	4.086E-10	8.432E-07	1.30E-06
Sn	SiO_2	-329767	9.812E-09	2.824E-07	3.300E-07	5.144E-07	2.646E-04	2.77E-03
Sn	Al_2O_3	-406420	9.812E-09	2.824E-07	3.050E-08	5.186E-08	4.537E-06	2.56E-04

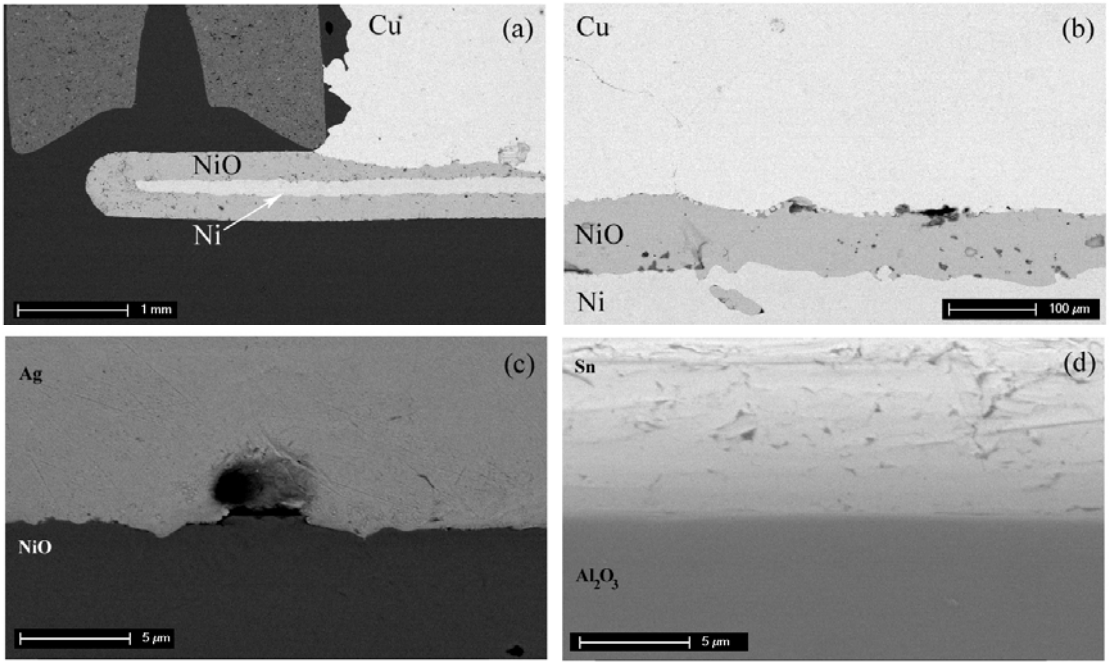

Figure 23 Cross-sectional SEM micrographs of NiO immersed in Cu (a) and (b), NiO in Ag,(c), and Al_2O_3 in Sn, following 30 minute exposure at 1100°C

5.1.2 Calculated Dissolution Rates

In order to understand the effect that diffusion has on dissolution behavior of oxides into liquid metals, the values of γ and X_O were calculated for several metal-oxide couples. The rate constant, γ, for the eight metal-oxide couples of NiO, $Al_{2/3}O$, $Si_{1/2}O$, Cu, Ag, and Sn were calculated using Equation 5.1.1**,** which was derived in Section 2.4.1.1.

$$K' = \left(\frac{\left(X_O^{A_zO} + \frac{\overline{V}_{A_zO}}{\overline{V}_M} \right)}{1 + \frac{1}{\sqrt{\pi}} \frac{\exp\left(-\gamma^2\right)}{\gamma\left[1 + erf\left(\gamma^{1/2}\right)\right]}} \right) \left(\frac{\left(X_A^{A_zO} + \frac{\overline{V}_{A_zO}}{\overline{V}_M} \right)}{1 + \frac{1}{\sqrt{\pi\Theta}} \frac{\exp\left(-\Theta\gamma^2\right)}{\gamma\left[1 + erf\left(\gamma\Theta^{1/2}\right)\right]}} \right)^z \tag{5.1.1}$$

Due to the paucity of experimental data, some values are estimated using the "Modified Hole Theory" of solute diffusion in liquid metals, developed by Cahoon.[53] The values of γ, and X_O are calculated at 1100°C and presented in Table 5, along with the relevant thermodynamic data. [53-54]

5.2 SESSILE DROP EXPERIMENTS

5.2.1 Copper-Sapphire

In order to estimate the precision and accuracy of the sessile drop method, the contact angle of Cu on (0001) face of single crystal Al_2O_3, sapphire, was determined at 1100°C. The contact angles of the three tests are presented in Table 6, and a representative in-situ micrograph is presented in Figure 24. There is a small amount of scatter in the three tests, with the contact angle 114.5°±0.4°.

The wetting behavior Cu on Al_2O_3 has been thoroughly investigated in the literature, and was examined in this study to calibrate the sessile drop measurements. The contact angle of 114.5°±0.4° is in good agreement with the literature. Shan et al.[55] investigated the wetting behavior of Cu on several orientations of single crystal Al_2O_3 at 1100°C. These authors found that the contact angle was in the range 114-116° on the $(01\bar{1}2)$, $(11\bar{2}0)$, and (0001) sapphire planes.

Table 6 Measured contact angles of Cu on Al_2O_3 at 1100°C

trial number	θ °	Average θ	± 95% CI
1	114.69	114.5	0.43
2	114.44		
3	114.36		

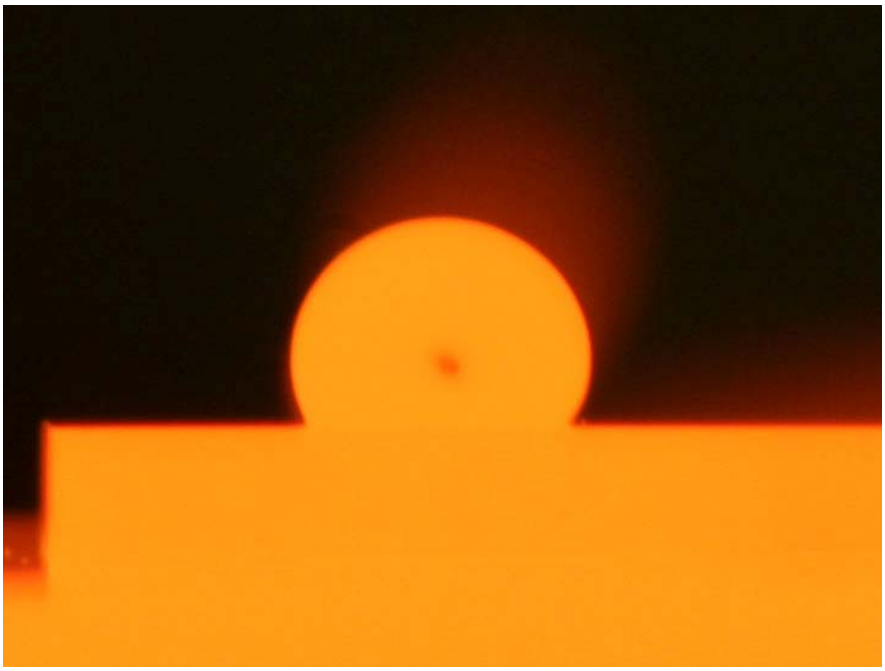

Figure 24. Photograph of Cu on single crystal Al_2O_3 substrate taken in-situ at 1100°C

5.2.2 Copper-Nickel Oxide

The sessile drop technique was used to study the wetting behavior of Cu on NiO. The experiments were performed at 1100°C in an Ar-0.6%H_2O gas mixture which was filtered through Cu turnings at 1000°C. The specimens were heated from room temperature in 1 hour, and held at 1100°C for 30 minutes, and then furnace cooled. The equilibrated gas composition is given in Table 3 and has an oxygen partial pressure which is above the dissociation pressure of NiO, but below the dissociation pressure of Cu_2O. The measurement was repeated three times and the average contact angle was found to be 78.7°±3.1°. A representative, in situ, photograph, along with cross-sectional SEM micrographs are shown in Figure 25**.** The Cu-NiO interface was no longer planar following exposure. In the solidified copper droplet, there were micron-scale, facetted NiO particles, along with smaller Cu_2O particles, Figure 25(d) and Figure 26.

The contact angle of Cu on NiO was found to be 78.7°±2.3°. The only other investigation of this system found in the literature was performed on Naidich[21] who found the contact angle to be 68° at 1200°C. However, the experimental atmosphere was not described in Naidich's work. The results of this investigation are in general agreement with the work of Naidich, Cu wets NiO, and while a 10° difference in contact angle at 100°C difference is larger than what is typically found with in a single investigation, typically $d\theta/dT \approx -0.05°K^{-1}$ [49]it can be attributed to possible differences in specimen purity or surface roughness.

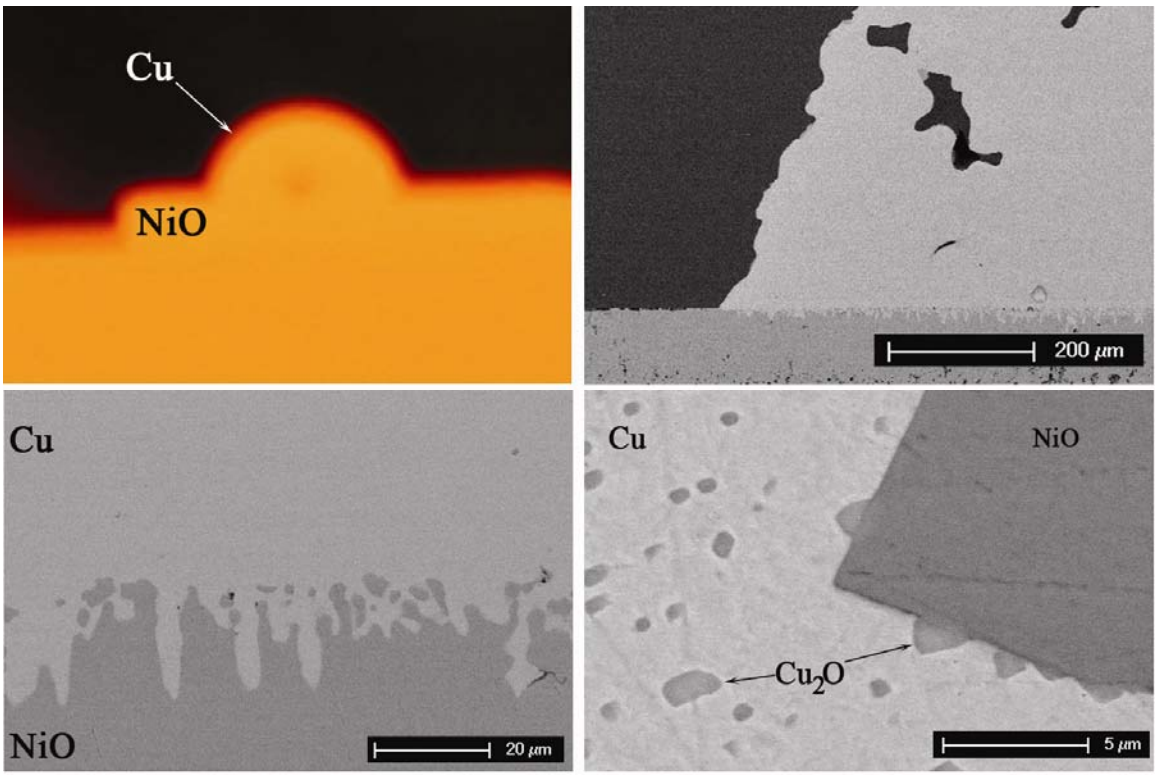

Figure 25. In-situ photograph of liquid Cu on NiO at 1100°C (Top Left). Cross sectional SEM images of (bottom left) Cu-NiO interface and (bottom right) NiO and Cu_2O particles in Cu

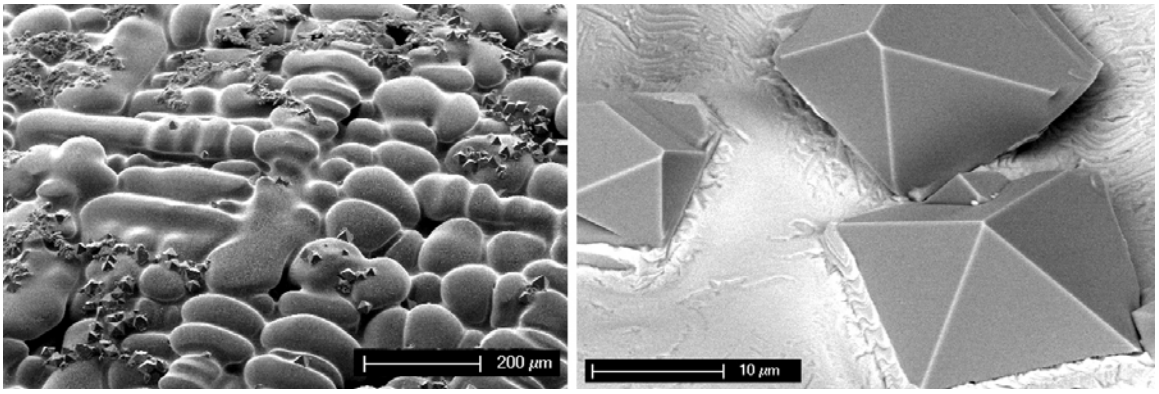

Figure 26 Low magnification surface SEM micrograph of solidified Cu (left), and higher magnification image showing facetted NiO crystals (right)

5.2.3 Cu-1Ni-NiO

Pieces of Cu and Ni, proportioned such that the molar ratio was 99Cu-1Ni, were heated at 1150°C for 1 hour in the sessile drop apparatus. The alloy was then sectioned into four pieces and re-melted to insure that the Ni was uniformly distributed through the copper. The approximate composition of the alloy was Cu-1at%Ni

An approximately 1 gram piece of the alloy was then used to perform a sessile drop test on NiO. Cross-sectional and surface SEM micrographs are shown in Figure 27, along with an in-situ photograph. The contact angle was found to be 54.4°. The interface remained planar near the triple line, but became unstable in the center of the droplet. A large area fraction of the solidified Cu droplet is covered by NiO.

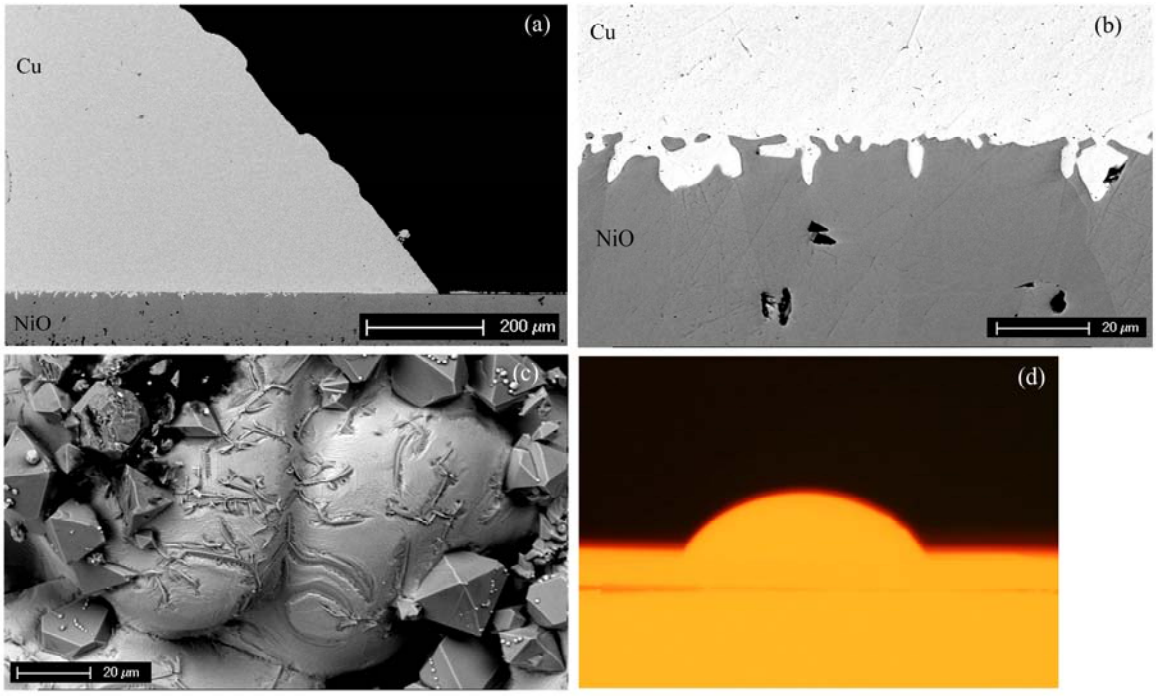

Figure 27 Cross-Sectional SEM micrographs of Cu-1Ni-NiO after 30 minute exposure at 1100°C (a) and (b), surface SEM micrograph of the facetted NiO particles on the solidified Cu surface, and (d) in-situ photograph of Cu-1Ni NiO

5.2.4 Ag-NiO

Silver was melted on NiO in an Ar-0.06%H_2O atmosphere gettered by Cu at 1000°C, as well as in air. Cross-sectional SEM micrographs are presented in Figure 28 and Figure 29, respectively. In the low pO_2 atmosphere the contact angle was found to be 96.2°, while in air, the contact angle was 78.6°.

In the low pO_2 environment, a low concentration of NiO particles was observed on the Ag surface. These particles are the angular features in the secondary electron SEM images in Figure 29(c). No oxide particles were observed on the surface of the Ag droplet exposed in air. The Ag-NiO interface, in Figure 28(a) and (b) has small amplitude undulations while the Ag-NiO interface in Figure 29(b) is planar.

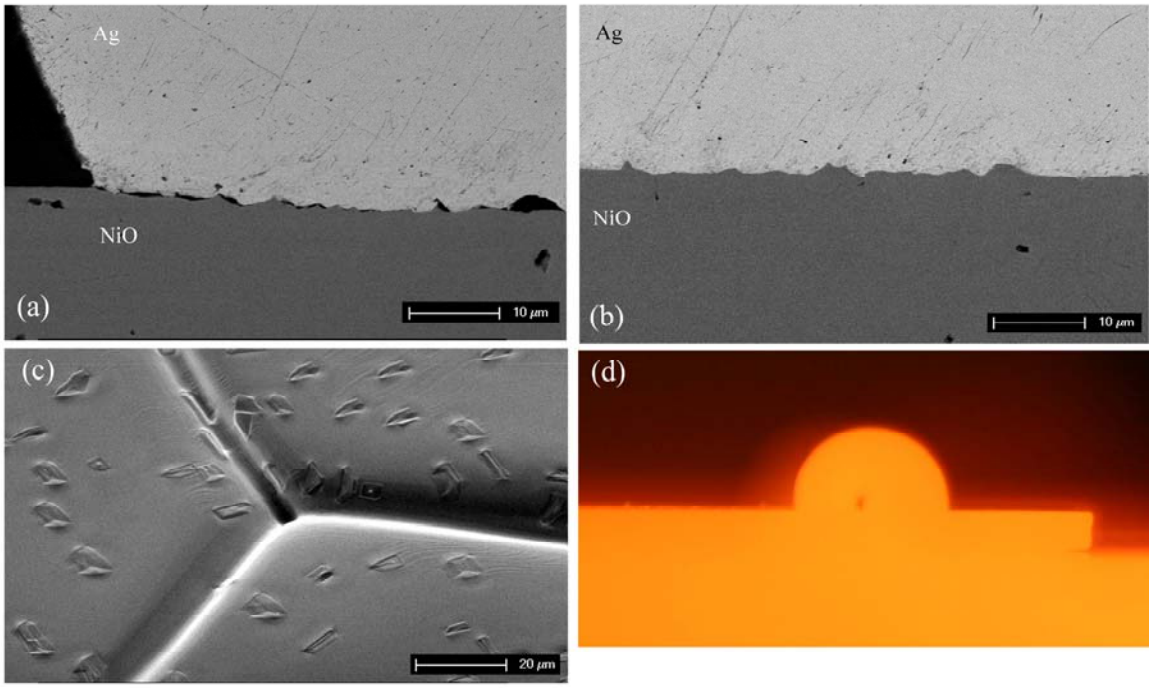

Figure 28 Cross-sectional SEM micrographs of Ag-NiO exposed at 1100°C for 30 minutes in Ar-0.06%H_2O(a) and (b), surface SEM micrograph of Ag surface, with facetted NiO particles and (d) in-situ photograph

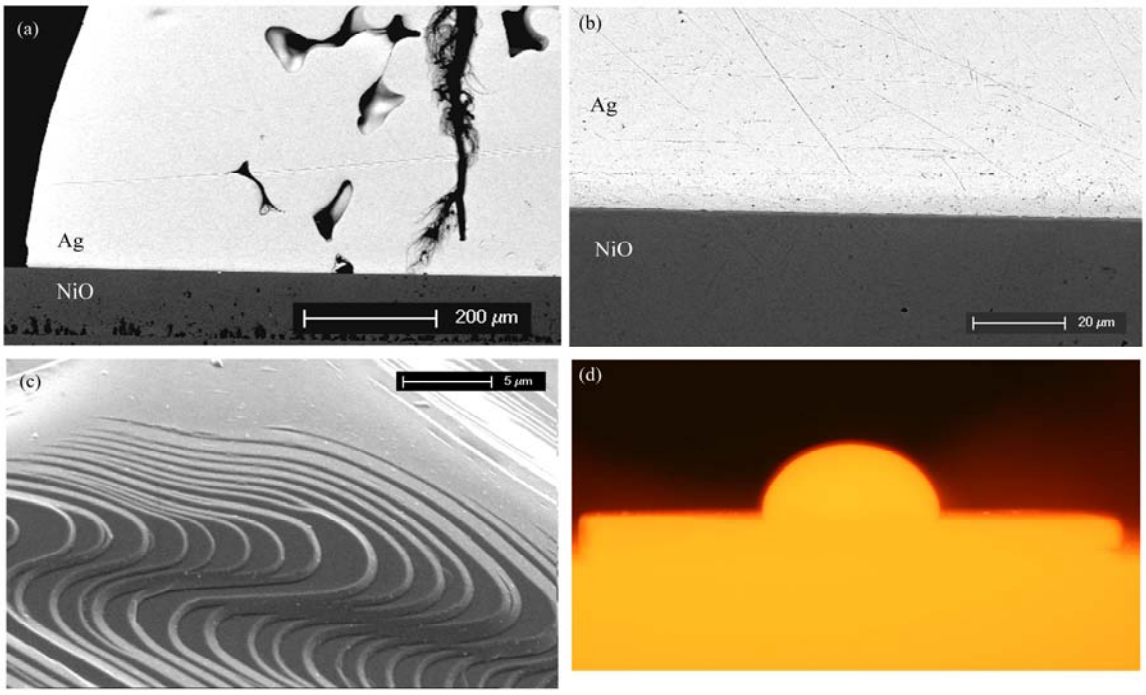

Figure 29 Cross-sectional SEM micrographs of Ag-NiO exposed at 1100°C for 30 minutes in air (a) and (b), surface SEM micrograph of Ag surface, (d) in-situ photograph

5.2.5 Copper-YSZ

Sessile drop measurements were also performed to study the wetting behavior of Cu on YSZ, using the atmosphere of Ar-0.6%H_2O gas mixture which was filtered through Cu turnings at 1000°C. In two tests, the contact angle of copper was found to be 119.1 and 120.3°, with an average of 119.7°, as shown in Figure 30. Surface SEM micrographs of the solidified copper droplet show a macroscopically dendritic structure, as did Cu solidified on NiO. Higher magnification surface micrographs show a finely ridged morphology. Cross-sectional micrographs show that the Cu-YSZ interface is planar. During the test, the grain boundaries in the YSZ substrate are delineated. Additionally, large pores are found at the metal-oxide interface. It is believed that these pores result from gas being trapped during the melting of the copper droplet.

The measured contact angles are in good agreement with Nikolopoulos and Sotirolopoulou[42] who found the contact angle of Cu on YSZ to be 122° at 1200°C. In this system, there is little oxide dissolution, and the adhesion between copper and zirconia is primarily due to van der Waals forces.

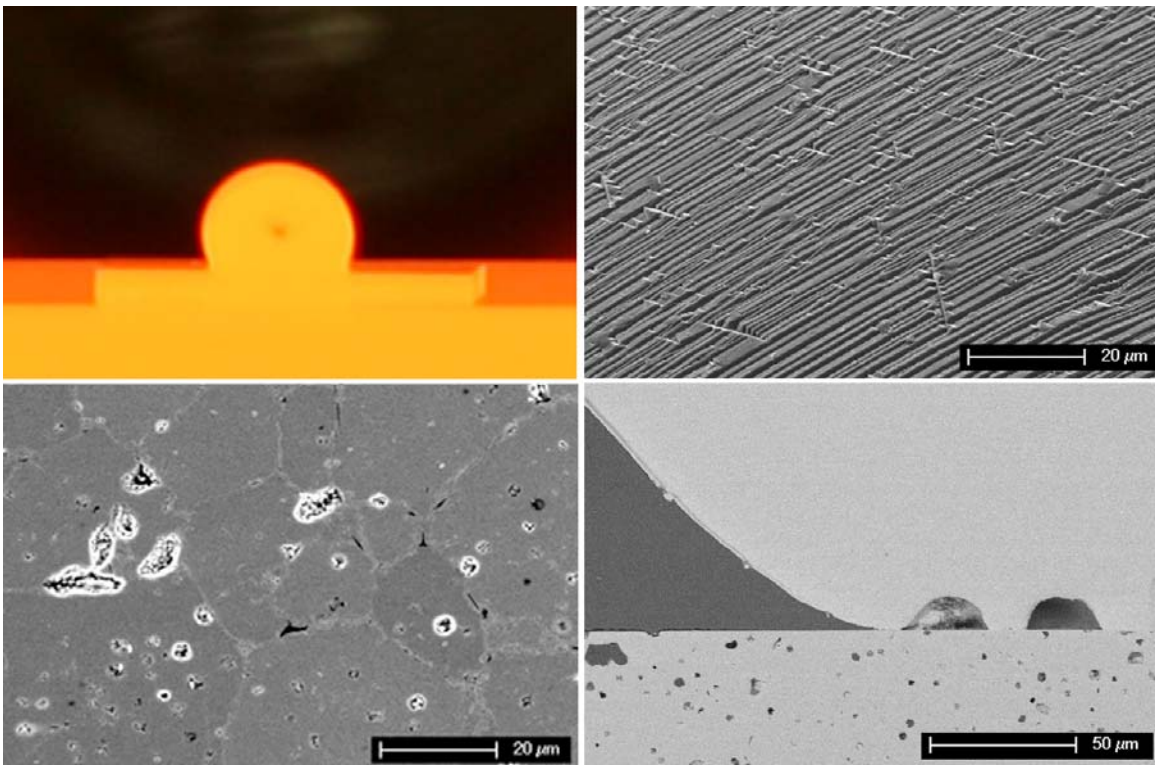

Figure 30 Cu-YSZ exposed at 1100°C: in situ photograph (Top left), solidified copper surface (Top right), YSZ surface (bottom left) and Cu-YSZ interface (bottom right)

5.2.6 Copper-YSZ-Nickel Oxide

Sessile drop measurements were also performed to study the wetting behavior of Cu on two-phase NiO-YSZ, using an Ar-0.6%H_2O gas mixture which was passed through Cu turnings at 1000°C. The contact angle of copper was found to be 96.7° as shown in Figure 31. The solidified copper surface has the same dendritic structure as did copper solidified on NiO and YSZ. Facetted NiO crystals are found on the copper surface, but not with the same density as was observed in Cu-NiO. Cross-sectional micrographs show that the Cu-NiO-YSZ does not remain planar. Pores are found near the metal-oxide interface, and in these regions, the extent of oxide dissolution is decreased.

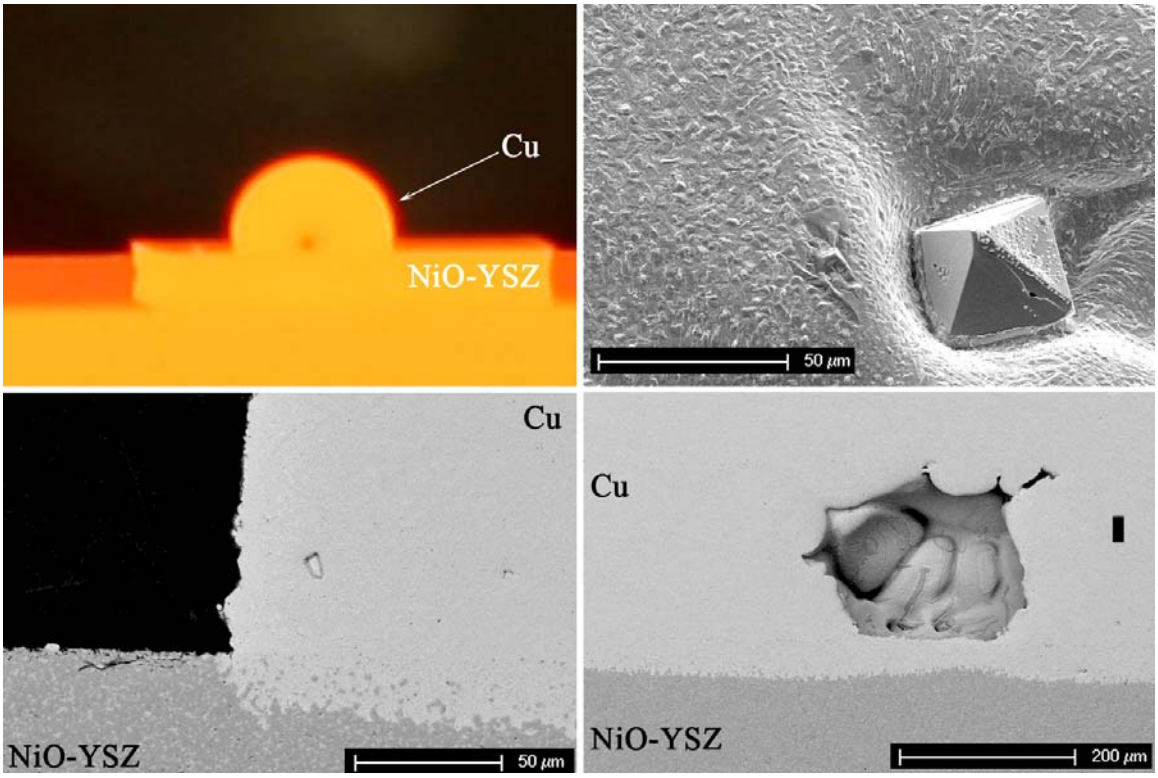

Figure 31. Cu-NiO/YSZ exposed at 1100°C: in situ photograph (Top left), solidified copper surface (Top right). Cross sectional micrographs of the Cu-NiO/YSZ interface showing oxide dissolution (bottom left) and a pore formed as a result of gas trapped during melting (bottom right)

5.3 MOLTEN ALUMINUM-CERAMIC INTERACTIONS

Aluminum-quartz, and aluminum-mullite diffusion couples were exposed at 550°C, 700°C, and 1000°C. In the Al-SiO_2 couples, extensive reaction occurred at all temperatures, however, the nature of the reaction was temperature dependent. In the Al-mullite diffusion couples, the rate of reaction was generally slower than in Al-SiO_2 couples. At 550°C and 700°C, little reaction was observed, while at 1000°C , hemispherical regions decomposed to Al_2O_3 and Si. The specifics of each exposure will now be discussed.

5.3.1 Al-SiO_2 1000°C

A quartz tube was briefly placed in the liquid metal bath at 700°C, to coat the outside of the tube, and fill the inside with liquid aluminum. The tube was then placed in the tube furnace, used in the sessile drop test, and re-heated for 1 hour at 1000°C under vacuum. Figure 32 shows cross-sectional SEM micrographs of the Al-SiO_2 diffusion couple, after a one hour exposure. The layer sequence is SiO_2/Al_2O_3/Si+Al_2O_3/Al. The thickness of the Al_2O_3 layer varies from 100-300 μm, while the Si+Al_2O_3 aggregate layer is approximately 100 μm thick. In the aggregate layer, the Al_2O_3 and Si particles are approximately 5-10 μm in thickness. Cracks are present throughout the SiO_2 substrate. At the SiO_2-Al_2O_3 interface a distinct compositional change is observed, and little to no Al is detected in the SiO_2 phase and only a small amount of Si was found in Al_2O_3. No phase with a composition near that of mullite, $Al_6Si_2O_{13}$, was found.

X-Ray diffraction was performed on a crushed section of the specimen and the diffraction pattern is shown in Figure 33. Three phases were identified, α-Al_2O_3, θ-Al_2O_3, and Si. The α-Al_2O_3 peaks are more intense than the θ-Al_2O_3 peaks.

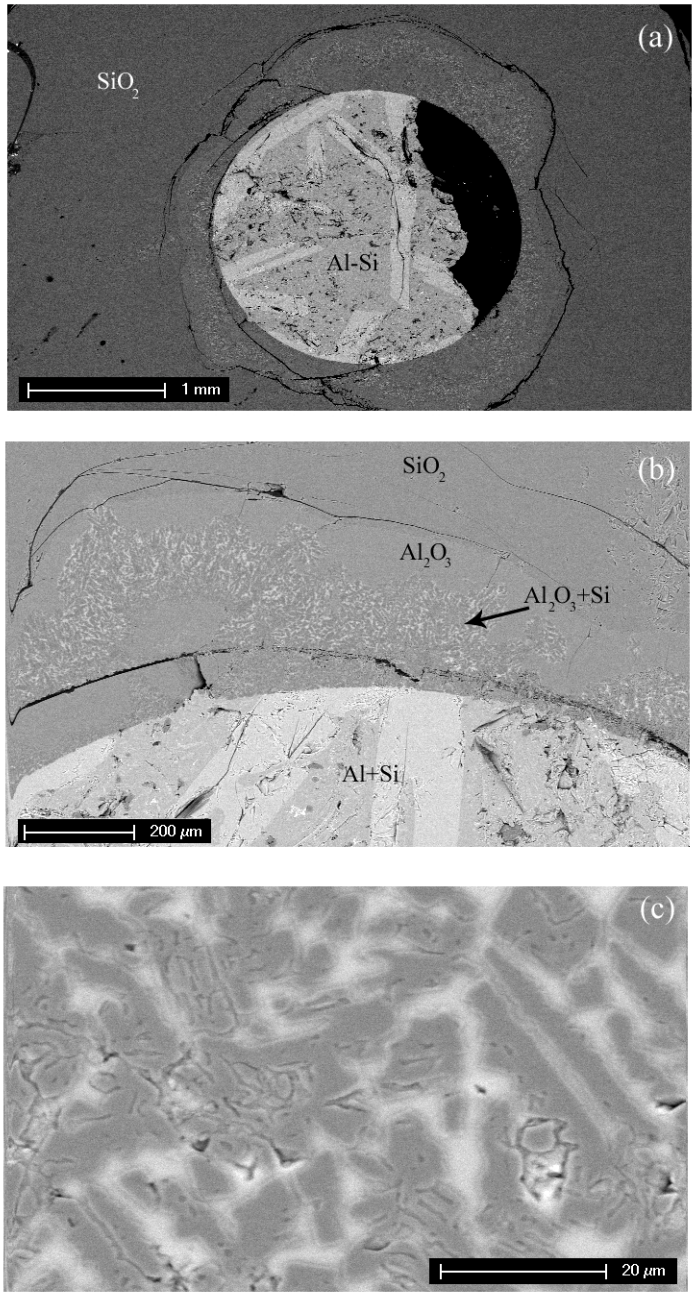

Figure 32 Cross-sectional SEM micrograph of Al-Quartz diffusion couples, exposed at 1000°C for 1 hour

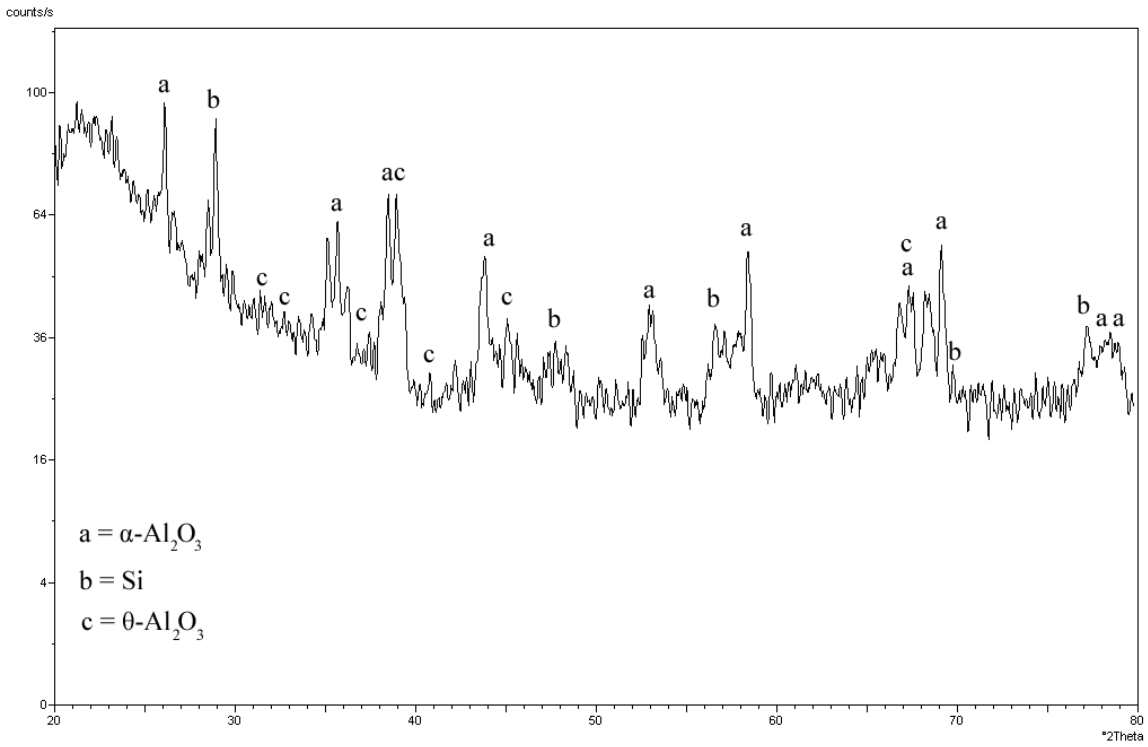

Figure 33. Powder X-Ray diffraction pattern of crushed Al-Quartz diffusion couples, exposed at 1000°C for 1 hour

5.3.2 Al-SiO_2 700°C

After a 30 minute exposure at 700°C, the layer sequence $SiO_2/Al_2O_3/Al$ was found, Figure 34. EDS line scans show the abrupt composition shift at each phase boundary and little Si is observed in the metallic phase adjacent to the Al_2O_3 layer. Interestingly, there are areas at the Al-SiO_2 interface where little to no reaction appears to have taken place, Figure 34(b). The product layer thickness increased with time, and after 2 hours the alumina layer had grown to be over 200 μm thick. Figure 35.

X-Ray diffraction was performed on a crushed section of the specimen and the diffraction pattern is shown in Figure 36. Three phases were identified, Al, Si, α-Al_2O_3, and θ-Al_2O_3. The θ-Al_2O_3 peaks are more intense than the α-Al_2O_3 peaks.

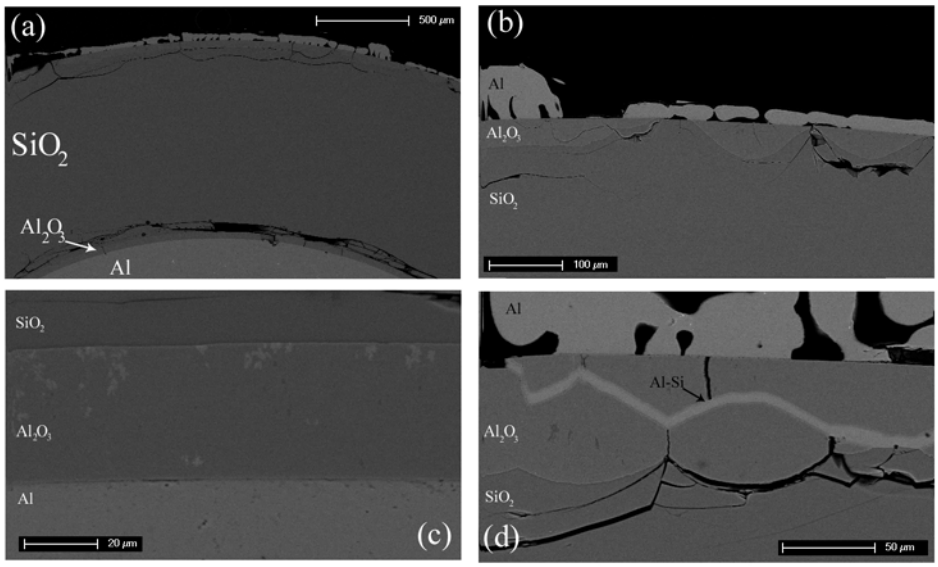

Figure 34. Cross-sectional SEM micrographs of Al-quartz diffusion couples at 700°C after 30 minutes.

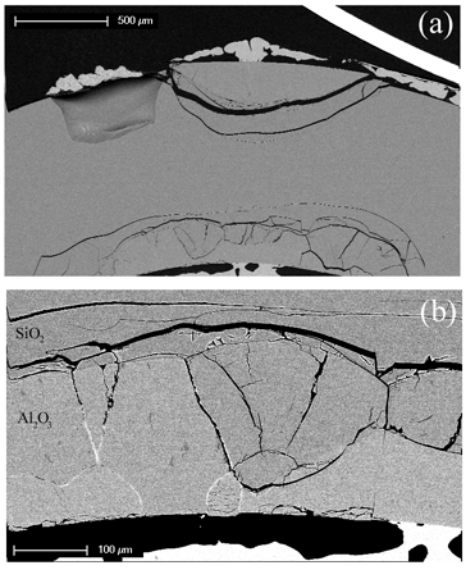

Figure 35. Cross-sectional SEM micrographs of Al-quartz diffusion couples at 700°C after 2 hours.

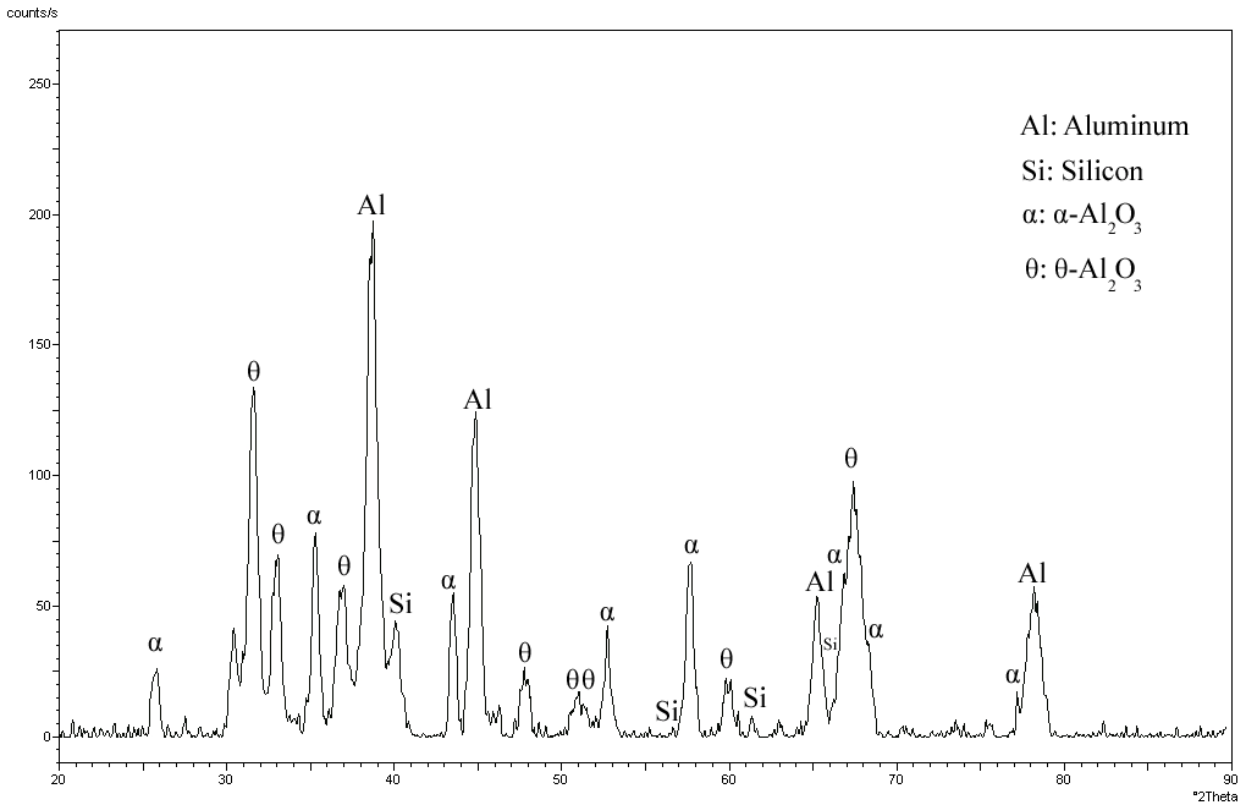

Figure 36 Powder X-Ray diffraction pattern of crushed Al-Quartz diffusion couples, exposed at 700°C for 2 hours

5.3.3 Al-SiO_2 550°C

The exposure temperature of 550°C is below the Al-Si eutectic temperature, and, therefore, no liquid phases should be produced during the exposure. However, in order to get intimate contact between Al and SiO_2, the quartz tube was placed into the liquid aluminum bath at 700°C, for a few minutes. The tube was then placed in the tube furnace used for the sessile drop tests, and exposed at 550°C for 100 hours in vacuum. Figure 37 shows that the layer sequence $SiO_2/Al_2O_3/Si+Al/Al$ was found on the outside of the tube.

No reaction was observed on the inside of the tube, and there was an approximately 1 μm separation between the Al layer and the SiO_2 substrate. It is possible that good contact was not made during the 100 hour exposure, which would explain the lack of reaction. It is also possible that there was intimate contact during the re-exposure at 550°C, and only a very thin reaction product was formed, and that the separation occurred during polishing.

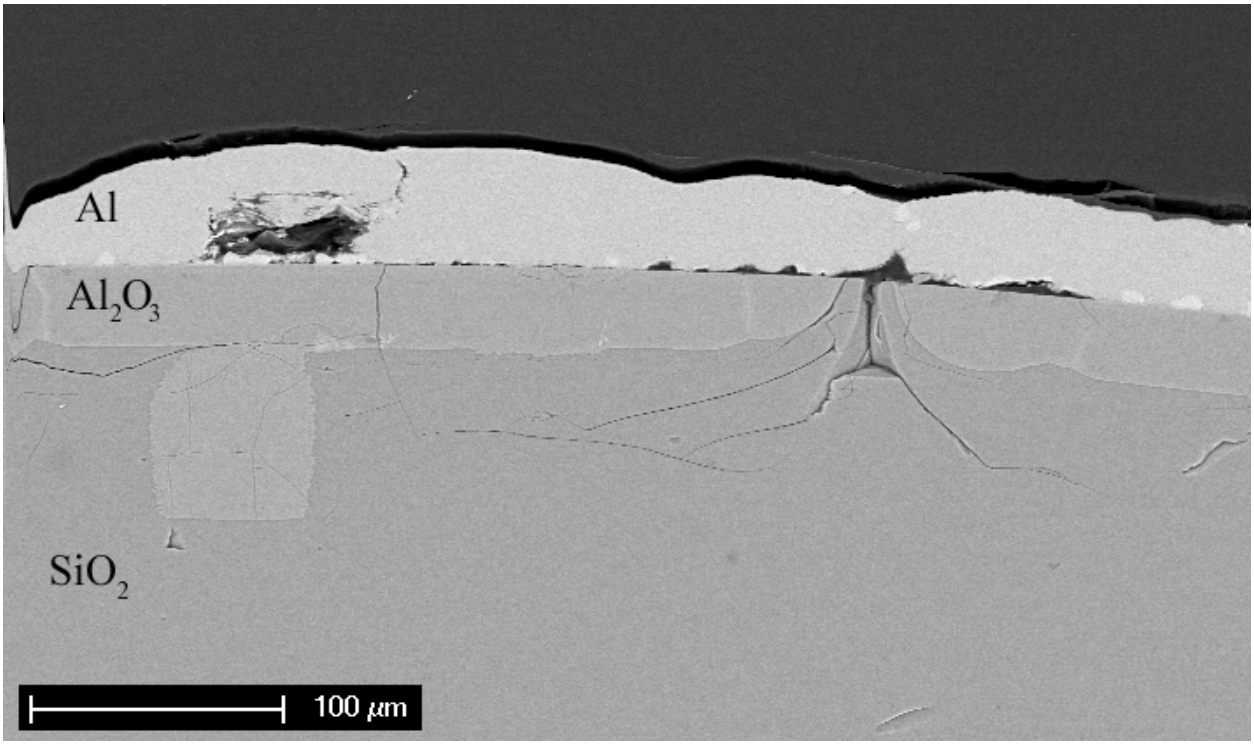

Figure 37. Cross-sectional SEM micrograph of Al-Quartz diffusion couple after 100 hours at 550°C.

5.3.4 Al-Mullite

No reaction was observed between Al and mullite after exposure at 550°C for 100 hours. At 700°C, only a thin Al_2O_3 layer was found at the mullite-Al interface, Figure 39. At 1000°C, hemispherical volumes of reaction were observed, after a 1 hour exposure, Figure 39. In the reacted area, a two phase region of Al_2O_3 and Si was present. The maximum distance the metal-oxide interface in which reaction had occurred was 200 μm, Figure 39.

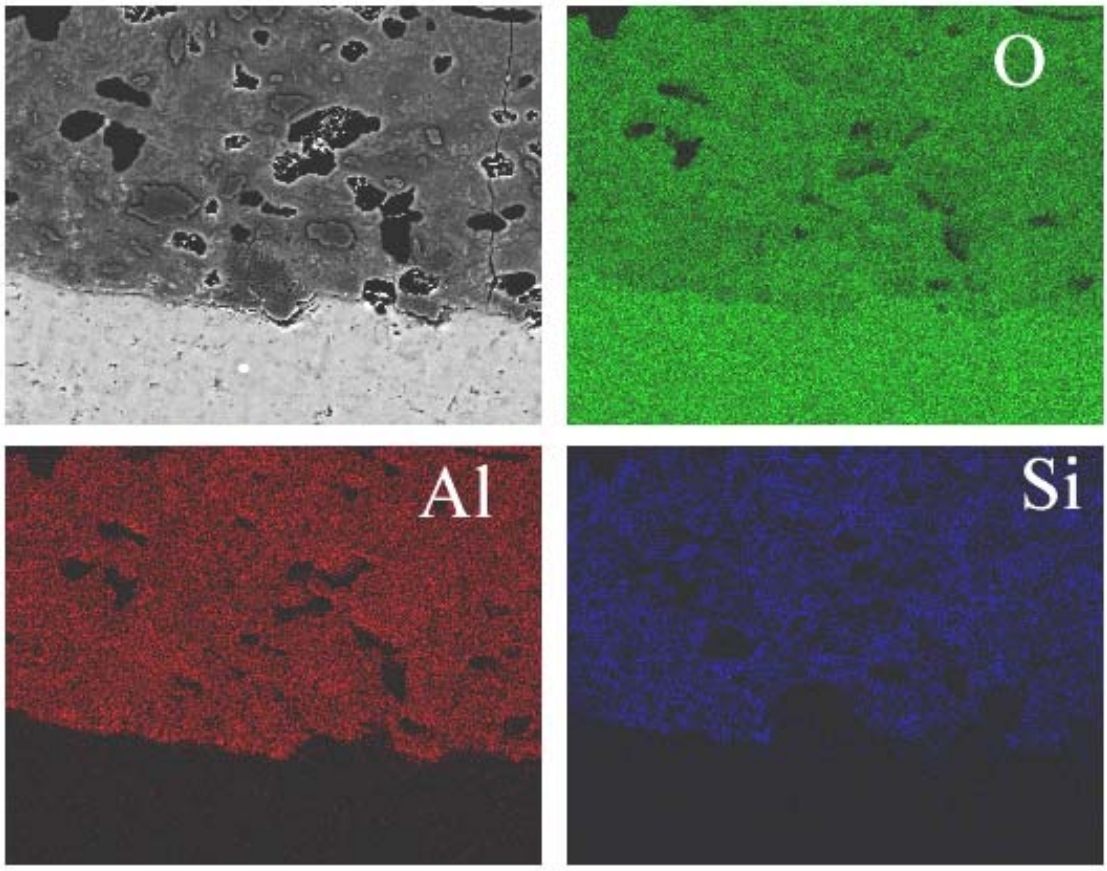

Figure 38. EDS element map of mullite-Al after 25 hours at 700°C

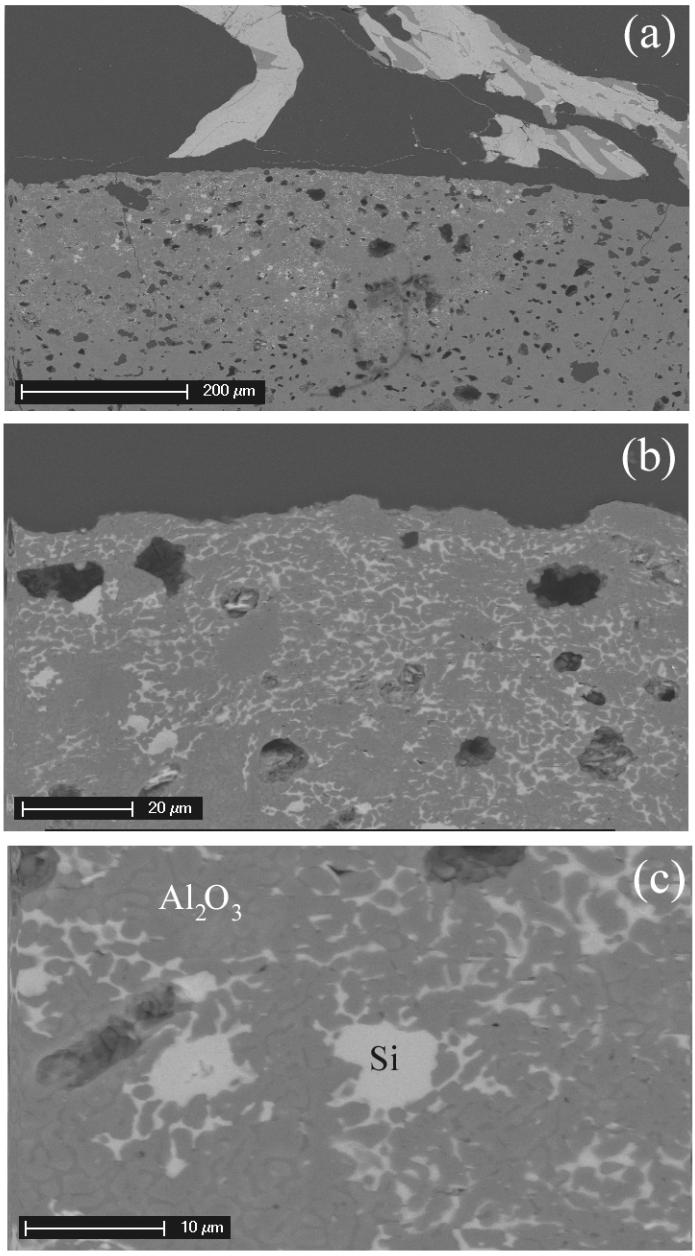

Figure 39. Cross-sectional SEM micrographs of Al-mullite diffusion couple after 1 hour at 1000°C

5.3.5 Aluminum Barite

Barite was exposed to liquid aluminum at 700°C for 20 hours. A cross-sectional micrograph is shown in Figure 40. After polishing, the aluminum-barite interface was not intact for the majority of the surface. EDS measurements did not show a variation in the composition of the barite in the center of the sample and in the region of the Al-$BaSO_4$ interface, and no reaction product was observed.

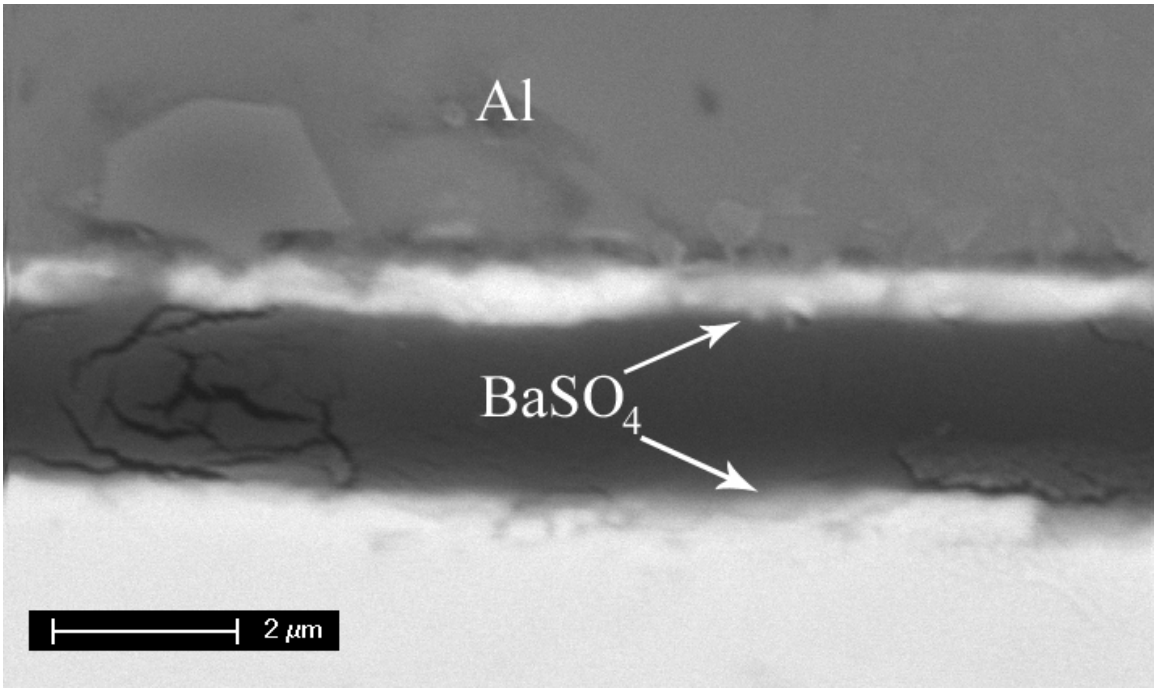

Figure 40. Cross-sectional SEM micrograph of $BaSO_4$ following immersion Al at 700°C for 20 hours

5.4 DYNAMIC CAPILLARY DISPLACEMENT

5.4.1 Al-Al_2O_3

The capillary displacement of liquid aluminum into alumina, at 700°C, was determined for tubes 1.20, 2.40, and 3.25 mm in diameter, respectively. Measurements were taken with the bottom of the tube 50.8 and 101.6 mm below the metal surface. The results are presented in Table 7, and in Figure 41. A capillary depression was observed, indicative of a contact angle greater than 90°. Vibratory energy was used to disrupt the surface oxide film, which, when continuous and adherent to the alumina tube, prevents the liquid metal from flowing to its equilibrium position. The least-squares fit of the data to the equation

$$h = -\frac{2\sigma_L \cos\theta}{\rho g r} \tag{5.2.1}$$

gives $\theta = 100.5^\circ \pm 1.6^\circ$ if the regression line is forced through the origin. This result is in good agreement with the literature value of contact angle of un-oxidized Al on Al_2O_3 of $\theta = 101^\circ$ by Laurent et al.[49] In the work of Laurent et al, the variation of contact angle was found to be $d\theta/dT$=-0.05 K^{-1}, which is in good agreement with the $d\theta/dT$ for Cu and Au on alumina, suggesting that an oxide film is not present on the metal surface.

Alternatively, the average of each contact angle is $\theta = 98.9^{\circ} \pm 1.7^{\circ}$ and if a regression line, of the form $y=mx+b$, is fitted to the data, $\theta = 107.5^{\circ} \pm 2.4^{\circ}$, with an intercept of -8.6mm. This corresponds to a capillary rise of 8.6 mm as the tube radius becomes infinitely large.

Table 7. Measured Al-Al_2O_3 capillary displacement data, and calculated contact angles

r (mm)	h (mm)	cosθ	θ
1.195	11.91	-0.186	100.7
1.195	9.53	-0.148	98.5
1.230	12.70	-0.204	101.8
1.230	15.08	-0.242	104.0
1.230	7.94	-0.127	97.3
1.230	7.94	-0.127	97.3
1.620	5.56	-0.117	96.7
1.620	4.76	-0.101	95.8
1.625	5.56	-0.118	96.8
1.625	6.35	-0.135	97.7
1.625	5.56	-0.118	96.8
1.595	3.18	-0.066	93.8
0.595	27.78	-0.216	102.4
0.595	31.75	-0.246	104.3

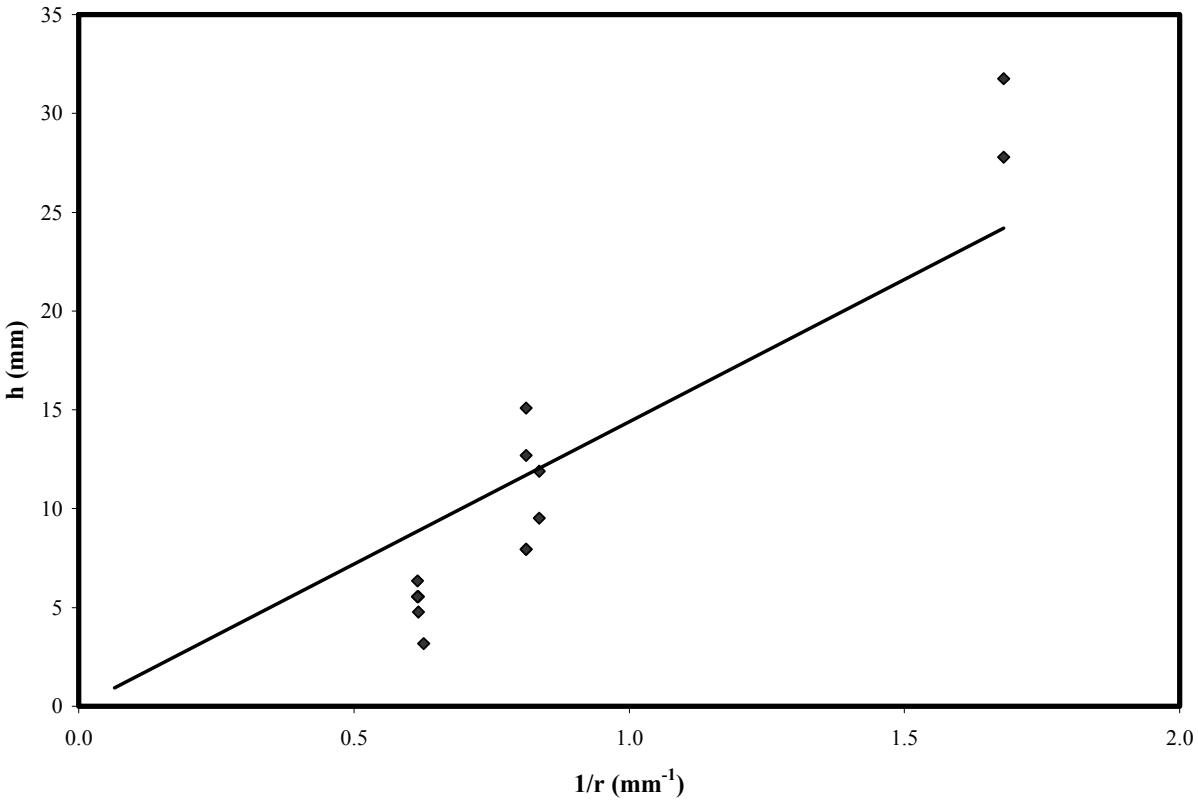

Figure 41. Capillary displacement depth as a function of tube radius for Al in Al_2O_3 at 700°C

5.4.2 Al-Quartz and Al-Mullite

Capillary displacement tests were also performed using mullite and quartz tubes. The results in the Al-Quartz system showed substantially more variability than the Al-Al_2O_3. As shown in Section 5.3, extensive reaction takes place between Al and SiO_2, and the reaction product in contact with liquid Al can be either Al_2O_3 or Si. Molten aluminum has been shown to not wet Al_2O_3 but will wet Si. As a result, a simple analysis of the wetting behavior of the evolving microstructure is not straight forward.

Al-mullite measurements performed using tubes with a diameter of 3.25 mm gave consistent results, $\theta = 104.1^\circ \pm 4.1^\circ$. However, at smaller diameters, the tubes were not strong enough to be firmly held in a manner that allowed a consistent amount of vibratory energy to be transferred to the tube, and further tests were not successfully completed. Table 8 shows the results for the Al-mullite capillary displacement experiments.

Table 8. Measured Al-Mullite capillary displacement, and calculated contact angle data

r (mm)	h (mm)	cosθ	θ
1.625	15.08	-0.320	108.6
1.625	9.53	-0.202	101.6
1.625	13.49	-0.286	106.6
1.625	7.94	-0.168	99.7

5.4.3 Water-Silica

To evaluate the influence of vibratory energy on capillary displacement, tests were performed with water and quartz. This system was used because water wets quartz, resulting in a capillary rise of the liquid, and because quartz is transparent, which allows visual inspection of water displacement. The results from the experiment are shown in Table 9 and Figure 42. The best fit contact angle $\theta = 55.6^{\circ}$ is in good agreement with the results of Hitchcock et al.[56]

When the vibratory energy was applied to the system, the total height of the water was not affected. The surface did undulate and the meniscus of the water was no longer constant.

Table 9. Measured water-quartz capillary displacement data, and calculated contact angles

r (mm)	h (mm)	cosθ	θ
1.135	-6.35	0.509	59.4
1.135	-7.14	0.573	55.0
1.135	-7.14	0.573	55.0
1.98	-3.18	0.444	63.6
1.98	-3.97	0.555	56.3
1.98	-3.97	0.555	56.3
0.52	-14.29	0.525	58.3
0.52	-15.88	0.583	54.3

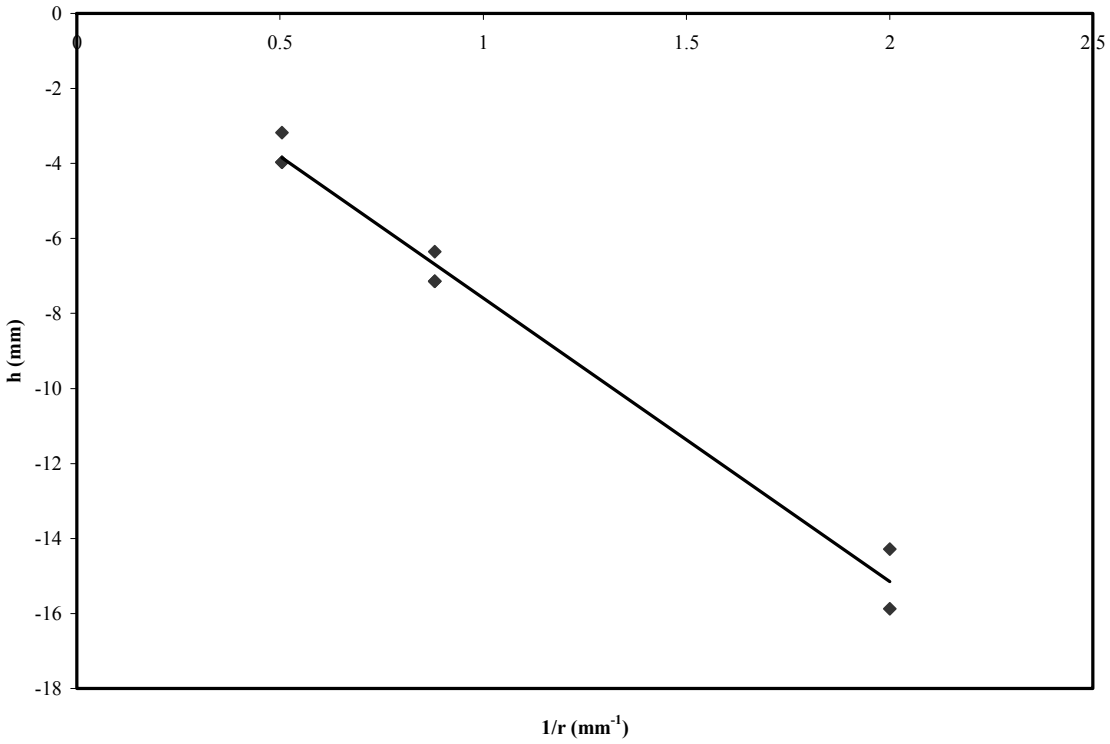

Figure 42. Capillary rise of water in quartz, as a function of tube radius

6.0 DISCUSSION

6.1 OXIDE DISSOLUTION

In section 2.4.1.1, a model was developed to determine the rate at which A_zO dissolved into an infinite bath of the molten metal M. A schematic isothermal section of a ternary phase diagram for the generic M-A-O system is presented in Figure 43(a). In this model system, M and A form a continuous liquid solution, and no ternary compounds exist. The dissolution rate was determined by calculating the range of compositions which could exist at the M-A_zO interface, then, by applying a mass balance, the particular interfacial compositions were determined, with which, the flux of each component into the metal could be calculated. This model is useful in that it can be used to predict the rate at which a non-reactive oxide will dissolve into a metal, and it can be used to determine the interfacial compositions.

In the literature, a number of models have been developed to determine, or at least rank, the adhesive strength of metal-oxide interfaces.[15-16, 20] A quantity of central importance to the strength of an interface is the metal-oxide interfacial energy. It has been proposed that metal-oxide interfacial energy decreases with increasing concentration of dissolved oxygen, resulting from metal-oxide clusters which segregate to the interface.[21] From this postulate, models have been developed to calculate the concentration of oxygen at the metal-oxide interface using thermodynamic data[16, 57], and these calculations have been compared with sessile drop data.[16]

Using the available thermodynamic data, the range of equilibrium compositions possible at the metal-oxide interface can be calculated. However, the determination of the particular

interfacial composition is not trivial. Oxides are composed of charged species, and if dissolution did not occur in a stoichiometric fashion, the oxide will become charged. In the literature, investigators have assumed that concentration of each species at the metal-oxide interface must follow the stoichiometry of the oxide.[16, 57-58]

$$X_A^* = zX_O^* \tag{6.1.1}$$

Such a boundary condition results in a diffusion path which is a straight line from A_zO to M, Path 1, Figure 43 (b).

However, once the species A and O have dissolved into the metal M, they will begin to diffuse away from the metal-oxide interface. If the interfacial compositions obey Equation 6.1.1, the oxide will be denuded of one of the species unless the diffusivities of the A and O are identical. As a result, the flux of each species must be considered.

Determining the flux of each species away from the metal-oxide interface is further complicated by the fact that as dissolution proceeds, the metal-oxide interface is receding, and by the fact that a volume change occurs when A and O are removed from the oxide lattice and dissolved into M. Even with these complications, the interfacial compositions can be determined. A hypothetical diffusion path, Path 2, Figure 43(b) shows that the dissolved interfacial oxygen concentration is hypostoichiometric, with respect to the oxide composition, when the diffusivity of oxygen is greater than the diffusivity of A. Due to the greater diffusivity, the X_O becomes greater than the X_A away from the interface.

However, the accuracy of the model can only be as good as the data which is used. One source of error in the model is the assumption that the presence of dissolved oxygen does not affect the activity of dissolved A, and *vice versa*. Consider the Cu-Ni-O system, where X_O and X_{Ni} are relatively large, and solute-solute interactions may be appreciable. The activity coefficient γ_O can be calculated as a function of X_O and X_{Ni}, Equation 6.1.2, where ε_O^O and ε_O^{Ni} are interaction parameters.

$$\ln \gamma_O = \ln \gamma_O^\circ + \varepsilon_O^O X_O + \varepsilon_O^{Ni} X_{Ni} \tag{6.1.2}$$

Similarly, γ_{Ni} can calculated

$$\ln \gamma_{Ni} = \ln \gamma^{\circ}_{Ni} + \varepsilon^{O}_{Ni} X_O + \varepsilon^{Ni}_{Ni} X_{Ni} \qquad (6.1.3)$$

Using the data of Neumann et al,[59] γ_O and γ_{Ni} can be approximated under the assumption that the concentration of oxygen and nickel are equal to the values X^*_O and X^*_{Ni} determined by Equation 6.1.4.

$$\gamma_O\left(X_{Ni}=0\right)=0.116 \qquad \gamma_O\left(X_{Ni}=X^*_{Ni}\right)=0.130 \qquad (6.1.4)$$
$$\gamma_{Ni}\left(X_O=0\right)=2.52 \qquad \gamma_O\left(X_O=X^*_O\right)=2.46$$

Inserting the values X^*_O and X^*_{Ni} leads to a change in γ_O of 10.3% and a change in γ_{Ni} of 2.4% with respect to the values calculated when solute-solute interactions are ignored, i.e. Henrian behavior.

The effect of solute-solute interactions decreases with decreasing solute concentration, therefore, the effect of solute-solute interactions will be negligible for many of the systems modeled in section 5.2. It may be possible to incorporate the interaction parameters into model described in section 2.4.1, however, it would significantly increase the complexity of the calculation, and is beyond the scope of this work.

Additionally, the model requires knowledge of the diffusivity of the species *A* and *O* in *M*. The diffusivity of oxygen in many liquid metals has been calculated by Rapp and co-workers using solid-state electrochemical methods.[60-61] However, there is not a great deal of data for metal impurity diffusion. Cahoon[53] has collected a large portion of this data, and developed a model which can be used to predict the diffusivity of solutes in liquid metals. Nevertheless, the availability of diffusion data may limit the application of the dissolution model.

A comparison of calculated and measured dissolution distances for Cu-NiO, Ag-NiO, and Sn-Al_2O_3 are presented in Table 10. The calculated and experimental results are in good agreement for the Ag-NiO and the Sn-Al_2O_3 couples, but the calculated dissolution distance of NiO into Cu is an order of magnitude small than the experimentally measured value. This discrepancy may be attributed to error propagation that results from the use of thermodynamic data in the model. It is also possible that the rate of dissolution was increased due to convective currents in the molten metal.

Table 10. Comparison of calculated and measured dissolution distances following exposure at 1100° for 30 minutes

Metal	Oxide	Calculated ξ µm	Measured ξ µm
Cu	NiO	16.92 µm	150-200 µm
Ag	NiO	2.35 µm	2-3 µm
Sn	Al_2O_3	0.26 nm	none

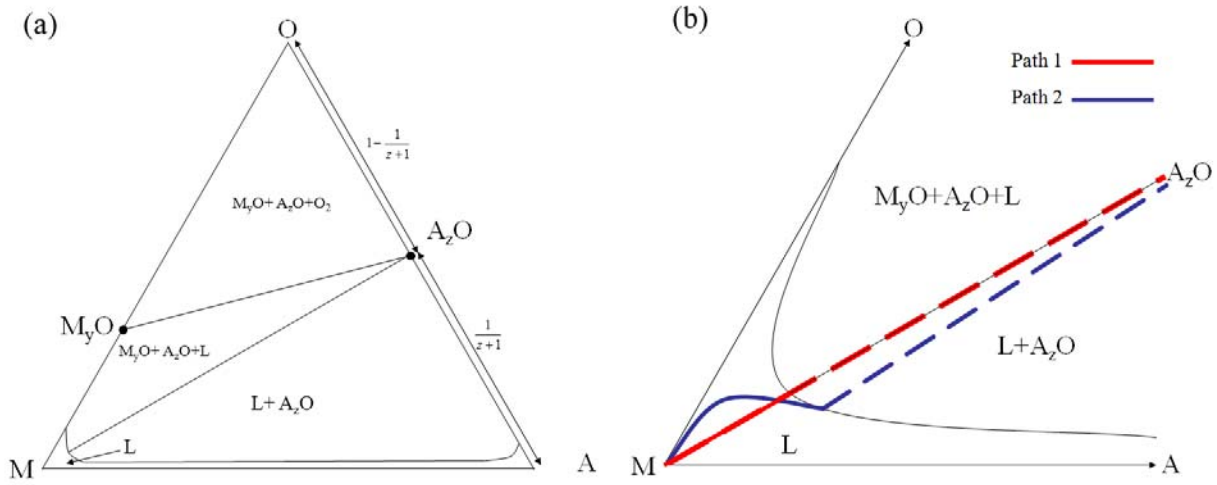

Figure 43. (a) Isothermal section of *M-A-O* ternary phase diagram and (b) *M* right corner showing hypothetical diffusion paths

This model indicated the importance of kinetics, and couple geometry in the determination of the equilibrium interfacial concentration. The simple case of an infinite couple was modeled in this investigation, and in principle, the more complicated case of a finite couple, such as a sessile drop could be modeled. However, the mathematical analysis of the finite couple becomes increasingly more complex. A schematic representation of the concentration profile of oxygen, into liquid metal, of a finite thickness *L*, is presented in Figure 44. In this case, if the oxygen partial pressure in the gas phase in equilibrium with the metal, is greater than the A_zO dissociation pressure, $X_O^S \langle X_O^*$, and as time increases, the concentration throughout the metal will approach X_O^S.

Additionally, the dissolution of the oxide A_zO can only continue when the oxygen concentration gradient is negative at the metal-oxide interface. In Figure 44, the switch between a negative and positive concentration gradient occurs between t_2 and t_3.

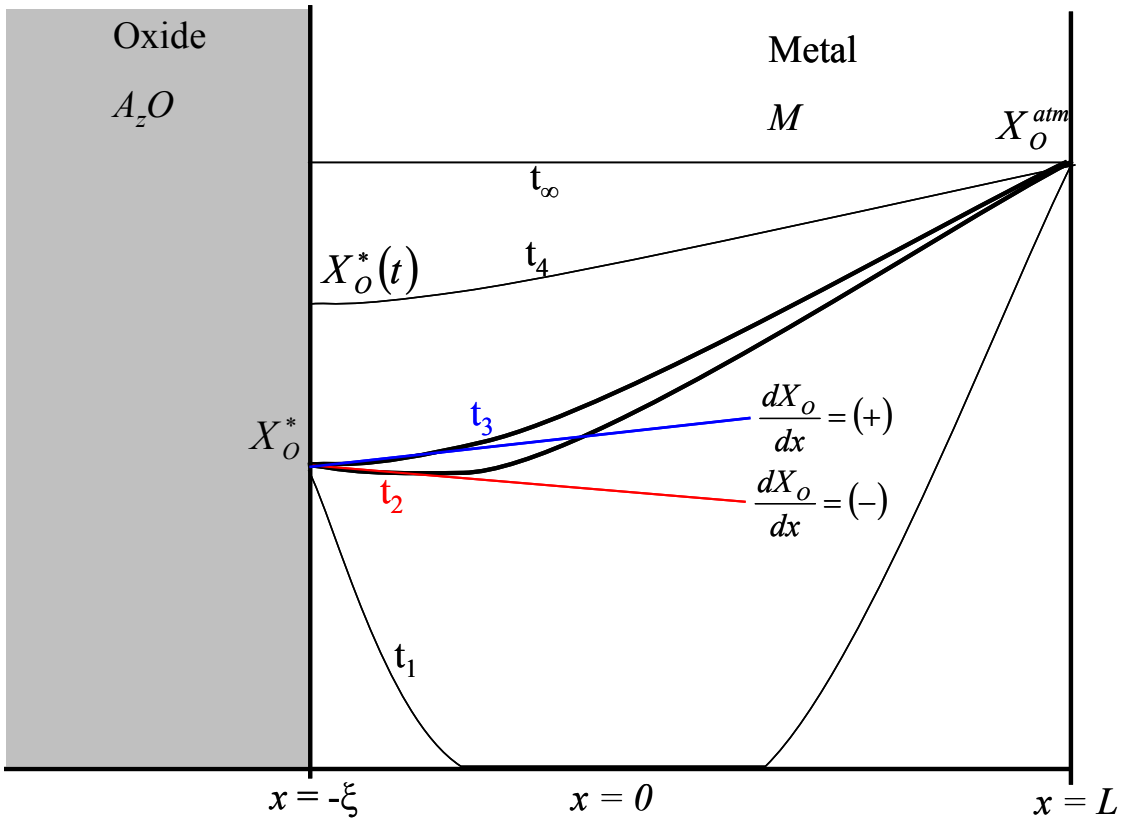

Figure 44 Schmeatic representation of the oxygen concentration profiles for A_zO dissolving into M, of thickness L, in which the X_O at the metal oxide interface is fixed by the atmosphere

6.2 SESSILE DROP DISCUSSION

6.2.1 Factors Affecting the Contact Angle

Despite the importance of wetting phenomena in many technologies, and the large number of investigations which have been performed, a fundamental understanding of the physical mechanisms which control the wetting behavior of molten metals on solid oxides is lacking. A factor which has been identified as important in predicting the wetting behavior is the amount of oxide dissolution which occurs at the metal-oxide interface. Using the results presented in Section 5.2, the effect that oxide dissolution has on the contact angle will be considered, in conjunction with influence of melt composition and experimental atmosphere.

In the sessile drops tests performed in the Ar-0.06%H_2O atmosphere, the contact angles of Cu on YSZ and Al_2O_3, were 119.7° and 114.5° respectively. The Ag-NiO contact angle was approximately 20° lower at 96.3°, and the contact angle of Cu on NiO was even lower at 78.7°. The amount of intrinsic oxide dissolution calculated in the Section 5.1.2 follows the same trend with the amount of Al_2O_3 and YSZ dissolution yielding oxygen concentrations on the order of $X_O=10^{-9}$, NiO dissolving into Ag increasing to $X_O=10^{-4}$, and NiO into Cu $X_O=10^{-3}$. (The amount of YSZ dissolution was not calculated, but based on thermodynamic considerations; it is expected to be on the order of Al_2O_3 dissolution.)

However, in the sessile drop test, the pO_2 in the gas must be higher than the dissociation pressure of the oxide substrate, A_zO, or the oxide will be reduced, and the *M-A* wetting behavior will determine the contact angle. As a result, the pO_2 in the gas phase will establish the concentration of oxygen near the triple line, Figure 45, which will be greater than the value of X_O calculated in Equation 6.2.44. If the Naidich oxygen-cluster model is operative [7, 21], then the

oxygen flux from gas phase will reduce the interfacial free energy, σ_{SL}, near the triple line, with respect to σ_{SL} in the center of the sessile drop.

The equilibrium contact angle, observed in a sessile drop test, is reached when the surface energy of the system is no longer decreased by the creation of solid-liquid interface. If the length of the metal-oxide interface is y, and δy is an incremental increase in the interfacial length, then the change in free energy of the system ΔG, can be expressed as a function of the surface energies of the system.[7]

$$G(y+\delta y) - G(y) = \Delta G = (\sigma_S - \sigma_{SL})\delta y + \cos\theta \sigma_L \delta y \qquad (6.2.2)$$

Equation 6.2.2 leads directly to Young's equation through a free energy minimization.

Further, Equation 6.2.2 shows that only the value of σ_{SL}, at the triple line will determine the macroscopic contact angle. The solid-liquid interfacial free energy, σ_{SL}, at the triple line in the metal-oxide system will be rapidly reduced as a result of ingress of external oxygen. As further inward diffusion of oxygen occurs, the total energy of the system will decrease, but the contact angle will not change. This in is agreement with the constant contact angle observed in the Cu-NiO system, and by experiments in the literature which have shown that in non-reactive metal-oxide systems, the equilibrium contact angle is achieved within a few seconds of melting.[7]

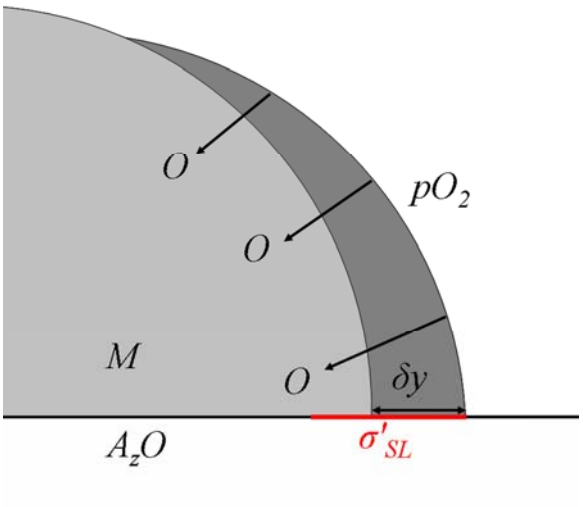

Figure 45. Schematic of a sessile drop in which the σ_{SL} has decreased near the tripleline due to oxygen diffusion from the atmosphere

6.2.1.1 The effect of M-O cluster concentration on contact angle: increasing the driving force of M to cluster

The importance of metal-oxide cluster density is further illustrated by the Cu1Ni-NiO system. The contact angle of Cu1Ni on NiO was of 54.4° which is more than 20° lower than pure Cu on NiO. Young's Equation indicates the change in contact angle must be due to either a change in surface free energy of copper due to the addition of Ni or to a change in the solid-liquid interfacial free energy.

No study has been performed in the literature on the effect of Ni on the surface free energy of Cu. However, the surface free energies of molten Cu-Fe alloys have been studied, in which it was found that Fe increased the surface tension of Cu.[62] The liquid surface free energies of Fe and Ni are both approximately 30% greater than Cu,[7] and while Cu-Fe and Cu-

Ni mixing thermodynamics are not identical, to a first approximation Ni additions to Cu should increase the surface free energy, which, all other factors being constant, should increase the contact angle. However, because Ni is more oxygen active than Cu, the amount of oxygen adsorption on the surface will increase under the experimental conditions which would decrease the surface tension.

The presence of Ni in the alloy should also increase the concentration of metal-oxide clusters. Nickel has a greater affinity for oxygen than copper and the concentration of Ni in the Cu1Ni alloy is much greater than the amount NiO which will dissolve in Cu. The increased concentration of metal-oxide clusters will decrease the metal-oxide interfacial free energy.

Conversely, the presence of Ni decreases the amount of oxide dissolution, Equation 6.2.3, where K' is the equilibrium constant described in Equation 2.4.9.

$$X_O = \frac{K'}{X_{Ni}} \tag{6.2.3}$$

This demonstrates that the concentration of metal-oxide clusters is the mechanism by which the interfacial free energy is decreased, not the dissolution of oxide.

6.2.1.2 The effect of M-O cluster density on contact angle: increasing the driving force for O to cluster

The concentration of *M-O* clusters can also be increased by increases in the oxygen partial pressure in the gas phases. In Section 5.2.4, the effect of pO_2 on the Ag-NiO contact angle was demonstrated, where it was found that the contact angle was 96.2° when Ag was melted in an Ar-0.06%H_2O atmosphere, and decreased to 78.6° when melted in air.

Oxygen in known to decrease the surface free energy of many metals, and the effect of oxygen on the surface free energy of silver has been studied by Mehrotra and Chaklader.[63] In the low pO_2 environment, the surface free energy of silver is 0.92 J/m^2, and decreases to 0.75

J/m^2 when the pO_2 is increased to 0.21 atm. However, in order for the contact angle to decrease from non-wetting, as is the case of Ag on NiO in a low pO_2 environment, to wetting, the quantity σ_S-σ_{SL} must change from negative to positive. Changes in σ_L only change the magnitude of the cos(θ).

Therefore, if the change in σ_S as a function pO_2 is small[64], the quantity σ_{SL} must be decreased due to the increase in pO_2. The increase in pO_2, and, therefore, the dissolved oxygen concentration should increase the concentration of Ag-O clusters. The increased Ag-O cluster concentration should decrease the solid-liquid interfacial free energy which will decrease the contact angle.

Mehrotra and Chaklader[63] have studied the effect of oxygen partial pressure on the contact angle of Ag on Al_2O_3. Their results agree with the Ag-NiO results of this investigation in that the contact angle decreases with increasing oxygen partial pressure. However, in the Ag-Al_2O_3 system, all of the contact angles are obtuse. Therefore, a reduction in the Ag surface free energy would have a tendency to increase the contact angle, making cos(θ) a larger negative number. The observed decrease in the contact angle is therefore attributed to the decrease in Ag-Al_2O_3 interfacial free energy. The magnitude of the quantity $d\sigma_{SL}/dpO_2$ is greater than the increase in the quantity $d\sigma_L/dpO_2$. This result suggests that the decrease in Ag-NiO contact angle with increasing oxygen partial pressure is also due to the decreasing $\sigma_{SL,}$ presumably resulting from the increased concentration of Ag-O clusters, rather than the decrease in Ag surface free energy.

6.2.1.3 The factors affecting the contact angle: summary

The magnitude of the solid-liquid interfacial free energy, σ_{SL}, has a strong effect on the contact angle. In the literature, it has been proposed that the concentration of *M-O* clusters at the metal-oxide interface has a strong effect on the solid liquid interfacial energy. This proposal has been supported in this work by showing that if the tendency for clustering is increased by increasing

the concentration of a metal species, in this case Ni, which has a higher affinity for oxygen then the solvent molten metal, the contact angle decreases due to increase in *M-O* cluster concentration. Also, if the concentration of dissolved oxygen in the molten metal is increased, as was done in the Ag-NiO experiments by increasing the oxygen partial pressure in the atmosphere, the contact angle will decrease due to the increase in *M-O* cluster concentration. In both cases, the tendency for the oxide to dissolve was decreased, showing that the *M-O* cluster concentration, not the tendency for oxide dissolution, affects the contact angle.

Additionally, it was demonstrated that it is not essential for the solid-liquid interfacial free energy of the entire area of solid-liquid interface to be modified by the segregation of *M-O* clusters for the contact angle to change, because only the solid-liquid interfacial free energy of the area near the triple line will affect the spreading of the liquid metal to equilibrium contact angle. This is a new proposal, and in conjunction with the oxide dissolution model described in Sections 2.4.1.1, 5.1, and 6.1 it has been shown that the contact angle cannot be predicted by the thermodynamic data which describe oxide dissolution, because the influence of oxygen from the atmosphere determines the oxygen concentration near the triple line. These results will be presented in a forthcoming paper.[65]

6.2.2 Interface Stability

In Section 5.1, the dissolution behavior of an oxide into a liquid metal was examined and the analysis was applied to the dissolution behavior of NiO into Cu. When NiO is dissolving into an infinite bath of Cu, the concentration profiles of the dissolved Ni and O are in the form of an error function, which allows the maximum amount of dissolution. However, in the sessile drop configuration, the liquid bath cannot be approximated as infinite, and after a certain exposure time, oxygen will begin to accumulate at the edge of the droplet, decreasing the oxygen concentration gradient, which will decrease the oxygen flux, Figure 46 and Figure 47**.**

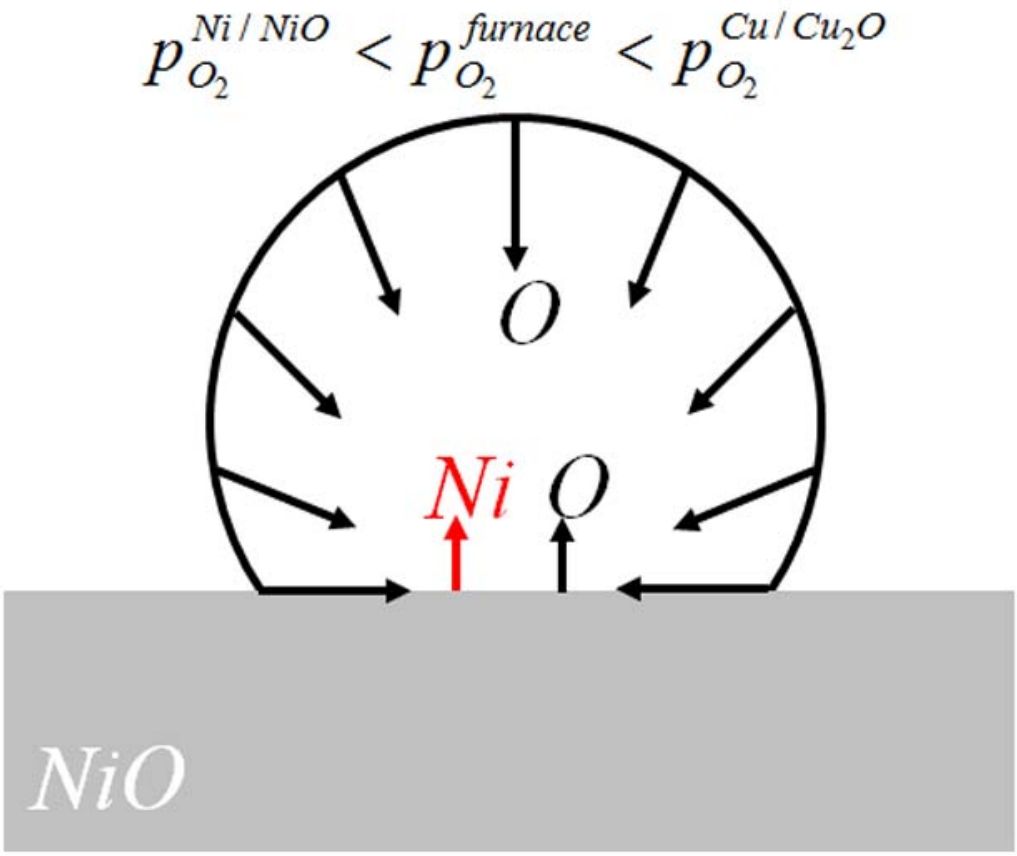

Figure 46 Schematic of sessile drop showing oxygen ingress into the metal from the atmosphere

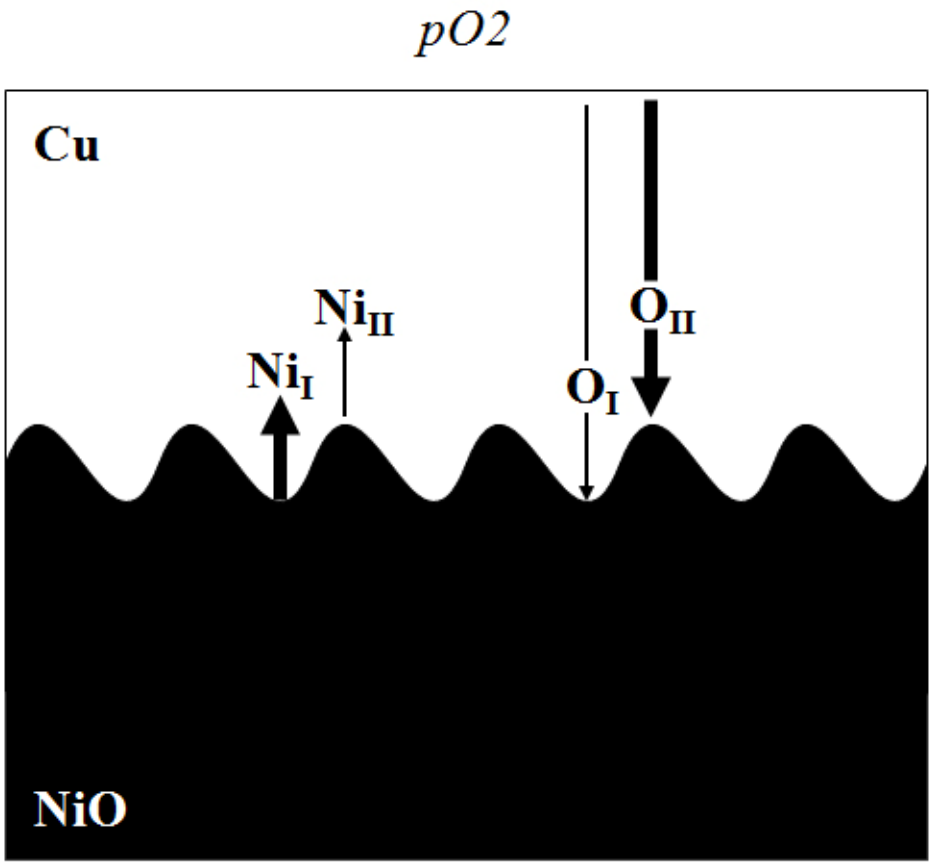

Figure 47. Schematic of unstable Cu-NiO interface

Further, due the presence of oxygen in the gas phase surrounding the sessile drop, oxygen will dissolve into the Cu. Indeed, the oxygen partial pressure in the gas phase is an order of magnitude greater than the local oxygen partial pressure at the Cu-NiO interface. As a result, there is a flux of oxygen toward the metal-oxide interface.

The rate at which NiO dissolves into Cu is dependent on the flux of Ni and O away from the Cu-NiO interface, and when there is a flux of oxygen from the atmosphere, the rate of dissolution is retarded. Under these conditions, there is a tendency for the initially planar Cu-NiO interface to become unstable.

The mechanism by which the interface becomes unstable is similar to that by which the solid metal-oxide interface becomes unstable, as described in Section 2.4.2.3. If a perturbation develops at the metal-oxide interface, the distance between the top of the perturbation and the gas-metal interface will be less then the bottom of the perturbation, Figure 47. The decrease in distance between the top of the perturbation and the gas-metal interface decreases the magnitude of the oxygen concentration gradient, which decreases the rate at which NiO will dissolve. As a result, the rate at which the dissolution occurs at the bottom of the perturbation will be greater than at the top. As this process continues, the height of the perturbation will increase, resulting in an increasing difference between the dissolution rates at the top and bottom of the perturbation.

An unstable interface was also observed in the Ag-NiO sessile drop, exposed at a low pO_2. The diffusivity of oxygen in silver is greater than in Cu, and as a result, a shorter amount of time is necessary until the concentration gradient at the metal oxide interface becomes positive, stopping dissolution, and the amplitude of the unstable interface is less than in the Cu-NiO sessile drop.

In the Ag-NiO sessile drop exposed in air, the interface remains planar. The increased pO_2 in the gas phase increases the oxygen concentration on the surface of the Ag droplet, and

time necessary for the positive concentration gradient to develop is so short that minimal dissolution occurs.

The interface of the Cu-1at%Ni-NiO sessile drop also became unstable, but the amplitude was less then Cu-NiO. At the metal-oxide interface, the dissolution process can be viewed to follow the Equation 6.2.3

$$NiO \overset{Cu}{=} \underline{Ni} + \underline{O} \tag{6.2.3}$$

For which, at equilibrium, the concentration of O, and Ni must follow the equation.

$$K' = X_O X_{Ni} \tag{6.2.4}$$

Therefore, when Ni is alloyed into Cu prior to melting, the equilibrium oxygen concentration at the interface decreases. The decreased interfacial oxygen concentration decreases the amount of oxygen which must diffuse toward the metal-oxide interface to develop the positive concentration gradient, which prevents further oxide dissolution from occurring.

The mechanism in which the metal-oxide interface goes unstable should apply to all metal-oxide sessile drop couples. However, in many circumstances, the equilibrium constant, K', in Equations 6.2.3 and 6.2.4 is so small, that the flux of external oxygen is much greater than the initial concentration of oxygen at the metal-oxide interface. Therefore, a limited amount of dissolution can occur before the positive concentration gradient prevents further oxide dissolution, and the growth of interfacial perturbations. This is the case on the Cu-Al_2O_3 tests, as well as the Ag-NiO sessile drop test which was performed in air.

6.2.3 Heterogeneous surfaces

The Cu-NiO-YSZ system was investigated in Section 5.2.6 to analyze the effect that a non-wetting phase, YSZ, had on the wetting behavior of Cu on NiO. This system was chosen as an analogue to the Al-refractory matrix-metallophobic agent system, which is present in the aluminum processing industry.

The contact angle of Cu on NiO-YSZ substrates is plotted in Figure 48, as a function of area fraction YSZ. The addition of YSZ to the surface of NiO was found to increase the contact angle. The increased contact angle did not strictly follow the rule of mixtures dependence described in Cassie's Law[7, 36]. Rather, the dependence followed the relationship of Horstemke and Schöder[39] for an advancing contact angle. The paucity of data in this investigation limits the strength with which the model of Horstemke and Schöder is supported, but the trend, suggested in their work, applies to the data in this investigation.

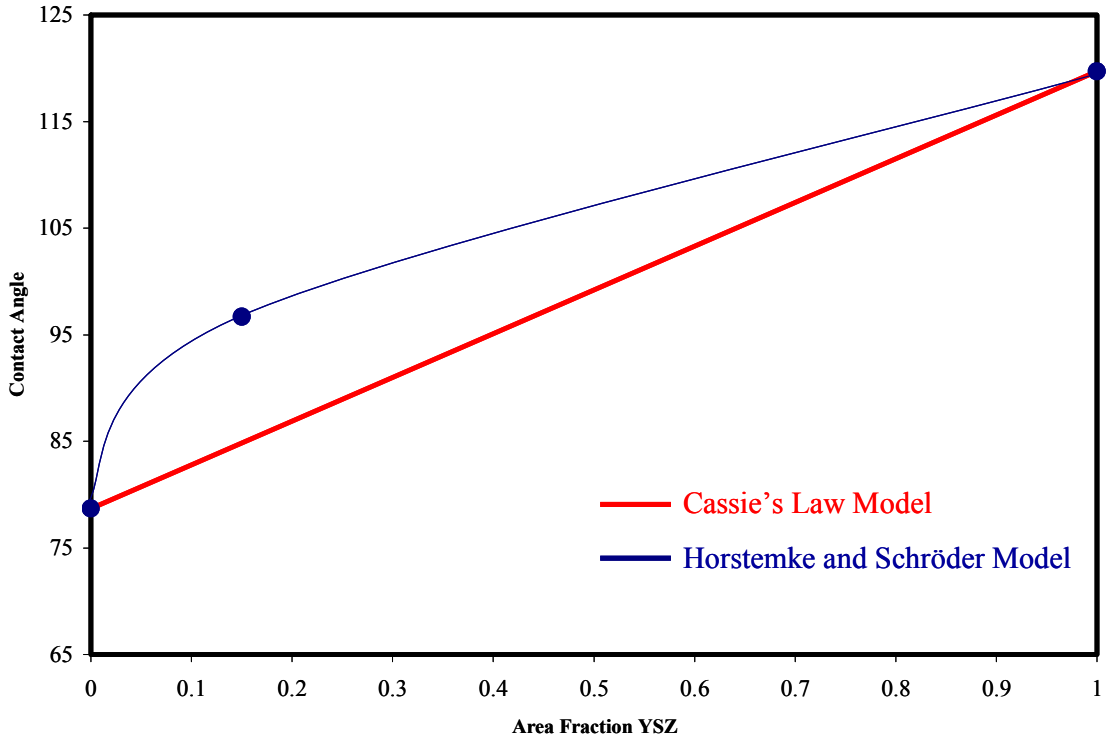

Figure 48. Contact angle of Cu on NiO-YSZ substrates, as a function of area fraction YSZ

6.3 MOLTEN ALUMINUM-CERAMIC INTERACTIONS

6.3.1 Aluminum-Silica

When liquid Al is in contact with SiO_2, reaction occurs, resulting in the layer sequence $SiO_2/Al_2O_3/Si+Al/Al$. This type of layer sequence occurs when there is a change in slope in the metal-oxide phase boundary, in the oxygen potential-composition phase diagram, Figure 8. In such a system, if the layer sequence $SiO_2/Si/Al_2O_3/Al$ developed, oxygen would increase its activity by diffusing through the Si layer to continue the formation of Al_2O_3, Figure 49. A schematic of the Al-Si-O, pO_2-composition phase diagram is presented in Figure 50, which shows how the activity of oxygen, at the $Si\text{-}SiO_2$ phase boundary increases with increase in Al activity.

The basic reaction mechanism is shown schematically in Figure 51. Initially, liquid aluminum reacts with SiO_2 to form Al_2O_3, which grows into the SiO_2, and rejects Si into the liquid Al. Brumm and Grabke[66] have determined the parabolic growth rate of different Al_2O_3 polymorphs, grown on NiAl, in the temperature range 500-1200°C. After a 1 hour exposure, the alumina thickness would be 35 nm, 350 nm, and 3.5 μm at 550°C , 700°C, and 1000°C,

respectively. This growth rate is more than an order of magnitude slower than the observed reaction rates. The relatively sluggish growth of alumina rules out the possibility that the overall reaction rate was controlled by solid state diffusion.

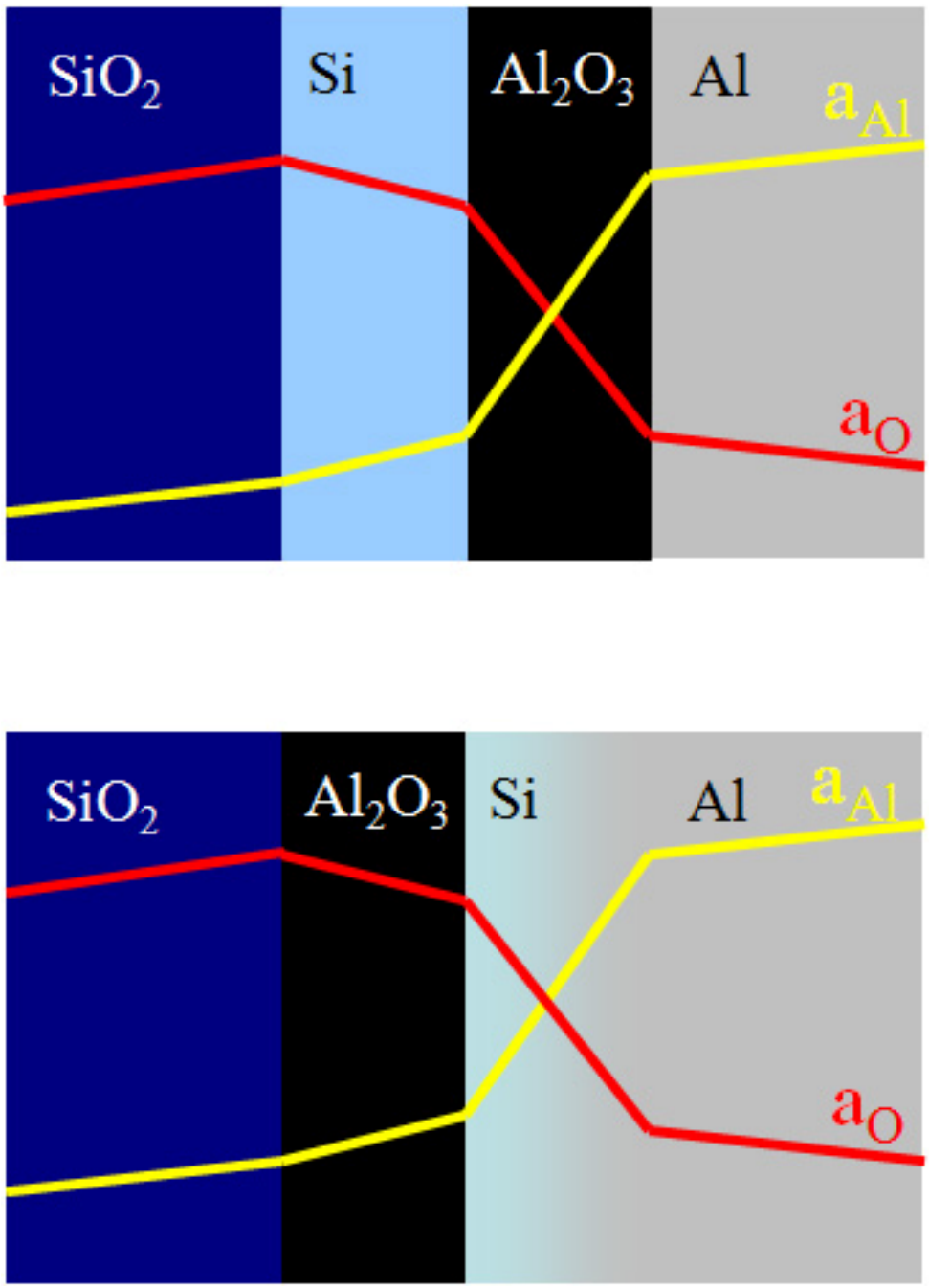

Figure 49. Aluminum and oxygen activity profiles across possible layer sequences of an annealed Al-SiO_2 diffusion couple. The top layer sequence is thermodynamically impossible, for systems with phase diagrams of the type shown in Figure 8.

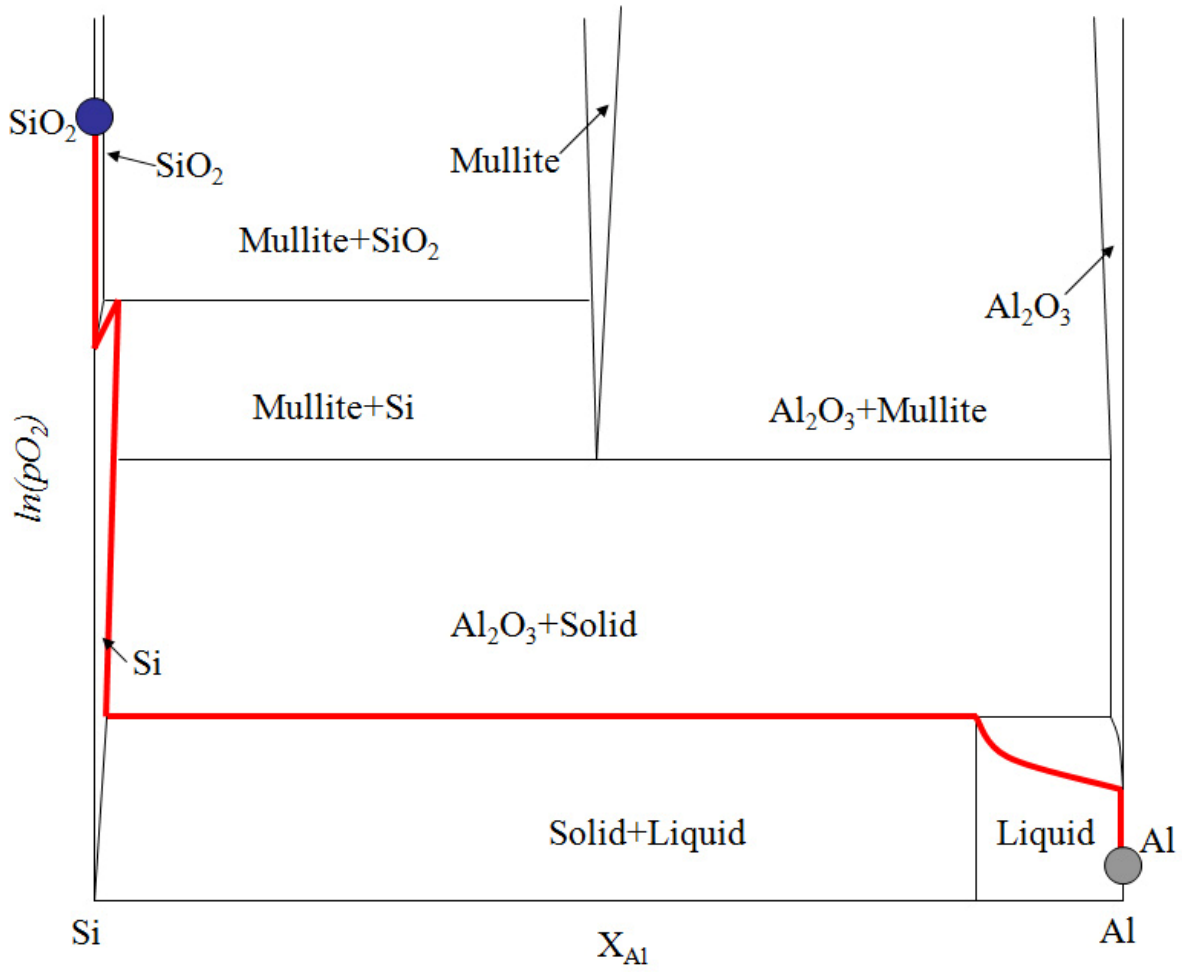

Figure 50. Schematic composition-*pO2* phase diagram for the Al-Si-O system, with Al-SiO_2 reaction path, (red)

The reduction of silica, Equation 6.1.1

$$3SiO_2 + 4Al = 2Al_2O_3 + 3Si \tag{6.1.1}$$

results in the decrease in the total volume and puts the Al_2O_3 layer into tension. The ratio of the product to reactant volume, *PBR*, is significantly less than unity,.

$$PBR = \frac{2V_{Al_2O_3}}{3V_{SiO_2}} = 0.78 \tag{6.1.2}$$

As the Al_2O_3 layer grows, the stored elastic strain energy increases, and once a critical thickness is reached, cracking occurs. Liquid aluminum can then flow through the crack to the SiO_2 surface and cause further reaction. This oxide growth followed by cracking sequence occurs repeatedly throughout the exposure. The reaction rate is initially controlled by the rate of oxide growth and cracking. As the thickness of the Al_2O_3 layer increases, so does the distance Al must diffuse to reach the SiO_2 surface, and, eventually, liquid phase diffusion becomes rate controlling.

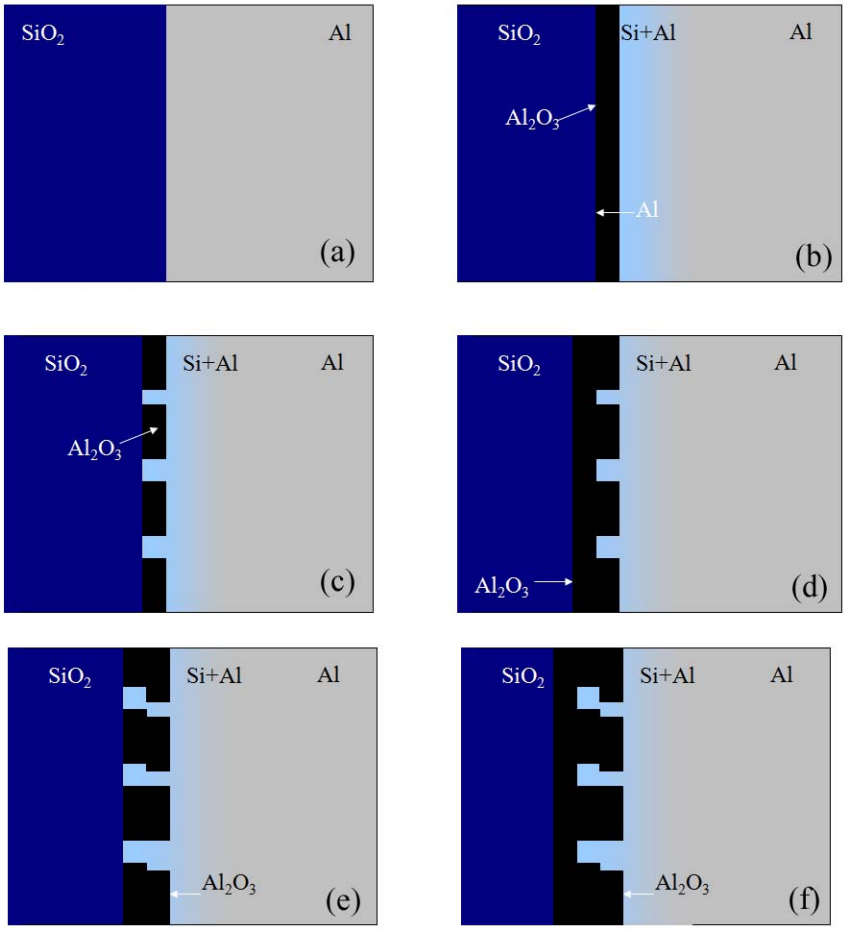

Figure 51. Schematic representation of reaction mechanism between Al and SiO_2

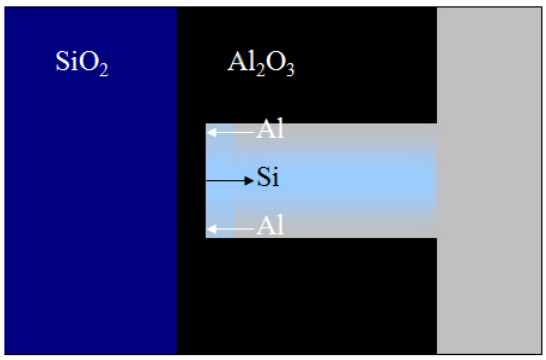

Figure 52 Schematic of liquid aluminum, flow through cracks.

Table 11 Calculated γ-Al_2O_3 thickness after 1 hour exposure in air.

Temperature (°C)	Oxide Thickness (μm)
550	0.03
700	0.35
1000	3.47

The absence of a Si rich phase after exposure at 700°C is a curious result. One possibility is that the Si can diffuse into liquid aluminum at a great enough rate to remove the Si rejected from the reduction of SiO_2. The diffusivity of Si in liquid Al is not found in the literature, but if the diffusivity is estimated to be equal to the self-diffusivity of Al, then the flux of Si through liquid Al can be approximated. If the reservoir of Al is sufficiently large that concentration profile of Si is in the form of an error function, the solution to Fick's second law is

$$X_{Si} = X^*_{Si} erfc\left(\frac{x}{\sqrt{4D_{Si}t}}\right) \tag{6.1.3}$$

where X^*_{Si} is the interfacial concentration of Si. As a first approximation, it can be assumed that pure Si is formed at the SiO_2-Al interface and $X^*_{Si}\left(\frac{mol}{cm^3}\right) = \frac{1}{\overline{V}^M_{Si}}$ where $\overline{V}^M_{Si}$ is the molar volume of Si.

Using Equation 6.1.4, the flux of Si at *x=0* can be determined, and integrating with respect to time, the total amount of the Si which diffuses into Al can be determined.

$$M_{Si} = \int_0^{t'} D_O \frac{2}{\sqrt{\pi}} \frac{X^*_{Si}}{\sqrt{4D_{Si}t}} dt = \frac{X^*_{Si}}{\sqrt{\pi}} \sqrt{D_{Si}t'} \tag{6.1.4}$$

However, because Si is only diffusing through cracks, the area fraction of cracks must be estimated to determine the amount of Si which flows from the SiO_2 interface. The amount of Si removed, as a function of crack area fraction is presented in Figure 53, along with the equivalent thickness of SiO_2 which has dissolved. If it is assumed that 1% of the interface is cracked, then

the amount of SiO_2 reacted is less than the observed value. A crack area fraction of 5% would result in an amount of SiO_2 similar to the observed amount of reacted SiO_2.

In the above analysis, it was assumed that diffusive flow was the mechanism by which Si is removed. However, if there is convective flow in the liquid Al, the rate of Si removal will increase. The 700°C exposures were performed in a larger Al bath in which temperature gradients may exist, which can promote convective flow.

At 1000°C, a distinct Si phase was found. The increase in temperature markedly increases the rate of SiO_2 reduction, while the diffusive flux of Si into Al is only slightly increased. Additionally, the experiments were performed with only a finite amount of Al in contact with SiO_2. As a result, the Si concentration profile will no longer be in the form of an error function, and the flux of Si will be further decreased. Consequently, the rate of Si removal will no longer be great enough to keep up with the reduction of SiO_2, and Si is enriched at the Al-Si interface, eventually precipitating solid Si.

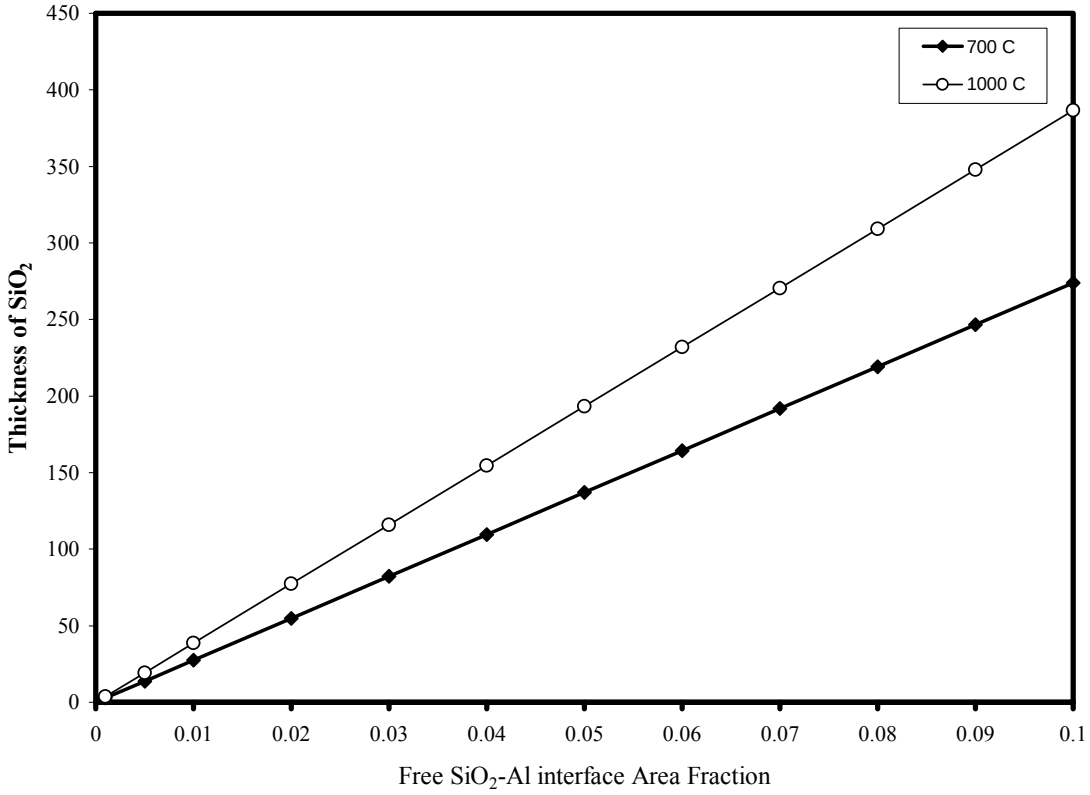

Figure 53 The amount of Si which could be removed from the Al-SiO_2 interface as a function of free interface. The thickness of SiO_2 corresponding the given amount of Si is calculated as a function of free interface.

When the Al-SiO_2 diffusion couple was annealed at 550°C, below the eutectic temperature, there is no apparent reaction product formed in the inside of the tube. If the alumina reaction layer that forms at higher temperatures forms at 550°C, and then cracks due to tensile stress, further reaction may not be possible because solid aluminum cannot flow to the new SiO_2 surface. Solid state diffusion would then control the rate of reaction, and, as calculated above, the growth rate of γ-Al_2O_3 is extremely slow at 550°C.

The Al-SiO_2 reaction path, is shown on an isothermal section of the Si-Al-O ternary phase diagram, Figure 54. According to the phase diagram, the layer sequence should be

$SiO_2/Al_6Si_2O_{13}/Al_2O_3/Si/Al$. However, as can been seen in the EDS concentration profiles, Figure 55**,** the Al_2O_3 phase is adjacent to SiO_2. Therefore, there is either a very thin layer of mullite, which was not resolved in the SEM, or mullite was not able to crystallize at the relatively low exposure temperatures.

Hallstedt et al.[67], have studied the behavior of Mg-Al_2O_3 metal matrix composites. The Mg-Al_2O_3 system is analogous to the Al-SiO_2 system in that the metal phase has a thermodynamic driving force to reduce the oxide, and a ternary oxide, $MgAl_2O_4$, is known to be stable. In their investigation, MgO was found to be adjacent to Al_2O_3, and using TEM, no $MgAl_2O_4$ was found at the interface.

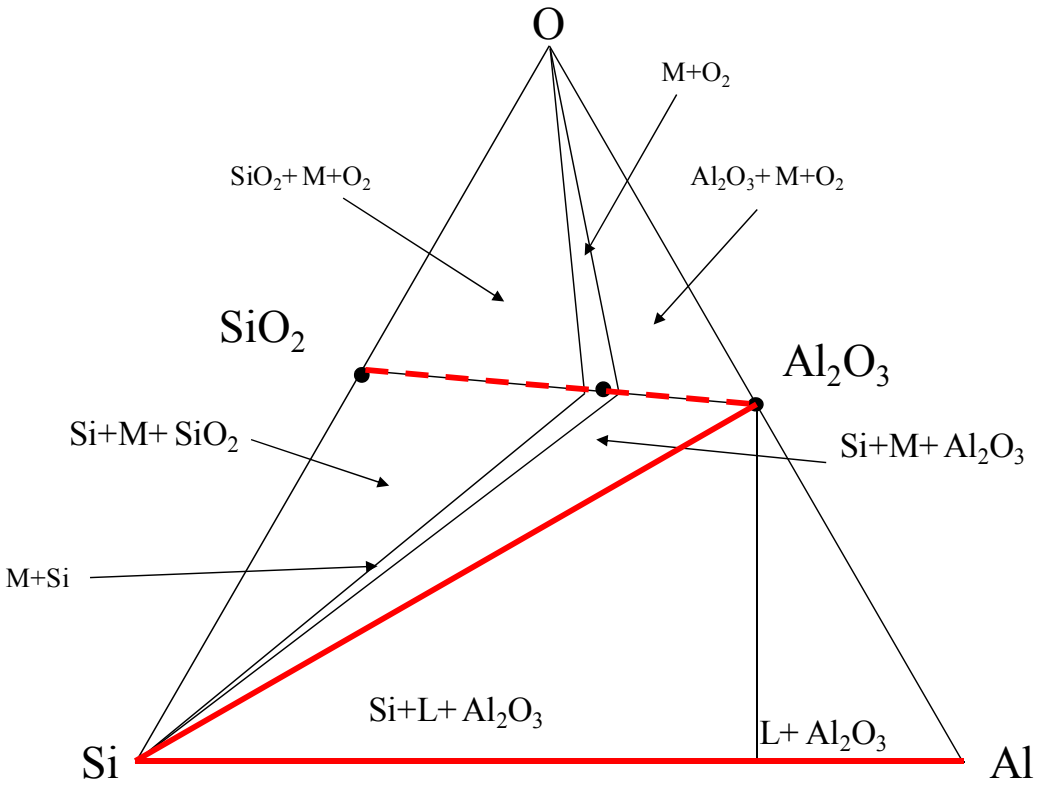

Figure 54. Isothermal section of Al-Si-O phase diagram showing the Al-SiO_2 reaction path

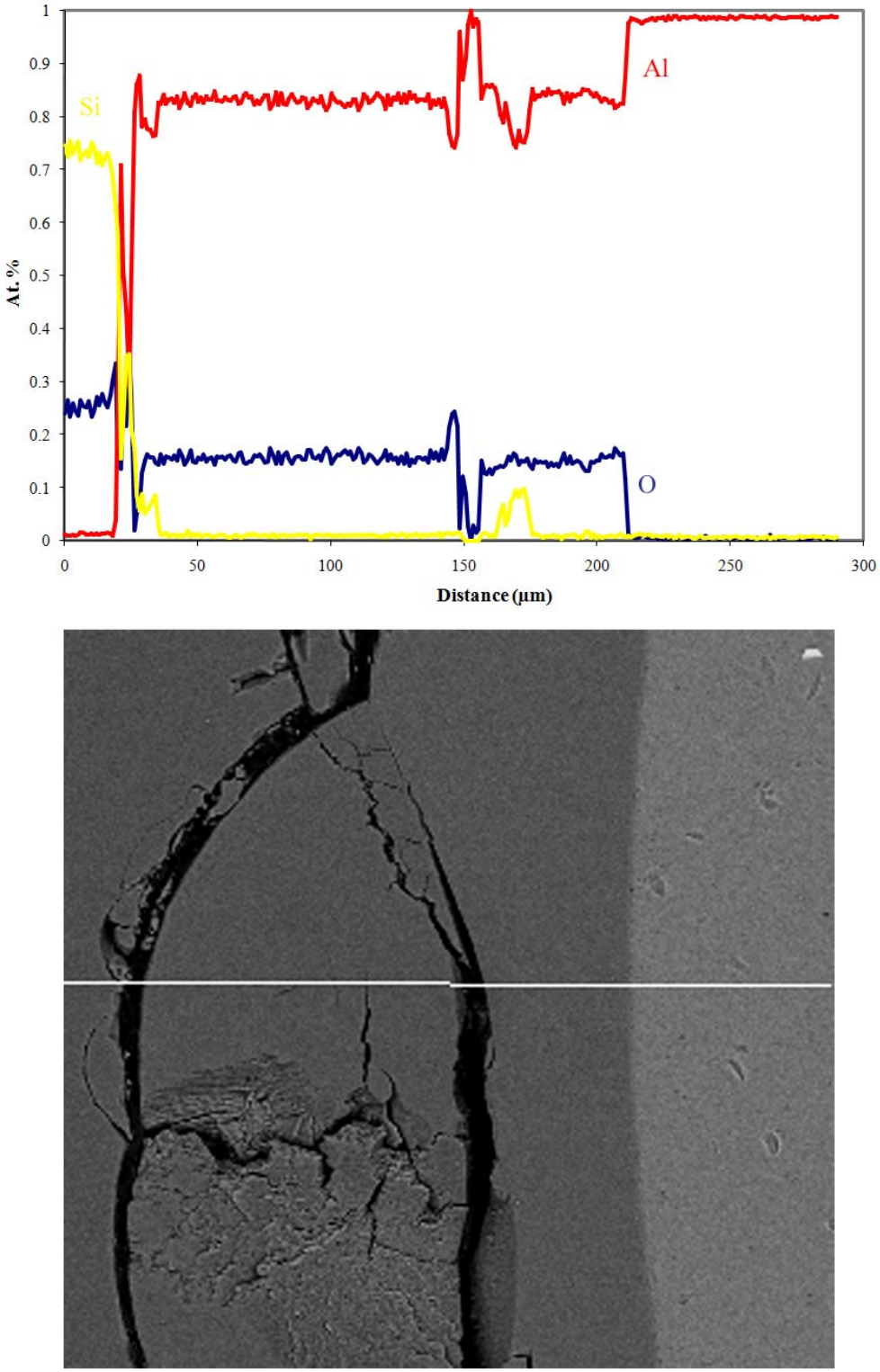

Figure 55 EDS line scan of Al-Silica interface after 30 minutes at 700°C

6.3.2 Aluminum-Mullite

In Section 5.3, it was shown that SiO_2 reacts extensively with molten aluminum to create a thick Al_2O_3 reaction product. Mullite, on the other hand, does not react at a comparable rate. The thermodynamics and kinetics of the aluminum-mullite reactions will now be considered

Mullite can be formed from the reaction of alumina with silica.

$$3Al_2O_3 + 2SiO_2 = Al_6Si_2O_{13} \tag{6.3.1}$$

Thus, the activities of silica and alumina in mullite can vary, Equation 6.3.2.

$$K = \frac{a^3_{Al_2O_3} a^2_{SiO_2}}{a_{Al_6Si_2O_{13}}} \tag{6.3.2}$$

If alumina is brought in contact with mullite at elevated temperature, and allowed to equilibrate, the activity of alumina in mullite will rise to a maximum level, equal to the activity of alumina in the adjacent, previously pure alumina phase. The exact nature of this equilibrium is not known, but if it assumed that the activity of alumina remains close to unity, the minimum silica activity can be estimated. At 700°C and 1000°C the activity of alumina saturated mullite is $a_{SiO_2} = 0.47$ and $a_{SiO_2} = 0.39$ respectively.

At the reduced activity, the reaction

$$3SiO_2 + 4Al = 2Al_2O_3 + 3Si \tag{6.3.3}$$

$$K = \frac{a_{Al_2O_3}^2 a_{Si}^3}{a_{Al}^4 a_{SiO_2}^3} \tag{6.3.4}$$

can still proceed, as long as the aluminum activity remains above $a_{Al}=5.5x10^{-7}$ and $a_{Al}=1.2x10^{-5}$ respectively. Therefore, mullite should be reduced by aluminum through the reaction

$$Al_6Si_2O_{13} + \frac{8}{3}Al = \frac{13}{3}Al_2O_3 + 2Si \tag{6.3.5}$$

After a 25 hour exposure at 700°C, mullite was found to react with Al to form Al_2O_3. The reaction was not uniform across the Al-mullite interface, and in the areas where reaction did take place, the alumina which formed was never greater than 5 μm thick.

In the analysis of Al-SiO_2 reaction, it was postulated that the reaction proceeded so rapidly due to the tensile cracking of the alumina reaction product. A similar analysis can be performed with mullite. However, there are two possible reaction products. If, as was observed in the Al-Silica system, the Al_2O_3 was adjacent to the original substrate, in this case mullite, the *PBR* would be

$$PBR = \frac{\frac{13}{3}V_{Al_2O_3}}{V_{Al_6Si_2O3}} = 0.91 \tag{6.3.6}$$

The value of *PBR* is less than unity, and therefore, it is expected that tensile stress should form in an Al_2O_3 layer growing into mullite. However if the silicon rejected by the reduction is incorporated into the Al_2O_3 layer, a tensile stress would no longer be expected.

$$PBR = \frac{\frac{13}{3}V_{Al_2O_3} + 2V_{Si}}{V_{Al_6Si_2O3}} = 1.09 \tag{6.3.7}$$

The change in volume associated with Equation 6.3.6 is closer to unity than that for SiO_2 reduction, and therefore, the stresses should be lower. It is possible the alumina layer can withstand this stress without cracking. Additionally, there is porosity present in the mullite, as seen in Figure 39. Stress relief could occur by a cracking or deflection of the porous mullite structure such that a thin Al_2O_3 layer can form and remain continuous.

6.3.3 Aluminum-Barite

No reaction product was found at the Al-$BaSO_4$ interface following a 20 hour exposure at 700°C. There are several possible chemical reactions which can take place between molten aluminum and barite. The free energy change for reaction 6.3.7 is the most negative at 700°C.

$$BaSO_4 + \tfrac{8}{3}Al = \tfrac{1}{3}Al_2S_3 + BaO + Al_2O_3 \qquad \Delta G^\circ = -1170kJ \qquad (6.3.7)$$

$$BaSO_4 + \tfrac{8}{3}Al = \tfrac{4}{3}Al_2O_3 + BaS \qquad \Delta G^\circ = -938kJ \qquad (6.3.8)$$

$$BaSO_4 + 2Al = \tfrac{4}{3}Al_2O_3 + \tfrac{1}{3}Al_2S_3 + Ba \qquad \Delta G^\circ = -931kJ \qquad (6.3.9)$$

As demonstrated in the previous sections, the phase evolution of ceramic phases at low temperatures does not always proceed such that the equilibrium structure is produced. However, it is clear that there is a thermodynamic driving force for molten aluminum to react with barite and at longer exposure times, reaction may proceed.

The PBR for the reaction in Equation 6.3.7 is greater than unity.

$$PBR = \frac{\frac{1}{3}V_{Al_2S_3} + V_{Al_2O_3} + V_{BaO}}{V_{BaSO_4}} = 1.09 \qquad (6.3.10)$$

Therefore, reaction may be taking place at the Al-$BaSO_4$ interface, but, if the reaction product is adherent, growth may be extremely slow at 700°C.

6.3.4 Application of the Pilling-Bedworth Ratio

The reaction rate of SiO_2 was shown to be so rapid, that it is not possible that it is rate controlled by diffusion through the growing Al_2O_3 layer. As reported previously, it is necessary that cracking in the growing oxide provides a continuous path for aluminum to reach the SiO_2 surface to allow the formation of Al_2O_3 to continue at the observed rate. It has been proposed that cracking in the oxide scale is initiated by tensile stresses which results from the net volume reduction that occur when three moles of SiO_2 are transformed into two moles of Al_2O_3. This is a direction analogy to the Pilling-Bedworth ratio, *PBR*, which has been used to describe the rapid oxidation certain metals due to tensile cracking in oxide layer that forms in the metal surface.

It is worthwhile to calculate the *PBR* of other molten metal-oxide systems and compare the results with observed ceramic degradation rates in the literature. The *PBR* of several molten metal-ceramic systems is presented in Table 12, along with the observed degradation rates. While the list is not comprehensive, in all of the noted examples, if the PBR is greater than unity, a slow reaction rate is observed, and if the PBR is less than unity, rapid reaction is observed.

This phenomenon is particularly noticeable when the reaction rate of SiO_2 and Si_3N_4 with molten aluminum is observed. In both cases, the standard free energy of formation of Al_2O_3 and AlN is larger, *-134 kJ/mol-Al*, and *-100 kJ/mol-Al*, respectively. However, the *PBR* of Al_2O_3 formation is *0.78* and the PBR of AlN formation is *1.18*. The reaction product thickness for SiO_2 is several orders-of-magnitude larger than that for Si_3N_4.

While the *PBR* has been used in the literature to describe molten metal-ceramic interactions, it has only been used to analyze a few systems. The stability of Si_3N_4 in molten Al for example shows that ceramics which form a mechanically stable reaction product when exposed to molten metals can degrade at very slow rates, even when there is a strong thermodynamic driving force for reaction. Indeed, it is well documented in the high temperature oxidation literature that the thermodynamic driving force for reaction does not have a strong effect on the rate of oxidation. With this in mind, it may be possible to develop new refractory materials which have good resistance to attack by molten metals despite a large thermodynamic driving force for reactions.

Table 12. Pilling-Bedworth ratio of several molten metal-ceramic reaction couples

Liquid Metal	Ceramic Substrate	Reaction Product	PBR	Reaction Product Thickness
Al	SiO_2	Al_2O_3	0.71	>100μm
Al	TiO_2	Al_2O_3	0.91	>100μm
Al	$3Al_2O_32SiO_2$	Al_2O_3	0.91	<1μm at 700°C, >100μm at 1000°C
Cu-Pd-Ti	Al_2O_3	Ti_2O_3	1.22	<10μm
Cu-Cr	C	Cr_7C_3	3.65	<10μm
Al	Si_3N_4	AlN	1.18	<1μm
Cu-Si	C	SiC	2.43	<10μm

6.4 DYNAMIC CAPILLARY DISPLACEMENT

The primary motivation for the development of the dynamic capillary displacement technique was to create a test which is capable of evaluating the tendency of molten aluminum to infiltrate a crack in a refractory crucible.

The tendency for a liquid to infiltrate a crack, or any capillary volume, is governed by surface thermodynamics. If the surface free energy of the solid, in this case the refractory ceramic, is greater than the solid-liquid interfacial free energy, the system will lower its energy when the liquid flows into the crack destroying solid surface and creating the solid-liquid interface. The parameter which can be used to describe this tendency is the work of immersion, W_I, described in Section 2.2.4. If the W_I is negative, pressureless, spontaneous infiltration occurs.

$$W_I = \sigma_{SL} - \sigma_S \tag{6.3.1}$$

Alternatively, if W_I is positive, infiltration will only occur if an external source of energy, such as a metallostatic pressure, is applied to the liquid at the surface of the crack. The critical crack size into which infiltration can occur will then depend on the metallostatic pressure, and the magnitude of W_I.

The parameter W_I, can be experimentally determined in a number of ways. Most commonly, this is done through the sessile drop measurement in which the contact angle is measured and the W_I can be calculated through Equation 6.3.2.

$$W_I = -\sigma_L \cos\theta \tag{6.3.2}$$

However, as described in Section 2.7.1.1, great pains must be taken to perform the sessile drop test in a non-reactive atmosphere. Specifically, the surface of the liquid metal must remain free of oxide so that the liquid can flow to the equilibrium shape.

While the actual value of the liquid surface free energy greatly affects the measured contact angle, it does not affect the tendency for a liquid to infiltrate into a crack, or any capillary like volume, Equation 6.3.1. Therefore, in the analysis of the infiltration behavior of reactive liquid metals, it is prudent to develop a test in which the liquid surface energy does not affect the determination of W_I.

The classic capillary rise test is such a measurement. As described in Section 2.2.4, the height that a liquid will climb or fall in a capillary tube is a function of the work of immersion.

$$h = \frac{2W_I}{\rho g r} = \frac{2\left(\sigma_{SL} - \sigma_S\right)}{\rho g r} = \frac{-2\sigma_L \cos\theta}{\rho g r} \tag{6.3.3}$$

Once, W_I is determined, the contact angle, θ, can be calculated and compared with sessile drop data, with independent knowledge of the liquid surface free energy.

6.4.1 Oxide Film Disruption

To allow the molten aluminum to flow into the capillary tube, vibrational energy, in the form of sound waves, was transmitted to the tube to rupture the oxide film. The exact nature by which the film ruptures is unknown, but two possibilities will be considered.

First, assume that the oxide film-tube interface is extremely strong, and liquid metal flows into the tube when the oxide film fractures at the center of the tube. Such a fracture is analogous that of rupture discs, which are frequently used as safety valves in devices with pressured gas. This failure mechanism is schematically represented in Figure 56.

The mechanics of this problem have been analyzed by Brown and Sachs[68], who developed the expression for the critical rupture pressure, P_R, in terms of the ultimate tensile strength, σ_{UTS}, of the rupture disc material, the thickness, t, and the diameter, D, and a dimensionless constant k.

$$P_R = \frac{\sigma_{UTS} t}{kD} \tag{6.3.4}$$

The work necessary to break the film can then be calculated assuming the film moves a distance equal to amplitude of vibration, Δh.

$$W = \int P_R dV = A \int_{h_1}^{h_2} P_R dh = \pi r^2 P_R \Delta h \tag{6.3.5}$$

Approximating the ultimate tensile strength of oxide film to be that of α-Al_2O_3, the energy associated with rupture can be calculated to be $1.22x10^{-8}$ J for an oxide 250 nm thick in a tube with a 3 mm diameter, with an amplitude of vibration of 1 μm, assuming *k=1*.

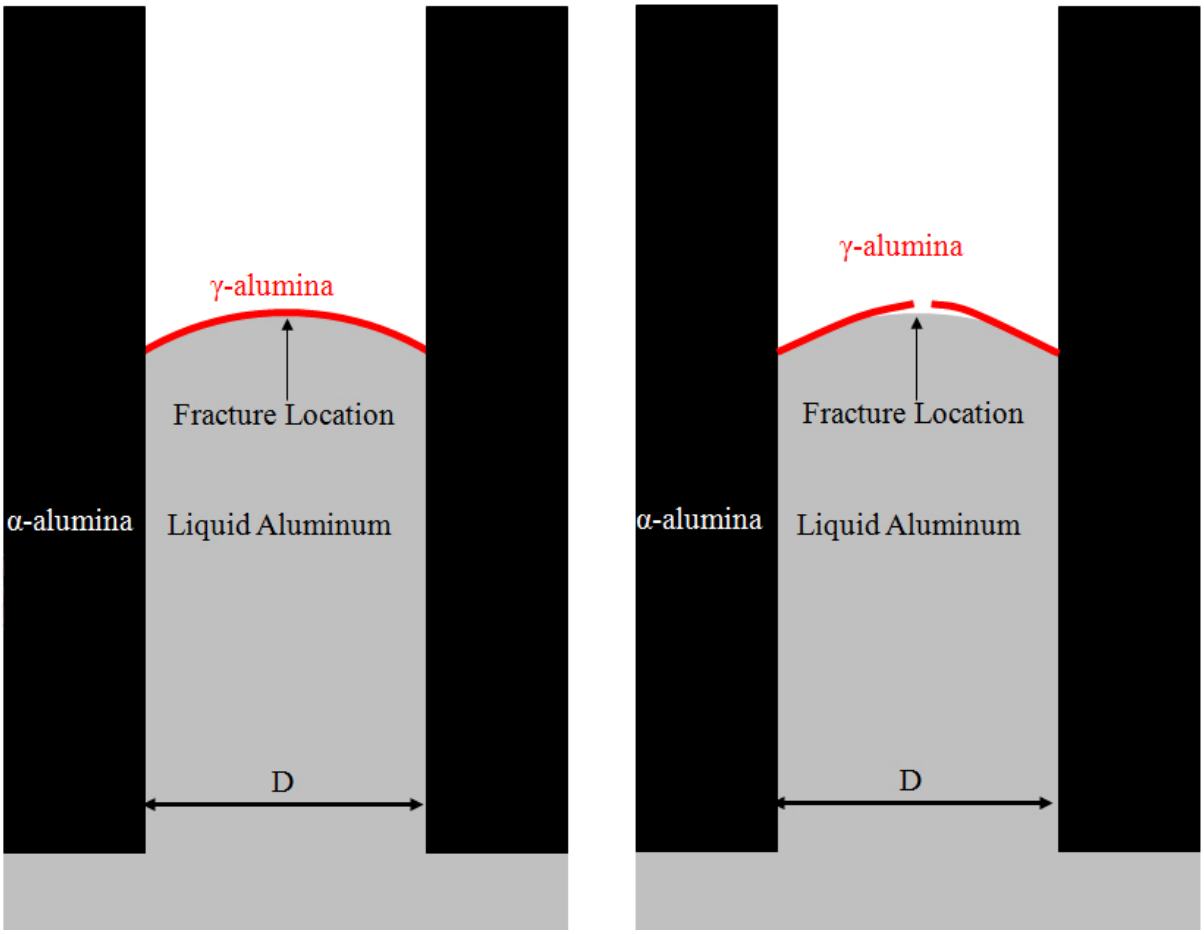

Figure 56. Schematic of oxide film before (left) and after (right) disruption, by the rupture disc mechanism

Alternatively, the oxide film could be separated from the alumina tube wall, schematically represented in Figure 57. The energy change associated with this process can be calculated from the contact area between the film and the tube, and the work of adhesion of the film and the tube.

$$W_A = \sigma_{\alpha\gamma} - \sigma_\alpha - \sigma_\gamma \tag{6.3.6}$$

A conservative estimate for the work of adhesion, W_A, between α-Al_2O_3 and γ-Al_2O_3 is the fracture energy of alumina, which has been found to be 30 J/m^2.[69] The work necessary to separate the thin film is approximately 1.8×10^{-12} J. In addition to the separation, some amount of elastic deformation would need to occur to allow the film to flex inward away from the tube wall. The total amount of energy for this process is much less than the energy necessary to rupture the film.

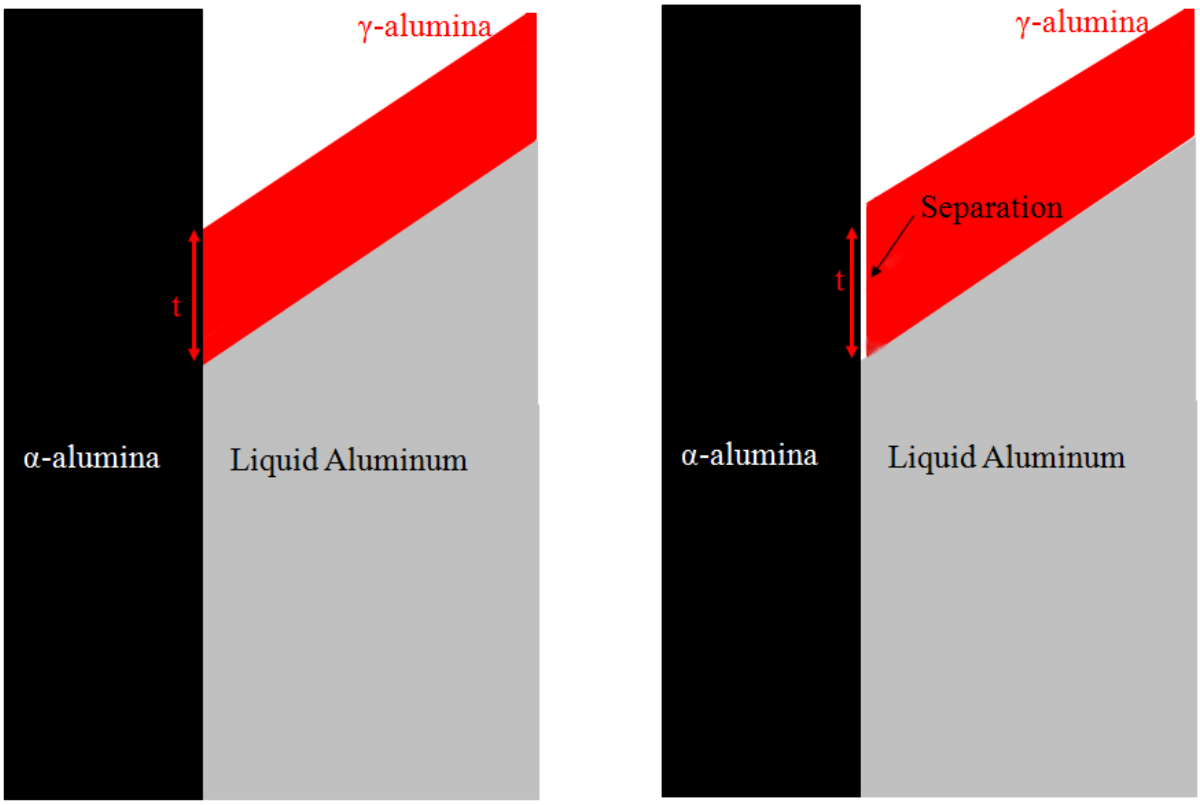

Figure 57. Schematic of oxide film before (left) and after (right) separation with tube

Once the film is disrupted, the liquid will begin to flow into the capillary tube. However, due the presence of oxygen in the atmosphere, the film will re-adhere to the tube as new oxide is created. It is, therefore, necessary for a continuous amount of vibrational energy be supplied, over a given time interval, to allow the liquid to move up the capillary tube. In experiments where a short pulse of energy was applied, the molten aluminum did not move to the equilibrium capillary depth.

6.4.2 Capillary Energetics

The variation in the total surface energy of the system, as a function of liquid height is plotted in Figure 58. For a given work of immersion, W_I, the minimum energy is independent of tube radius, which can be determined by substituting Equation 2.2.10 into 2.2.9

$$E^* = 6\pi \frac{(\sigma_{SL} - \sigma_S)^2}{\rho g} \tag{6.3.7}$$

The increase in energy that results when the height of the liquid is slightly above or below the h^* does change as a function of tube radius, Figure 58. The change in energy with respect to the change in height follows Equation 6.3.8. Therefore, the driving force for the liquid to move from a non-equilibrium position to the equilibrium position increases with increasing tube radius.

$$\frac{dE}{dh} = (\sigma_S - \sigma_{SL})2\pi r + \rho g \pi r^2 h \tag{6.3.8}$$

Alternatively, the effect that a given error in the measurement of the height will have on the calculated W_I increases with increasing radius.

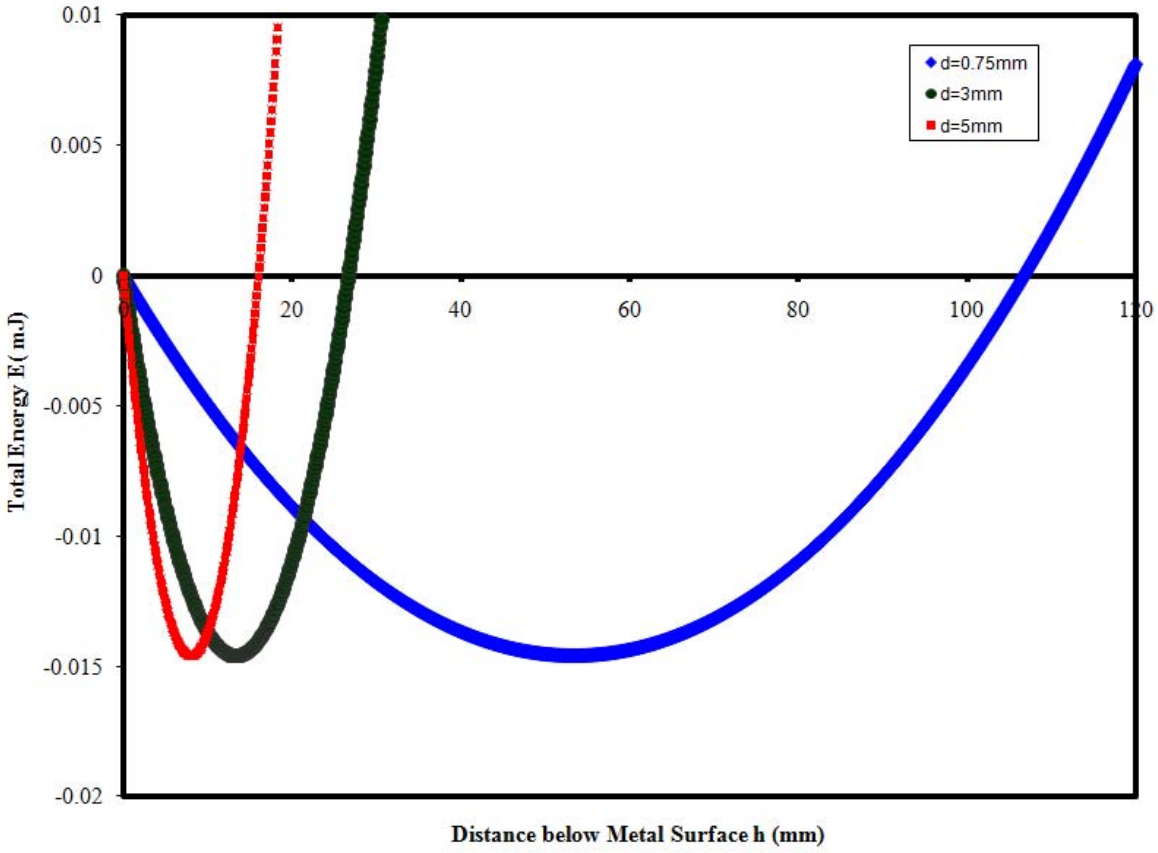

Figure 58. Total energy of a capillary liquid as a function of depression depth or a given W_I.

As was described in Section 5.4.1, the contact angle of liquid aluminum on polycrystalline alumina was determined. The contact angle, determined by a least-squares regression analysis of the data give a avalue of 100.5°±2.5°, which is in good agreement with both sessile drop and tensiometric contact angles determined by Laurent et al to be 101°.[49]

6.4.3 Future Applications

The primary hurdle to the widespread use of the DCD testing method is the fabrication of capillary tubes of the desired materials, which are sufficiently dense, with sufficiently smooth inner surfaces, and have small enough inner diameters such that the capillary displacements are great enough to allow a precise measurement. This hurdle is not trivial. However, processes such as slip casting allow the fabrication of dense, small diameter tubes. Indeed, such tubes are fabricated for use as thermocouple sheaths. The fabrication of tubes with the composition multiphase refractory ceramics would be more costly, and may not be practical in many circumstances. Nevertheless, the DCD is an option to investigate the wetting behavior of liquid aluminum on ceramics.

Additionally, a large bath of liquid aluminum is necessary to perform these tests. This may make the DCD technique impractical in an academic setting. The amount of metal does not need to be as great as was used in the present investigation, however it is necessary that volume of metal which is displaced as the tube is lowered, does not raise the global metal level.

The use of such a testing method could be particularly useful in an industrial setting in which knowledge of the infiltration behavior of a variety of aluminum alloys on different ceramic materials may give critical information to improve the efficiency of a given process. For example, the degradation of a given refractory in a given alloy could be better modeled if the infiltration behavior of that system was known. Also, in the fabrication of metal-matrix composites where it is desired that the liquid metal spontaneously flow into a ceramic pre-form, the compatibility of metal-ceramic couples could be investigated using the dynamic capillary rise technique.

7.0 CONCLUSIONS

In this investigation several types of molten metal-ceramic interactions were studied to better understand the degradation mechanisms of refractory ceramics by molten metals. Oxide dissolution, chemical reaction, and infiltration were focused upon. Advances in the understanding of each of these phenomena were made, such that as a whole, the understanding of the processes by which molten metals degrade refractory ceramics was furthered. The conclusions from each investigation are highlighted below.

7.1 OXIDE DISSOLUTION

A model was developed to describe the behavior of non-reactive molten metal-oxide couples. This model was used to calculate the equilibrium concentration of dissolved species in the molten metal, at the metal-oxide interface, and, the dissolution rate of an oxide immersed in an infinite bath of molten metal. Further, the model showed that the flux of the dissolved oxide species away from the metal-oxide interface is an important parameter which affects the equilibrium interfacial oxygen concentration.

7.2 SESSILE DROP EXPERIMENTS

The sessile drop method is widely used to study the interactions between liquid metals and solid oxides. The contact angle, the parameter measured in sessile drop experiments, is a lumped parameter determined by the solid and liquid surface free energies, and the solid-liquid interfacial free energy. From this measurement, a number of physical properties of metal-oxide systems can be inferred, such as adhesive strength of the metal-oxide interface, typically described through the work of adhesion, and the tendency for a liquid to infiltrate a capillary volume, which is determined by the sign of $\cos(\theta)$. However, in order for the contact angle to give insight into these related phenomena, the factors which affect the contact angle must be properly analyzed. In this work several steps were taken to further this pursuit.

- In the literature, it has been proposed that the concentration of *M-O* clusters at the metal-oxide interface has a strong effect on the solid-liquid interfacial energy. This proposal has been supported in this work by showing that the tendency for clustering can be increased by increasing the driving force for the metal species to cluster, demonstrated by the decreasing contact angle in the Cu-NiO system which occurred when 1 at.% Ni was alloyed in to Cu, and by increasing the driving force for clustering by increasing the dissolved oxygen concentration, demonstrated by the decreasing contact angle in the Ag-NiO system that occurred when the pO_2 in the atmosphere was increased. In both cases, the tendency for oxide dissolution decreased, demonstrating that the *M-O* cluster concentration, not the tendency for oxide dissolution, affects the contact angle.

- The solid-liquid interfacial free energy of the area near the triple line will affect the spreading of the liquid metal to equilibrium contact angle, and, therefore, it is not essential for the solid-liquid interfacial free energy of the entire area of solid-liquid interface to be modified by the segregation of *M-O* clusters for the contact angle to change. As a result, the contact angle, determined in the sessile drop experiment, cannot be predicted solely by the thermodynamic data which describes oxide dissolution, because, oxygen dissolution from the gas phase will affect X_O, near the tripleline.

- The tendency for the metal-oxide interface in a sessile drop to become morphologically unstable was described. This analysis shows that the interface of all metal-oxide sessile drops will tend to be unstable, and the perturbation will grow until the dissolution of oxide is stopped by positive oxygen concentration gradient between the metal-oxide interface and the gas-metal interface. In many metal-oxide couples, the time it takes for the positive oxygen gradient to develop is extremely short, and unstable interfaces are not observed.

- The effect that the addition of a second phase to the surface of a solid has on the contact angle was studied in the Cu-NiO-YSZ system. While this study was limited, the previous trends in the literature were confirmed. The addition of a non-wetting second phase results in an incremental increase in the contact angle, as described by Horstemke and Schroder.

7.3 MOLTEN METAL-CERAMIC REACTIONS

- Silica, mullite, and barite were immersed in molten aluminum for different time periods and at different temperatures. The resulting microstructural evolution was characterized using SEM and X-Ray diffraction. The observations from this work were analyzed using the a thermodynamic model of van Loo et al, to predict the layer sequence which develops between solid metal-oxide diffusion couples.

- It is proposed that the rapid rate of reaction between Al and SiO_2, results from the continuous cracking of the growing Al_2O_3 layer, due to tensile stress, caused by the net volume reduction associated with reaction. The net change in volume is calculated by determining the ratio of reaction product volume to reactant volume, in analogy to the Pilling-Bedworth ratio.

- The *PBR* for several other molten metal-oxide systems was calculated, and results from the literature were used to compare the resulting phase evolution with the magnitude of the *PBR*. In the cases considered, a *PBR* of less than unity corresponded to the rapidly growing reaction product, while materials with a *PBR* of greater than unity, e.g. Al-Si_3N_4, reacted much more slowly. From this result, it is suggested that the new refractory ceramics could be developed by choosing materials with a *PBR* greater than unity for the given molten metal application.

7.4 INFILTRATION

- An experimental method has been developed to determine the contact angle, based on the classic capillary rise experiment. The contact angle was determined by measuring the distance a liquid is raised or depressed in a capillary tube, above the external liquid surface. Alumina, mullite, and silica tubes were used to determine the capillary displacement of molten aluminum, and silica tubes were used to determine the capillary displacement of H_2O.

- The contact angles of Al on Al_2O_3, and H_2O on silica using the DCD were in good agreement with literature values.

- The DCD method is particularly suited to determine the tendency for molten metal to infiltrate cracks in the ceramic materials. The tendency for infiltration is governed by the magnitude of the difference between the solid surface free energy and the interfacial free energy and is not directly affected by the liquid metal surface free energy. The contact angle, measured by the sessile drop test is directly affected by the liquid metal surface free energy which can be strongly influenced by interactions with the atmosphere. Metals which are highly reactive with oxygen, such as aluminum, are particularly sensitive to atmospheric interactions. Therefore, to investigate the infiltration behavior of molten aluminum into cracks, the DCD method has clear advantages over the sessile drop method.

REFERENCES

1. Ernst, F., Mater. Sci. Eng. , 1995. **R14**: p. 97-156.

2. Partridge, P.G. and C.M. Ward-Close, Inter. Mater. Adv., 1993. **38**: p. 1.

3. Birks, N., G.H. Meier, and F.S. Pettit, *Introduction to the High Temperature Oxidation of Metals*. 2nd ed. 2006, Cambridge: Cambridge University Press.

4. Moya, J.S., S. Lopez-Esteban, and C. Pecharroman, Prog. Mater. Sci., 2007. **52**: p. 1017-1090.

5. Hemrick, J.G., W.L. Headrick, and K.M. Peters, Int. J. Appl. Ceram. Technol., 2008. **5**: p. 265-277.

6. Rühle, M. and A.G. Evans, Mater. Sci. Eng., 1989. **107**: p. 187.

7. Eustathopoulos, N., M.G. Nicholas, and B. Dervet, *Wettability at High Temperatures*. Pergamon Materials Series, ed. R.W. Cahn. Vol. 3. 1999, Amsterdam: Pergamon.

8. Gibbs, J.W., *The Scientific Papers of J. Willard Gibbs*. 1961, New York: Dover Publications.

9. Shuttleworth, R., Proc. Phys. Soc., 1950. **A63**: p. 444.

10. Dupre, A., *Theorie Mecanique de la Chaleur*. 1869, Paris: Gauther-Villars.

11. Young, T., Phil. Trans. Roy. Soc. Lond., 1805. **94**: p. 65.

12. Laplace, P.S., *Mechanique Celeste*. 1805, Paris: Chez Courier.

13. Defay, R. and I. Prigogine, *Surface Tension and Adsoprtion*. 1966, New York: John Wiley and Sons.

14. Israelachvili, J.N., *Intermolecular and Surface Forces*. 1985, London: Academic Press.

15. McDonald, J.E. and J.G. Eberhart, TAIME, 1965. **233**: p. 512.

16. Eustathopoulos, N. and B. Dervet, Mater. Sci. Eng. A, 1998. **249**: p. 176.

17. Rhines, F.N., *Phase Diagrams in Metallurgy*. 1956, New Yotk: McGraw-Hill.

18. Didier, F. and J. Jupille, Surface Science, 1994. **314**: p. 378-384.

19. Duffy, D.M., J.M. Harding, and A.M. Stoneham, Acta Metall. Mater, 1992. **40 Suppl.**: p. S11-S16.

20. Lipkin, D.M., J.N. Israelachvili, and D.R. Clarke, Phil. Mag. A, 1997. **76**(4): p. 715-728.

21. Naidich, Y.V., Prog. Surf. Membrane. Sci., 1981. **14**: p. 353-484.

22. van Loo, F.J.J., et al., Oxid. Met., 1984. **22**: p. 161-180.

23. Backhaus-Ricoult, M., Ber. Bunsenges. Phys. Chem., 1986. **90**.

24. Kittel, C., *Introduction to Solid State Physics*. 2005, John Wiley and Sons, Inc.: New York.

25. Hamaker, A., Physica, 1937. **4**: p. 1058.

26. Hough, D.B. and L.R. White, Adv. Colloid Interface Sci., 1980. **14**: p. 3-41.

27. De Graef, M., et al., *Interfaces between alumina and platinum: Structure, bonding and fracture resistance.* Acta Metall. Mater, 1992. **40**: p. S333-S344.

28. Wagner, C., Z. Phys. Chem., 1933. **31**: p. 25.

29. Rapp, R.A., A. Ezis, and G.J. Yurek, *Displacement reactions in the solid state* Met. Trans. A, 1973. **4**: p. 1283-1292.

30. Li, X.L., et al., Acta Metall. Mater, 1992. **40**: p. 3149.

31. Pilling, N.B. and R.E. Bedworth, J. Inst. Met., 1923. **29**: p. 529.

32. Zhou, X.B. and J.T.M. De Hosson, Acta Mater., 1996. **44**: p. 421-426.

33. Nicholas, M.G., T.M. Valentine, and M.J. Waite, J. Mater. Sci., 1980. **15**: p. 2197-2206.

34. Afshar, S. and C. Allaire, JOM, 2000. **52**: p. 43-46.

35. Wenzel, R.N., Ind. Eng. Chem., 1936. **28**: p. 988.

36. Cassie, A.B.D., Discuss. Faraday Soc., 1948. **3**: p. 11.

37. Johnson, R.E. and R.H. Dettre, J. Phys. Chem, 1964. **68**: p. 1744-1750.

38. Dettre, R.H. and R.E. Johnson, J. Phys. Chem, 1965. **69**: p. 1507-1515.

39. Horsthemke, A. and J.J. Schoder, Chem. Eng. Process., 1985. **19**: p. 277-285.

40. Naidich, Y.V., R.P. Voitovich, and V.V. Zabuga, J. Coll. Inter. Sci., 1995. **174**: p. 104-111.

41. Gallois, B. and C.H.P. Lupis, Metall. Trans., 1981. **12B**: p. 549-557.

42. Nikolopoulos, P. and D. Sotiropoulou, J. Mater. Sci. Letters, 1987. **6**: p. 1429-1430.

43. Ghetta, V., J. Fouletier, and D. Chatain, Acta Mater., 1996. **44**: p. 1927-1926.

44. Yi, S., K.P. Trumble, and D.R. Gaskell, Acta Mater., 1999. **47**: p. 3221-3226.

45. Naidich, Y.V., *Kontaktnie Javlenia v Metallicheskih Rasplavakh*. 1972, Kiev: Nauka Dumka.

46. Cabrera, N. and N.F. Mott, Rept. Prog. Phys., 1948. **12**: p. 163.

47. Freti, S., J.D. Bornand, and K. Buxmann, Light Met., 1982: p. 1003-1016.

48. *Binary Alloy Phase Diagrams*, ed. T.B. Massalski. 1986, Metals Park, OH: ASM.

49. Laurent, V., et al., Acta Metall., 1988. **36**: p. 1797.

50. Ueki, M., M. Naka, and I. Okamoto, J. Mater. Sci., 1988. **23**: p. 2983-2988.

51. Naidich, Y.V., et al., Poroshkovaya Metallurgiya, 1983. **246**: p. 67.

52. Fu, Q. and J.W. Evans, Met. Trans. B, 1998. **29**: p. 971-978.

53. Cahoon, J.R., Met. Trans. A, 1997. **28**: p. 583-593.

54. Niessen, A.K., et al., Calphad, 1983. **7**: p. 51.

55. Shen, P., H. Fuiji, and K. Nogi, J. Mater. Res., 2005. **20**: p. 940-951.

56. Hitchcock, S.J., N.T. Carroll, and M.G. Nicholas, J. Mater. Sci., 1981. **16**: p. 714-732.

57. Sotiropoulou, D., J. Mater. Sci., 1997. **16**: p. 693-695.

58. Rado, C., B. Drevet, and N. Eustathopoulos, Acta Mater., 2000. **48**: p. 4483-4491.

59. Neumann, J.P., et al., Met. Rev. MMIJ, 1987. **4**: p. 106-120.

60. Oberg, K.E., et al., Met. Trans. A, 1973. **4**: p. 61-67.

61. Ramanarayanan, T.A. and R.A. Rapp, Met. Trans. A, 1972. **3**.

62. Nogi, K., et al., Mater. Trans. JIM, 1991. **32**: p. 164.

63. Mehrotra, S.P. and A.C.D. Chaklader, Met. Trans. B, 1985. **16**: p. 567.

64. Chatain, D., Annu. Rev. Mater. Res., 2008. **38**: p. 45-70.

65. Jackson, R.W., F.S. Pettit, and G.H. Meier, Manuscript in preparation, 2010.

66. Brumm, M.W. and H.J. Grabke, Corr. Sci., 1992. **33**: p. 1677.

67. Hallstedt, B., Z. Liu, and J. Agren, Mater. Sci. Eng. A, 1993. **169**: p. 149-157.

68. Brown, W.F. and G. Sachs, Trans. ASME, 1948. **70**: p. 241-251.

69. Davidge, R.W. and G. Tappin, J. Mater. Sci., 1968. **3**: p. 165-173.